Stony Brook University

High Resolution, Frequency Comb-Referenced Measurements of Spectral Line Shapes

A Dissertation Presented

by

Matthew James Cich

to

The Graduate School

in Partial Fulfillment of the

Requirements

for the Degree of

Doctor of Philosophy

in

Chemistry

Stony Brook University

August 2014

Stony Brook University

The Graduate School

Matthew James Cich

We, the dissertation committee for the above candidate for the

Doctor of Philosophy degree, hereby recommend

acceptance of this dissertation.

Trevor J. Sears
Professor of Chemistry, Department of Chemistry, Advisor

David M. Hanson
Professor of Chemistry, Department of Chemistry, Chairman

Philip M. Johnson
Professor of Chemistry, Department of Chemistry

Robert R. Gamache
Professor, Department of Environmental, Earth, and Atmospheric Sciences, University of

Massachusetts Lowell

This dissertation is accepted by the Graduate School

Charles Taber
Dean of the Graduate School

Abstract of the Dissertation

High Resolution, Frequency Comb-Referenced Measurements of Spectral Line Shapes

by

Matthew James Cich

Doctor of Philosophy

in

Chemistry

Stony Brook University

2014

Spectroscopic methods for retrieval of atmospheric data such as pressure, temperature, and concentration depend on the accurate characterization of spectral line shapes. As a model system, the P(11) line of the $\upsilon_1+\upsilon_3$ band of acetylene, near 1.5 μm, was explored in great detail using a high resolution spectrometer based on a frequency comb-referenced continuous wave laser. This spectrometer is capable of measurements with frequency accuracy better than 1 part in 10^{11}. This allows for unprecedented accuracy in experimental data exploring the effects contributing to a spectral line shape.

Direct absorption measurements on acetylene in a cell capable of modeling atmospheric conditions of varying temperatures and pressures have been made. Line shapes due to acetylene-acetylene and acetylene-nitrogen collisions were investigated at pressures up to 1 atm. and temperatures between 125 K and 296 K. Fitting line shapes in a practical way requires models that have parameters that scale realistically with temperature and pressure. Several of the most common line shape models were examined including models with broadening, shift, narrowing, and speed-dependent effects. Fits resulted in line shape parameters with large improvements in accuracy over previous measurements due to the frequency accuracy of the spectrometer.

Frontispiece

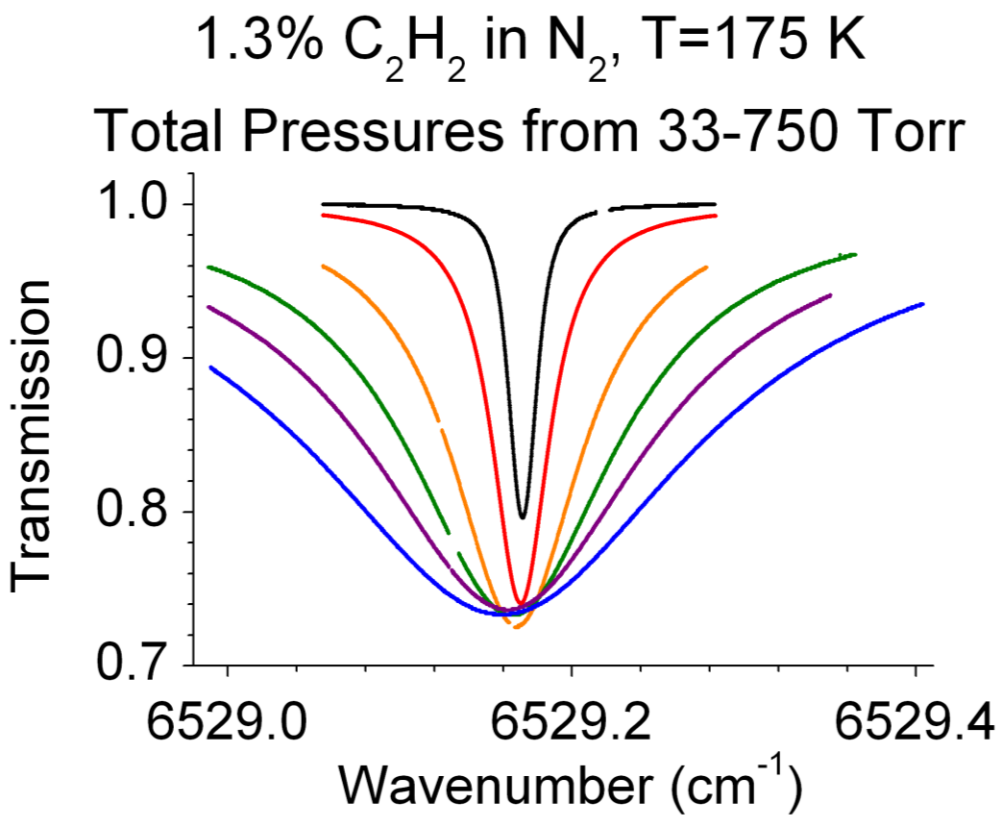

Table of Contents

List of Figures

List of Tables

List of Abbreviations

ADC: analog to digital converter

csdRG: correlated speed-dependent Rautian-Galatry profile

CW: continuous wave

DDS: direct digital synthesizer

ECDL: external cavity diode laser

EOAM: electro-optic amplitude modulator

EOM: electro-optic modulator

EOPM: electro-optic phase modulator

GPS: global positioning system

HARD: Rautian-Sobel'man profile

HWHM: half width at half maximum

LP: lowpass filter

O-C: observed minus calculated

OFHC: oxygen free high conductivity

PDH: Pound-Drever-Hall

PID: proportional-integral-derivative

PPLN: periodically-poled lithium niobate

Q-SDV: quadratic Speed-Dependent Voigt

RGP: Rautian-Galatry profile

RMS: root mean square

RMSE: root mean square error

SOFT: Galatry profile

SDV: Speed-Dependent Voigt line shape model

SDG: Speed-Dependent Galatry model

S/N: signal-to-noise

TDL: tunable diode laser

VCO: voltage-controlled oscillator

WSL: weighted sum of Lorentzians

Acknowledgments

I would like to offer my thanks to my research advisor Trevor Sears for making this work possible and for extensive guidance, insight, and support throughout the years. Thank you to Gary Lopez who was a graduate student with me and assisted in many ways inside and outside the lab. Thank you to postdoctoral researchers Damien Forthomme and Christopher McRaven for years of collaboration and very constructive interactions. Discussions with Greg Hall and Philip Johnson have been very insightful and invaluable. I am very grateful to Arlan Mantz for his development of the temperature-controlled absorption cell, for his close collaboration with us throughout the project and for introducing our research group to the field of line shape modeling. Thanks to the other postdoctoral researchers who have provided insight along the way including Vasily Goncharov and Sylvestre Twagirayezu, and the undergraduate students who have made contributions.

I appreciate the feedback and valuable time offered by my committee members who have been with me as I completed my degree requirements. The chemistry department staff have been incredibly helpful and tolerant through many difficult problems and their friendly assistance has always gone beyond expectations.

I am deeply grateful to my wife Caitlin who has been very supportive throughout the years I have been at Stony Brook. I would like to express my gratitude to my parents, family and friends who have helped or supported me over the years.

For funding considerations, acknowledgement is made to the Donors of the American Chemical Society Petroleum Research Fund for partial support of this research. Thanks to Program Development Funding awarded to Trevor J. Sears by Brookhaven National Laboratory which provided funds for some of the equipment used in this work. Work at Brookhaven National Laboratory was carried out under Contract No. DE-AC02-98CH10886 with the US Department of Energy, Office of Science, and supported by its Division of Chemical Sciences, Geosciences and Biosciences within the Office of Basic Energy Sciences.

Chapter 1: Introduction

Femtosecond laser-based frequency combs allow for incredibly high accuracy in spectroscopic measurements. During the last decade the development of phase-locked optical frequency combs in the near infrared has revolutionized metrology and optical clocks [2-6] and the technology has been applied to the measurement of molecular spectra [7-10]. They can act like rulers that measure and stabilize the difference between two optical frequencies. When one of these frequencies is fixed by a well-known reference, like the atomic clock frequency standard, the other can be determined to high accuracy and precision. Spectroscopic techniques based on this technology will have a profound effect on the precision and accuracy of high resolution spectroscopy in the near future. In the near-infrared spectral region the technology is particularly attractive because of the availability of highly efficient detectors, tunable diode lasers and erbium-doped fiber combs. External cavity diode lasers (ECDLs) permit continuous coverage of wide spectral regions, frequently providing continuous coverage of entire infrared bands [11]. Studies have been done using comb-referencing and ECDLs to measure high resolution rovibrational transition positions, for example [12, 13]. One area which can benefit greatly from applying the high resolution of frequency comb-referenced spectroscopy is the measurement and modeling of spectral line shapes.

The characterization of spectral line shapes is vital to fields as diverse as remote sensing, astronomy, analytical spectroscopy, and the molecular physics of collisions. Improvements in laboratory techniques and measurements provide the empirical data that drive advances in these fields. The improved determination of the subtle shifts and broadening caused by self- or foreign-gas collisions at increased pressures demands extremely good control of spectrometer frequency. For the present system, an absolute frequency accuracy of 8 kHz at 196 THz is shown to be possible[14], corresponding to a stability of 2.5 parts in $10^{12.}$ As a comparison, high resolution Fourier Transform Interferometers are usually controlled by helium neon (HeNe) lasers having a frequency stability of about 2 parts in 10^{8}, and tunable diode lasers locked to a stabilized Michelson interferometer exhibit similar performance[15, 16]. A portion of the data

reported here includes the first line shape measurements to take advantage of the precision and accuracy of frequency comb-referenced techniques, as mentioned in a review by Margolis[17]. More recently, CO_2[18] and CH_4[19] line shape measurements have also been made using frequency comb-referenced techniques.

The motivations for using acetylene as a model system for this new spectroscopic technique are numerous; the relatively strong $\nu_1 + \nu_3$ combination band of acetylene at 1.5 μm has long been used as a model system[20-22]. Spectroscopic measurements of the $\nu_1 + \nu_3$ band of acetylene are numerous, and following the first frequency-based optical measurements[23], the isolated rotational lines have been used as secondary frequency standards[24]. They were also some of the earliest molecular spectra measured referenced to a frequency comb[12, 25] in 2005[26, 27].

The 1.5 μm region lies in a window between strong water vapor and methane bands and is therefore convenient for both terrestrial and satellite observations. Acetylene in the earth's atmosphere[28, 29] has been linked to industrial processes[30] and marine sources[31], and may even have influenced the evolution of the earliest organisms[32]. Elsewhere in the solar system, acetylene has been detected around Jupiter's poles with the NASA Infrared Telescope by the NASA Cassini spacecraft [33]. Measurements of the dense, low temperature atmosphere of Titan [34] show it is composed mostly of nitrogen (98.4%) and methane (1.4%, but 4.9% close to the surface). The temperature of Titan's atmosphere is 94 K at the surface [35], where the pressure is approximately 1.45 times that of the earth's atmosphere. Trace amounts of acetylene and other hydrocarbons have also been detected [36, 37] in the atmosphere by mass spectrometers on fly-by missions and contribute to contributes to a complex photochemistry [38].

Past studies have reported line shape parameters for this band for pure acetylene and for acetylene in collisions with nitrogen and inert gases[11, 21, 39-41] and others listed in reference[42]. Several recent studies have measured the temperature dependence of collisionally- perturbed line shapes for both self-collisions[1] and collisions with N_2[39, 40]. First measurements of line broadening, collisional narrowing, shifts, and speed-dependent effects

caused by self- and nitrogen-gas broadening in the $\nu_1 + \nu_3$ band of acetylene at 1.5μm using an extended cavity diode laser locked to a femtosecond frequency comb are reported here. The Data Sets presented here [1, 14, 43] demonstrate how this increase in frequency stability translates into substantial improvement in the measurement of pressure broadening and shift parameters of molecular absorption lines.

Data Set I[14] represents the first measurements taken with the frequency comb-referenced system and includes a series of measurements of the P(11) line of the $\nu_1 + \nu_3$ band of acetylene in a temperature stabilized cell at 296 K with a temperature stability of 0.01K, at pressures up to 1 atm. Both pure acetylene and acetylene-nitrogen mixtures were studied. Using the common line shape models Voigt [44], Rautian-Sobel'man (HARD) [45, 46], and Galatry (SOFT) [47] , series of pressures are simultaneously fit using a multispectrum fitting software[48]. Pressure-dependent parameters representing broadening, shift, and, for HARD and SOFT models, collisional narrowing, were determined to higher accuracy than in previous studies for any reported acetylene line.

In order for laboratory measurements to be applicable in calibrating field measurements the temperature dependence of the line shape must also be determined. Data Set II[1] consists of pure acetylene measurements in which several temperatures between 125 K and 296 K were chosen and a series of pressures was measured at each temperature. Using the same fitting software[48] each temperature was analyzed separately. Line shape models, including Voigt, HARD, SOFT, RGP[48], and speed-dependent Voigt (SDV)[49] were tested. It was found that asymmetries in the fitted line shapes were best reproduced by the SDV model, and temperature-dependent trends were determined for the SDV fitted parameters.

Data Set III[43] includes the data from Data Set II along with temperature- and pressure-varied measurements for nitrogen-acetylene mixtures. In Data Set III, measurements are reported for all temperatures and pressures together in a single multispectrum fit in contrast to the way Data Set II was analyzed. Two closely-related SDV models were used to analyze the data and are described in detail. Fitting all the temperatures and pressures together ensures the derived parameters, in particular those with well-characterized temperature-dependent behavior,

are consistent across the entire range of experimental conditions[50]. This was not possible in the earlier Data Sets when data at each temperature were treated separately by the fitting program used. The new procedure became practicable due to the development of more efficient computer codes to analyze the data.

Depending on which model was used, the final nitrogen-perturbed line shape data are described by very few parameters described in Chapter 3.3. For the first time the temperature dependence of difficult-to-measure speed dependence parameters associated with the narrowing and asymmetry of the line are reported. The fit parameters resulting from pure acetylene and the acetylene-nitrogen mixture can together be used to model line shapes for acetylene-nitrogen mixtures over the full range of naturally-occurring concentrations, pressures, and temperatures using the extended multi-spectrum analysis. For this Data Set an attempt has been made to estimate parameter uncertainties accounting for systematic pressure measurement uncertainties. These become an important factor in determining true parameter uncertainties when other sources of error, such as in the frequency measurement, are small.

The above three Data Sets resulted in fitted parameters that are very accurate, but there is still room for improvement both in data acquisition and analysis. Presented in Chapter 4 is a Data Set taken at 296 K consisting of several acetylene-nitrogen concentrations, each measured at different total pressures. This Data Set was taken after several changes to the spectrometer reduced the noise level and baseline uncertainty contributions, and attempted to improve the pressure determination. This Data Set also made apparent a large baseline contribution of overlapping hot band transitions. In order to appropriately include these lines in the analysis, their transition frequencies must be known on the order of the accuracy of our spectrometer. Including them using positions from the HITRAN database [51] resulted in large baseline perturbations. Progress toward removing these baseline effects is presented.

Chapter 2. Experimental Details For Line Shape Measurements

2.1. Frequency Comb Principles

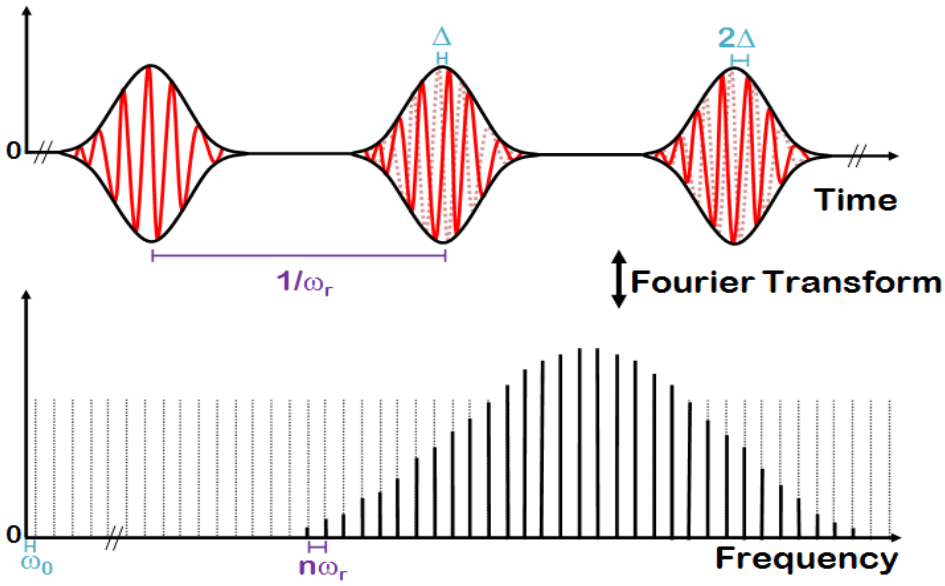

Figure 2.1: The frequency comb laser output in the time (Top) and frequency (Bottom) domains.

The frequency comb-referenced spectrometer at Stony Brook University uses a Menlo Systems FC-1500 Optical Frequency Synthesizer. A mode-locked Erbium-doped fiber laser is the main component of the frequency comb, and the evenly-spaced lines output in the frequency domain give the comb its name, as shown in Figure 2.1. The output light of the laser is very broad. The light is inserted into a cavity and only those wavelengths which are integer multiples of the cavity round trip will be resonant with cavity longitudinal modes and will produce an output. In the time domain, the output of the cavity under mode-locked conditions consists of a series of pulses of phase-matched light from all the cavity modes. These pulse envelopes are temporally separated by the round trip time of the cavity, $T=1/\omega_r$. ω_r is the repetition rate, approximately 250 MHz. However the carrier frequency within the pulse envelope travels at its phase velocity which is affected by intracavity dispersion. This causes a constant phase shift Δ from one pulse to the next.

In the frequency picture, the output consists of many lines separated by ω_r and spanning the output of the comb. The nth comb line ω_n is not an exact integer multiple of ω_r. The frequency offset from 0, ω_0, is related to Δ. The frequency of ω_n can be written as:

$$\omega_n = n\omega_r + \omega_0 \tag{2.1}$$

To determine the frequency of a comb line, n, ω_r, and ω_0 must then be determined. Determining n for the comb line nearest a CW laser locked to the comb will be described in section 2.1.2.

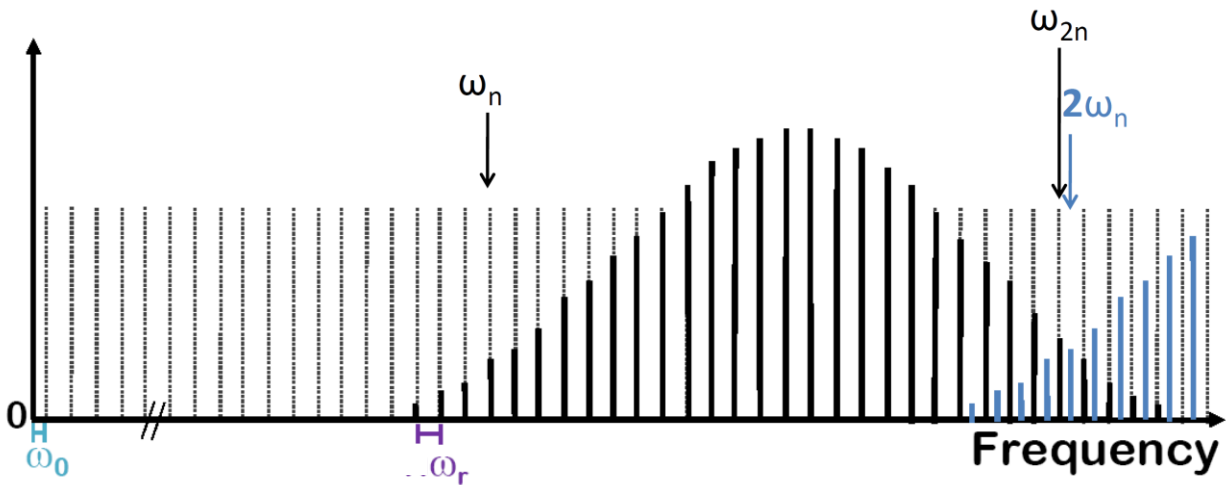

Figure2.2: Representation of the comb showing how the low end of a doubled frequency comb is compared to the high end of the comb to determine the frequency offset from 0, ω_0.

A Menlo systems GPS-612 receiver containing a local 10 MHz quartz oscillator is used as a frequency reference for all electronics essential in determining the comb's frequencies. This oscillator receives correction signals through a GPS antenna situated on the roof of the building. Satellites send out a frequency which contains a signal referenced to the hyperfine ground state splitting of cesium, giving an atomic clock absolute frequency reference with 1 part in 10^{17} accuracy.

To determine ω_0 a self-referencing technique is used. This requires the comb output to span at least an octave. The comb output is put through a fiber amplifier which broadens the comb output to approximately 1050nm-2100nm through self phase modulation[52], which is a

nonlinear effect due to high laser intensity. Shown in Figure 2.2, the broadened light is frequency doubled after passing through a periodically-poled lithium niobate (PPLN) crystal[53]. A doubled low frequency comb component, $2\omega_n$, is beat with a high frequency component of the original comb, ω_{2n}, on a fast photodiode detector. The beat note between the comb lines is:

$$2\omega_n - \omega_{2n} = 2(n\omega_r + \omega_0) - (2n\omega_r + \omega_0) = \omega_0 \tag{2.2}$$

The only condition for ω_0 is that it must be smaller than ω_r. ω_0 is locked to a direct digital synthesizer (DDS) set to 20 MHz, and referenced to the GPS atomic clock frequency.

Determining ω_r can be done using the unbroadened comb output. A fast photodiode detector detects ω_r at approximately 250 MHz. The 4th harmonic is mixed with a 980 MHz phase locked oscillator which is referenced to the GPS atomic clock frequency. The downmixed repetition rate, approximately 20 MHz, is then locked to the frequency of a referenced DDS, $f_{\omega r}$. ω_r is given by the following equation:

$$\omega_r = \frac{f_{\omega r} + 980MHz}{4} \tag{2.3}$$

ω_r can be changed by changing $f_{\omega r}$. This provides a useful tool for changing the spacing between adjacent comb lines and setting them to different frequencies.

The uncertainty of the comb is typically characterized within the comb software by a number representing the average frequency uncertainty over a 10 second interval. For the repetition rate this number is typically on the order of 10^{-3} Hz while for ω_0 under normal operating conditions this number is less than 10 Hz, but can drift as high as 100 Hz in less than ideal conditions. The comb lines of interest are near 1.5 μm and have *n* on the order of 790,000. Because ω_r represents the spacing between lines, multiplying the ω_r uncertainty by *n* yields a number close to 800 Hz, which more accurately reflects the 10 second frequency stability expected to impact experiments.

2.2. Locking a CW Laser to the Frequency Comb

The frequency comb is used as a highly accurate frequency reference for a CW laser in the experiments described here. Figure 2.1.2 A shows a basic locking scheme. The laser used here is a Sacher Lasertechnik Littman/Metcalf tunable diode laser, tunable from 1510 to 1590 nm. Coarse frequency adjustments are made manually using a tuning screw on the back of the laser head which adjusts the angle of the end mirror in a cavity defined by the diode, a fixed, near grazing incidence grating, and the mirror. More convenient scanning over smaller frequency intervals (up to 20 GHz) is done using a built-in piezo translator attached to the mirror.

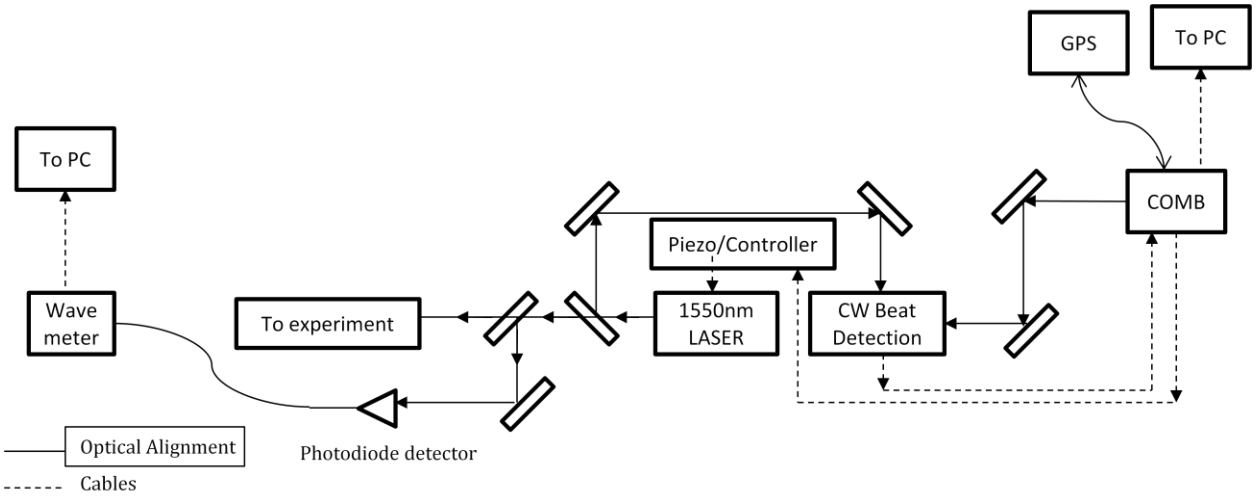

Figure 2.3: A basic diagram demonstrating the locking of a CW laser to the frequency comb.

A small portion of the light is reflected off a window to go to a wavelength meter (Bristol Instruments model 162). This gives an approximate frequency for the laser and is accurate to a quoted 60 MHz. Because this uncertainty is smaller than half of ω_r, taking the wavemeter frequency, dividing by 250 MHz, and rounding to the nearest integer will easily give the *n* for the nearest comb line from equation 2.1.

Another window takes a small portion of laser light away from the experimental beam path and into the beat detection unit. Figure 2.4 depicts the beam path within the beat detection

unit. The comb light and the CW laser light are collinear after the first polarizing beamsplitter cube within the beat detection unit. After a half wave plate and a second beamsplitter cube both beams have matched vertical linear polarization. The diffraction grating assures that only a few comb lines make it to the fast photodiode detector, which records the beat note between the CW laser and the comb. This beat note is locked to another referenced DDS, this one typically set to f_{cw}= 30 MHz. The equation for the laser locked to the frequency comb is then:

$$\omega_{CW}=n\omega_r+\omega_0+f_{cw} \tag{2.4}$$

The lock is maintained by a current modulation inserted into a Bias T on the rear of the CW laser. In order to maintain a consistent offset level for the laser current, and thus a more consistent laser intensity and locking voltage, drifts (or frequency changes due to scanning) are corrected for by using LabVIEW software to move the laser frequency using the piezo control.

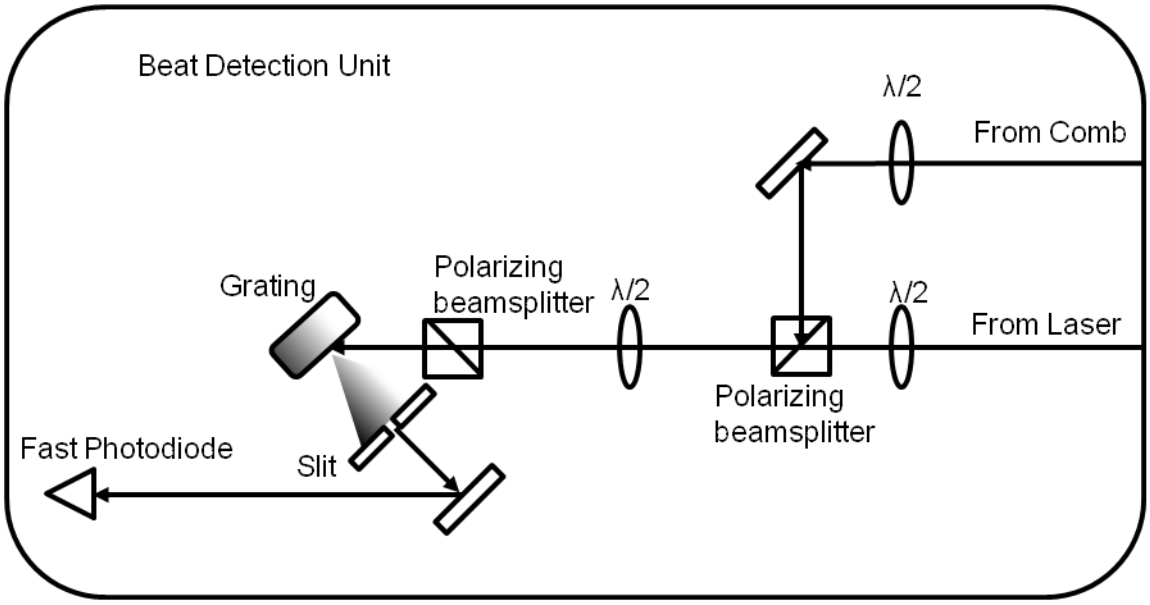

Figure 2.4: Diagram of the internals of the beat detection unit for locking the CW laser to the frequency comb.

While maintaining all other frequencies in equation 2.4 constant, a scan is done by changing the frequency of the DDS locking the repetition rate, $f_{\omega r}$, on the order of several Hz. This causes a change in the comb spacing which will change the position of a comb line near the CW laser by about (700 kHz) per Hz stepped on the DDS. Considerable effort was required to

achieve stable locking of the diode laser to the comb frequencies. The table holding the experiment was air-suspended, and large amounts of acoustical and vibrational isolation were found to be necessary. The current optical stability is typically at the level of 10-second Allan variances of between 5 and 30 Hz, as reported by the comb software. Vibrational and acoustical noise in the building and small, high frequency deviations due to noise on the repetition rate remain the limiting factors in the stability of the ECDL lock. In Chapter 4 an improved locking scheme will be discussed which improves short term stability by using a stable etalon in the locking loops.

In order to characterize the absolute accuracy and precision attainable with this system, an early sub-Doppler saturation dip measurement was made of the P(11) line in the $\nu_1 + \nu_3$ band of acetylene. The experiment confirming the stability of this system is found in section 4.3a.

2.3 Absorption Experiment

The absorption experiment involves looking at the line shapes of individual rovibration lines in acetylene in the 1.5 μm region, typically the P(11)e line of the $\upsilon_1+\upsilon_3$ band, under varying pressure and temperature conditions. The first data taken were done using a single beam path. A second detector was later added for recording the baseline level, and different techniques were used to get improved signal to noise. Other improvements include increasing the length of a single scan and locking to the comb through an etalon. The details of the experimental setup will be discussed here, as it relates to the reported data.

A. Single beam path absorption

Figure 2.5 shows the original experimental layout. The familiar comb locking was present here, with the experiment taking the majority of the CW light after the two pickoff windows. An optical isolator was placed at the beam waist to reduce back-reflections that cause diode laser instability. A 1 kHz optical chopper was placed in the beam path, before the cell. The light was focused onto a photodiode detector then fed into a lock-in amplifier. The chopper

is used to modulate the laser amplitude. When the signal is demodulated in the lock-in amplifier, a DC signal is output that relates to the amplitude of the modulation. This will reduce any noise that is not of the same frequency at which the laser is being modulated.

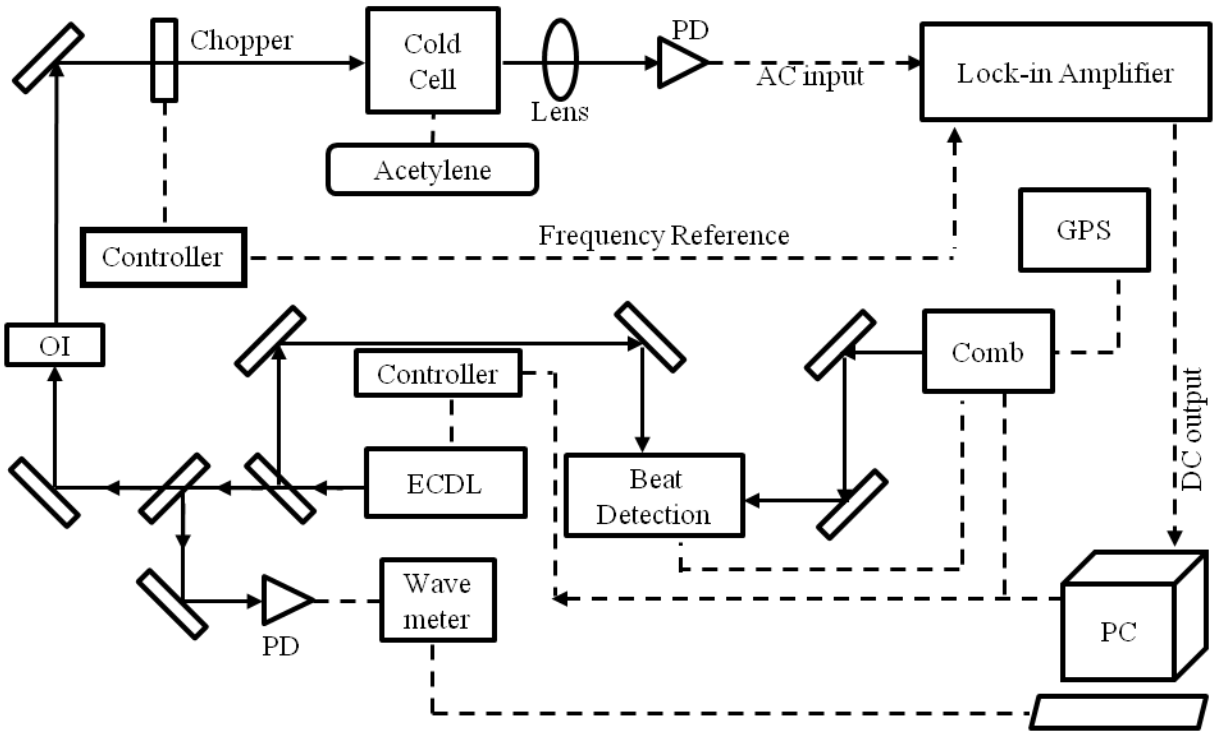

Figure 2.5: Experimental setup for the single beam line shape measurements. ECDL= Extended Cavity Diode Laser, OI= Optical Isolator, PD= Photodiode Detector. Not shown are connections for pressure and temperature sensors in the cell.

Figure 2.6 shows example data taken with the single beam setup. The signal-to-noise ratio here is about 150. The system noise here is dominated by amplitude fluctuations in the ECDL power which directly affect the measured signals. In order to maintain a large enough bandwidth in the frequency stabilization loop locking the laser to the comb, it was necessary to apply the feedback corrections to the diode current. This correction signal also causes proportional power fluctuations in the laser output accounting for most of the recorded noise. Almost all the noise in the system at frequencies above a few hundred Hz is due to this effect. Since this noise appears in both data channels, using a dual beam configuration is more practical and eliminates this ECDL amplitude variation.

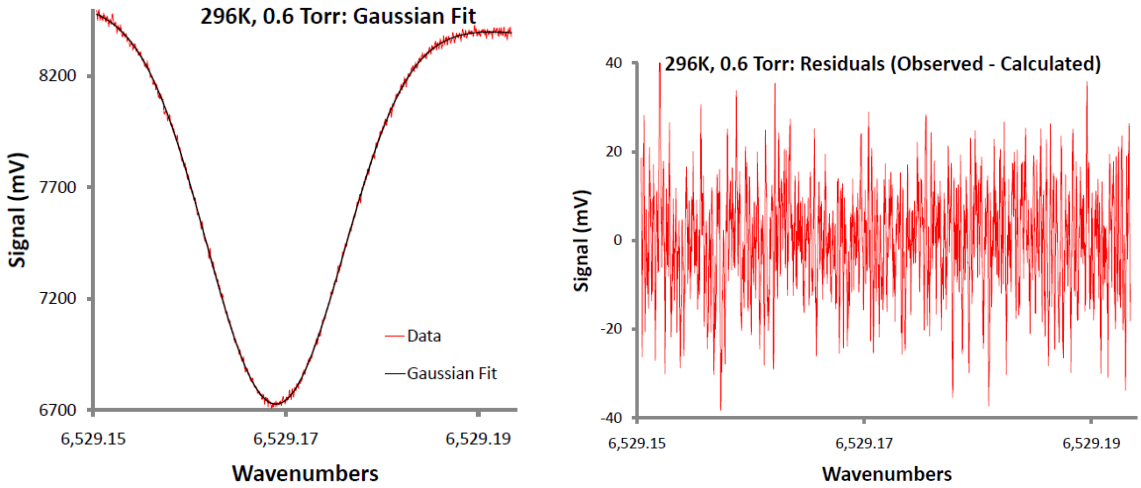

Figure 2.6: (Left) Data obtained using single beam absorption of the P(11) line of the $\upsilon_1+\upsilon_3$ band of acetylene. A line from a fit to a Gaussian line shape is also shown. (Right) Observed - Calculated residuals resulting from the Gaussian fit.

B. Dual beam path absorption

Figure 2.7 shows the experimental arrangement. The laser beam was optically chopped at 50 kHz using an electro-optic amplitude modulator (EOAM, New Focus model 4104 broadband modulator) and polarizing optics in place of the chopper used previously. The EOAM contains a crystal whose polarization-dependent refractive index changes with applied voltage. As one axis is slowed relative to the other by increasing voltage, input vertically polarized light will go from elliptical, to circular, and eventually to horizontally polarized output light. The polarization is switched at the 50 kHz modulation rate by putting a 50 kHz sine wave of appropriate amplitude into the EOAM. In the setup above, vertical polarizers are placed before and after the EOAM, resulting in a high frequency, and more consistent, optical chopper.

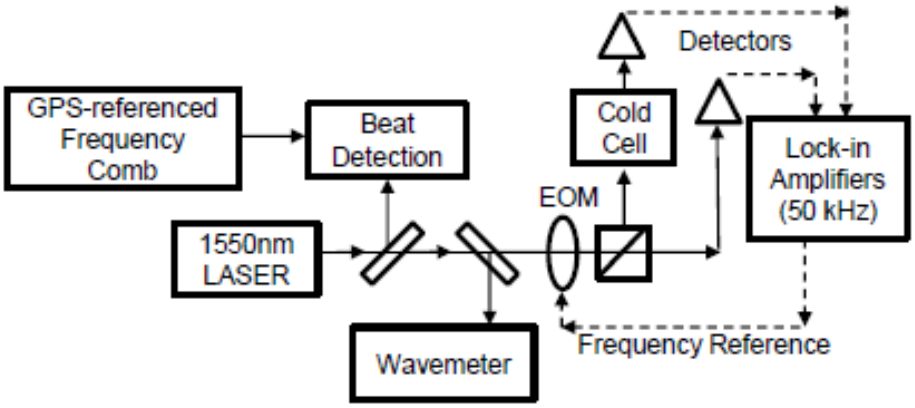

Figure 2.7: Simplified block diagram of the experimental set up for the dual beam line shape measurements. Abbreviations are as in Figure 1 and EOM = electro-optic amplitude modulator. Not shown are connections for pressure and temperature sensors in the cell that are monitored and recorded at all times during measurements.

After the EOAM the probe laser beam is split into two beams, which serve as the signal and reference, using a rotatable half-waveplate and beamsplitting polarizer cube. The two beams were separately imaged onto two identical InGaAs-based 10 MHz receivers (New Focus model 2053). The power imaged on the two detectors was matched under conditions of no signal absorption, using the waveplate. The absorption in the signal and reference beams was then detected as the phase independent magnitude ($R^2 = X^2 + Y^2$) of the demodulated 50 kHz 1 f signals using two identical two channel digital lock-in amplifiers (SRS model 830), and the ratio of the two yielded the transmission line profile directly. Signals from the two lock-in amplifiers were separately saved for later analysis. No recorded noise was noted that was associated with mechanical vibrations of the cell in the signal when collecting a spectrum. This was tested by collecting a data set with the refrigerator turned on and off. However, the spectrometer lock is sensitive to acoustic noise, and precautions were taken to provide insulation against the acoustic noise from the mechanical refrigerator and compressor.

An upper limit of the laser line width can be determined. Figure 2.8, upper trace shows a scan recorded at approximately 0.1 Torr in the 16.551 cm cell. A maximum value was estimated for the emission line width by fitting these data to a Gaussian line shape convoluted with a Lorentzian representing the laser. The lower trace in Figure 5 shows the observed minus calculated (O-C) residuals from the fit. The results suggest that the laser line width is smaller

than 8.3 (2.3) x 10^{-6} cm^{-1}, or approximately 250 kHz. With a 250 kHz line width the residuals appear flat. This result depends upon the S/N in the spectral file. Higher S/N yields smaller maximum values for the emission line width. This can be easily understood because with higher S/N it is possible to observe smaller residuals deviating from a flat observed minus calculated (O-C) plot of the experimental and calculated spectrum. 250 kHz is larger than typical for the comb-stabilized laser, due to the comparatively fast scan speed with low averaging needed to complete the measurements. At slower scanning rates such as those used in the line center measurements an upper limit to the HWHM of 105(2) kHz [14] was measured. S/N calculations are described in Chapter 2.3 F.

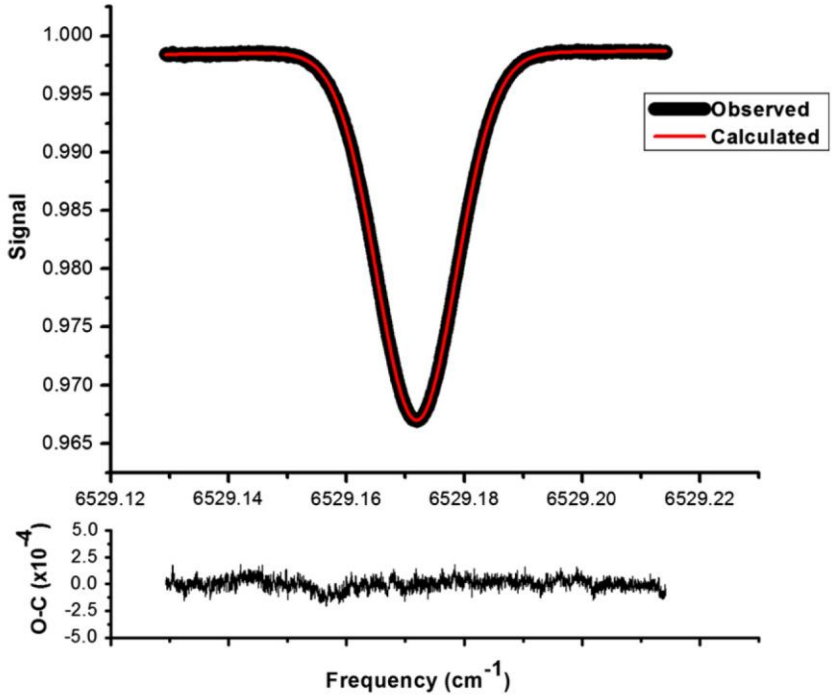

Figure 2.8: A low pressure (~0.1 Torr) scan over the P(11) line of pure acetylene in a 16.551 cm cell recorded at 296 K and used to determine an upper limit to the laser line width. The upper panel shows the experimental spectrum as well as the calculated (Gaussian) spectrum, while the lower panel shows the residuals (observed – calculated) resulting from subtraction of the calculated spectrum from the experimental spectrum.

C. Cell Details

The interchangeable absorption cells used in this experiment are similar in design to others described previously[54]. They are fabricated from OFHC copper. The cell is mounted on a temperature controlled copper mount attached to a CTI Model 22 closed cycle helium cooled cold finger. The cell is thermally isolated and mounted inside a vacuum box that is maintained at high vacuum by diffusion and mechanical pumps and by cryopumping in the case of a low temperature cell. The cell and vacuum box windows are wedged CaF_2. The wedge angle is 30 arc minutes, and the window clear aperture is 4.45 cm. The wedged window produces no measurable optical fringes. The cell windows are sealed to the copper cell body using a compressed indium metal seal. The sample gas is introduced into the cell through a 6 mm diameter stainless steel tube with 0.102 mm wall thickness. The tube is 38 cm long and is silver soldered to the copper cell body. Since copper heat conductivity is among the best of all metals, 4.01-5.57 W/(cm-K) between 80 and 296 K, no significant temperature gradient across the cell was observed in separate performance tests on each cell. Cell lengths used (at 296 K) were 1.085 cm and 16.551 cm, depending on experimental temperature and pressure conditions and desired absorption. Length measurements were made with a precision micrometer with estimated errors of +/- 0.0005 cm.

D. Temperature and Pressure Control

To maintain constant temperature, the He cooling of the cell is balanced by a 50 Ohm heater capable of supplying up to 50 Watts power. The cell temperature is controlled with a model 331 temperature controller (Lakeshore Cryotronics Inc.) and a silicon diode sensor mounted on the copper block located between the cold finger and the copper cell for feedback to the proportional, integral and derivative (PID) temperature control loop. A second sensor is placed on a lateral side of the cell midway between the two windows. The signal from this second sensor provides the actual cell temperature. The sensors utilized here were calibrated with an accuracy of 0.125 K at 77K and 0.105 K at 300K. The parameters for the PID temperature control loop were set automatically at each set point temperature. The temperature stability of the cell is typically less than 0.01 K for long periods, even with modest cryodeposits.

An MKS model 690A013TRA 0–1000 Torr Baratron capacitance manometer gauge head, with certified accuracy of better than 0.04% across the entire range was used for pressure measurements. However, zero offset drifts of up to 0.5 Torr were noted over periods of days during which data were collected. A portion of the data was recorded using an older gauge (MKS 310BHS 1000 Torr). These data, which include Data Set I and a small portion of Data Set II (see below for Data Set descriptions), were corrected based on calibrations using the new gauge resulting in an estimated accuracy of 0.5% for these measurements.

The cell temperature and sample pressure inside the cell are continuously recorded during a scan, and samples of such data files are plotted in Figure 4. Typically both the temperature and pressure are very stable throughout the experiment, with variations less than within the quoted accuracy over the duration of a scan.

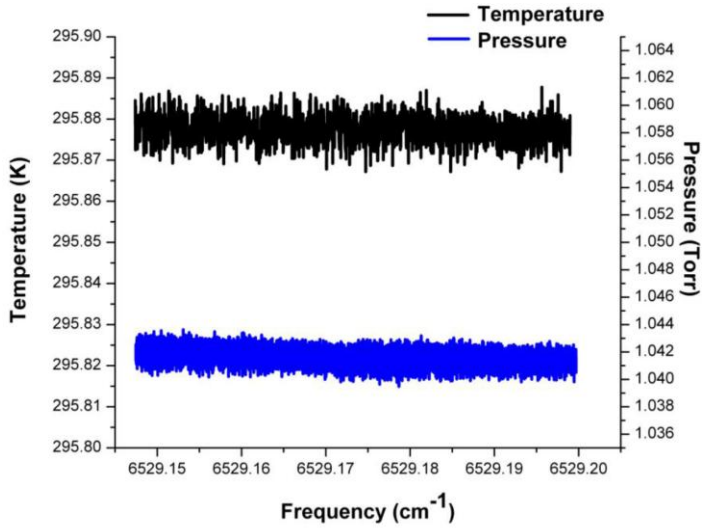

Figure 2.9: Cell temperature and sample pressure data recorded during a typical spectral scan. Average temperature is 295.877(3) K, average pressure is 1.0416(6) Torr, where uncertainties are expressed as one standard deviation in units of the last digit.

E. Data Acquisition

The following 3 data sets contain results obtained using the dual beam setup. Pure acetylene gas (>99.6%, MG gases) was used, and the residual acetone was removed by a cold trap maintained at 178 K before use. Several samples were checked by mass spectrometry to ensure purity. Nitrogen gas (Matheson, extra dry) was used without further purification. In gas mixtures, profiles were typically recorded using a high pressure sample of nitrogen containing a low concentration of acetylene at a given temperature and repeated at successively lower pressure as fractions were pumped out, maintaining the original concentration.

The spectrometer operation is entirely controlled by computers running LabVIEW (National Instruments) programs. The optical comb software (Menlo Systems) controls the operation of the frequency comb, in combination with home-developed software to control the scanning and acquire data. The data were collected with an optical step size of 0.78 MHz - 12.48 MHz. A single optical scan could be up to 2.1-2.5 GHz long, limited by the available servo-lock voltage controlling the comb laser cavity length. However, due to the extreme stability of the spectrometer, several files were routinely concatenated to produce a continuous, or nearly continuous, scan over the high pressure lines. For the lines measured at the highest sample pressures, as many as seven spectral files were concatenated to cover approximately 0.49 cm^{-1}.

I. Data Set I

Data Set I contains data for gas compositions of pure acetylene and acetylene in N_2, all at 296 K. Data is taken at varying pressures so that pressure-dependent line shape parameters can be determined. Data files included at least 2500 points covering approximately 2.1 GHz. Larger step sizes were attempted in order to collect data files with fewer data points per scan in a shorter time, but the ECDL would not remain locked under these conditions. All data were collected with a time constant of 30 milliseconds.

26 pure acetylene spectra and 22 spectra of nitrogen/acetylene mixtures were analyzed and the data are summarized in table I. Acetylene concentrations for acetylene-nitrogen mixtures were near 1.2%.

Table 2.1: : Summary of data fitted for Data Set I, including cell path lengths and total gas pressure (Torr). Temperature = 296 K.

Pure Acetylene: 26 Spectra			N_2 broadened: 22 Spectra	
Gas Pressure (Torr)	Spectra Fitted	Pathlength (cm)	Spectra Fitted	Pathlength (cm)
0 to 1	4	16.551		
2 to 50	3	1.085		
50-100	6	1.085	3	16.551
100-200	5	1.085	3	16.551
200-340	8	1.085	3	16.551
400-450			5	16.551
500-770			8	16.551

II. Data Set II

Data Set II contains pure acetylene measurements made at varying temperatures. Table 2.2 summarizes the entire set of experimental conditions under which spectra were recorded and analyzed. Note that maximum acetylene pressures at gas sample temperatures below 175 K were limited by the vapor pressure of acetylene. Cell length was 1.085 cm. for all measurements, and step sizes were similar to those in Data Set I.

III. Data Set III

For the most recent data (about 1/3 of Data Set III) the number of data points was reduced by using 16 Hz repetition rate steps between each acquisition point. A fast series of micro steps were made between each data point to maintain the comb-laser lock, and improved software checked for system stability before beginning the acquisition at each point. This allows for data files that contain 75% fewer points. A telescope in the beam of the ECDL probe was

added to reduce the beam divergence and improve the transmission through the narrow aperture optics such as an electro-optic modulator. These changes led to reduced analysis time by reducing the number of data points, and significantly improving the overall data quality.

Table 2.2: Number of acetylene absorption spectra used in the data analysis for Data Set II listed by corresponding experimental conditions.

Pressure Range (Torr)	296 K	240 K	200 K	175 K	165 K	160 K	155 K	150 K
5- 20	1	-----	2	-----	1	2	5	5
20-50	5	3	3	5	2	3	-----	-----
50-75	7	7	6	7	3	1	-----	-----
75-150	6	6	7	9	10	-----	-----	-----
150-300	5	11	13	20	-----	-----	-----	-----
300-500	8	7	7	-----	-----	-----	-----	-----

For these experiments, measurements in samples with low acetylene concentrations, i.e. from 0.01% to 2.5% were taken using a 16.551 cm (measurements are at 296 K) cell. A shorter 1.085 cm cell was used for measurements at high (25% or 50%) acetylene concentrations, which were later omitted from the analysis for reasons described in Chapter 3. Some example spectra are shown in Figure 2.10.

Table 2.3: The number of data files used, and experimental conditions, for the self- / N2-collisions fits for Data Set III. A total of 152 files were included in the self-collision dataset, and 199 files for the C2H2-N2 measurements. In both cases, the pressure listed represents the full pressure of the sample.

Pressure Range (Torr)	296 K	240 K	200 K	175 K	160 K	140 K	125 K
5- 20	2	2	---/5	---/1	---/1	2	5
20-75	7	6	10/5	12/6	6/5	5	3
75-150	3	4	4/4	9/3	8/3	3	---
150-300	3	4	5/4	20/3	---/3	5	---
300-500	5	5	2/5	---/5	---/5	---	---
500-770	26	12	---/12	---/11	---/12	12	---

It was necessary to include the earlier pure acetylene broadening measurements from Data Set II to account for the small partial pressure of acetylene present in Data Set III measurements. The vapor pressure of acetylene[55] limited measurements to minimum temperatures of 150 K and 125 K for pure C_2H_2 and N_2-broadened samples, respectively. At 125 K the vapor pressure of acetylene is only 0.4 Torr. For pure C_2H_2 a total of 67 line measurements were made in a total of 152 segments. Pressures ranged between 3 Torr and 350 Torr. The N_2-broadened C_2H_2 data set includes 62 line measurements made in a total of 199 segments. Concentrations between 3% and 0.3% were included in the final fit dataset. Total mixture pressures ranged from 5 Torr to 750 Torr.

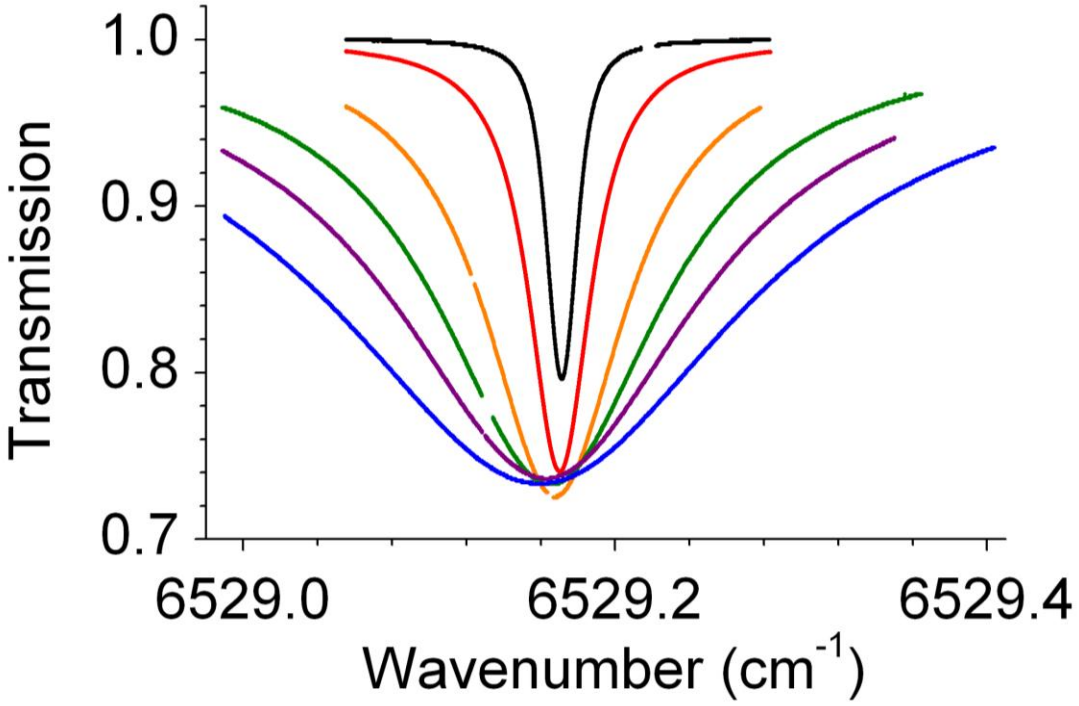

Figure 2.10: Example spectra taken at a concentration of 1.3% C_2H_2 in N_2 at 175 K. Overlaid in the plot are the raw experimental data between 33 and 750 Torr. Due to instrumental constraints broader line shapes needed to be taken in several segments and were later concatenated, leaving small gaps where no data exists.

F. Spectral signal-to-noise

Since signal-to-noise is a very important consideration when measuring absorption line parameters, especially in determining pressure dependent parameters for molecular absorption lines, it is examined in some detail in the results. First the root mean square error (RMSE) of a set of data points X_i needs to be defined. A standard definition for this parameter is

$$RMSE = \sqrt{\frac{\sum_{i=1}^{N} (X_i - X_{AVG})^2}{N}} \tag{2.5}$$

where X_{AVG} is the average value of the points, or

$$X_{AVG}^2 = \left(\frac{\sum_{i=1}^{N} X_i}{N} \right)^2 \tag{2.6}$$

So, the Signal to Noise ratio, S/N, is the ratio of the average value of the data points, divided by the RMSE:

$$\frac{X_{AVG}}{N_{RMS}} \tag{2.7}$$

Figure 2.11 demonstrates graphically the results from the above discussion. The upper trace shows raw data points in a short scan of an empty cell. Superimposed on this array is a least squares fit to the data from which an average value is calculated. The average value is calculated to be 1.0063(3) using equation 2.6**.** The bottom panel in Figure 2.11 shows the observed minus calculated (O-C) plot obtained by subtracting the two plots in the upper panel. From the lower plot the RMS noise is calculated to be 8.7×10^{-5}, using equation 2.5, and the S/N is determined to be about 11,600, using equation 2.7. Michelson interferometer-controlled tunable diode laser (TDL) measurements routinely achieve fits within the noise level of 0.1% [56]. Data obtained using Fourier transform spectrometers are practically limited to about 0.05 % [57].

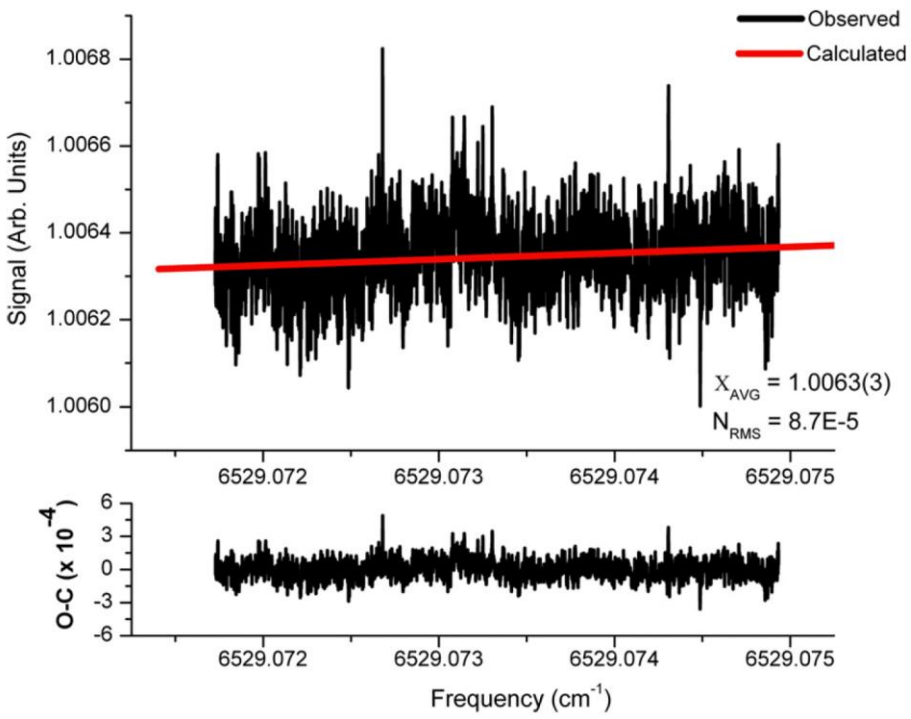

Figure 2.11: Spectral scan used to determine the typical spectral signal-to-noise ratio in a spectrum. The average value is calculated from fitting the experimental spectrum in the upper panel, and the RMS noise is calculated from the observed minus calculated plot (O-C) in the lower panel and the ratio results in a S/N of 1.160×10^4.

Chapter 3: Line Shape Modeling, Data Analysis, and Results

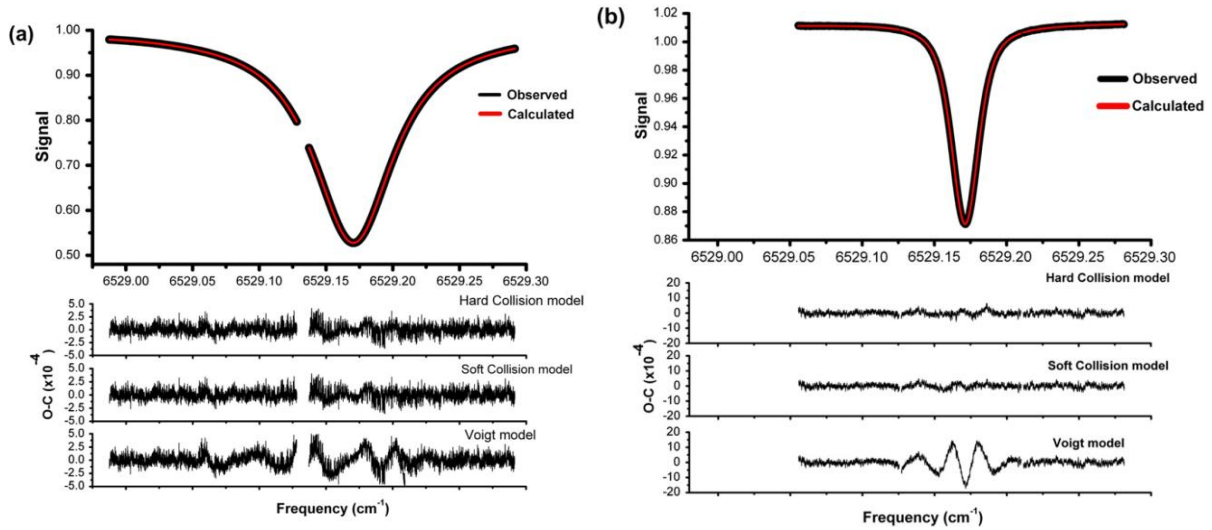

Figure 3.1: **a)** Set of 5 concatenated spectral files (total pressure: 155 Torr, 100% C_2H_2, 296K, path length=1.085 cm. The gap in the scan illustrates the stability of the spectrometer. **b)** Set of 3 concatenated spectral files (total pressure: 54 Torr, 1.26% C_2H_2, path length=16.551 cm. The effect of collisional narrowing at line center is clear at this pressure. In both panels, the spectral files are shown in the upper panel and the O-C plot in the lower panel is the result of subtracting the fitted spectrum from the experimental spectrum.

3.1 General Line Shape Model Theory

A satisfactory line shape model needs to be able to account for observed line shapes over the entire range of temperatures, pressures and concentrations. In the high pressure limit, many standard line shape models perform well as they correctly predict a limiting Lorentzian profile:

$$\Gamma_L(\omega) = \frac{\pi^{-1}\gamma_L}{(\omega - \omega_c - \delta_L)^2 + \gamma_L^2} \tag{3.1}$$

where γ_L and δ_L are the pressure- and temperature- dependent width and shift parameters, and ω_c is the unperturbed line center, all in units of cm^{-1}. Physically γ_L is a dephasing effect resulting from collisions which interrupt the absorption process, causing broadening as a result of the uncertainty principle. δ_L is a shift in the line center as increasing intermolecular collisions affect the upper and lower states in the absorption differently, causing the transition energy to change.

At the low pressure limit, much lower than 1 Torr, line shape models must predict a profile where pressure broadening is negligible in a nearly collisionless environment. The Doppler line shape is observed corresponding to varying absorption energy due to the molecular velocity distribution relative to the beam path:

$$\Gamma_D(\omega) = \frac{1}{\sqrt{\pi}\omega_D} e^{-\left(\frac{\omega^2}{\omega_D^2}\right)} \tag{3.2}$$

$$\omega_D = \frac{\omega_0}{c}\left(\frac{2k_B T}{M}\right)^{\frac{1}{2}} \tag{3.3}$$

where ω_D is the Doppler width (cm^{-1}) defined by eqn. 3.3, with temperature *T*, absorber Mass *M*, Boltzmann constant k_B, and speed of light *c*.

Actual measured line profiles of interest are at intermediate pressures and will not match either simple profile, and can be difficult to predict and so the choice of line shape model is important. Here the effects of collisions on the observed line shape depend on various intermolecular interactions that have been modeled using a number of different assumptions and derived parameters. For a model to be useful for extracting species concentration data from remote sensing measurements these interactions need to be described with parameters that scale in a well-defined way with changing pressures and temperatures.

The simplest such model is the Voigt profile[44, 58], a convolution of Gaussian and Lorentzian line shapes:

$$\Gamma_V(\omega) = \int_{-\infty}^{\infty} \Gamma_D(\omega')\Gamma_L(\omega - \omega')d\omega' \tag{3.4}$$

γ_L and δ_L are the parameters which are typically allowed to vary when using the Voigt since ω_D consists entirely of well-known constants or parameters that depend on experimentally measured values. The Voigt profile has well-known deficiencies due to its neglect of collisional narrowing

that is commonly observed at low to intermediate pressures[59], resulting in erroneously small estimates for $\gamma(T)$. Systematic W-shaped deviations[44] between the calculated and observed line shapes are characteristic of the Voigt profile, an example is shown in Figure 3.1. At higher pressures above a few hundred Torr, the Voigt does a much better job as the line shape, and model, begin resembling a Lorentzian.

The collisional narrowing, most easily observed at pressures below about 40 Torr but having an increased effect at higher pressures, is due to velocity changing collisions which have a higher probability of leaving both molecules involved in a collision with velocities closer to the average [44], or center of the velocity distribution. This is referred to as Dicke [60, 61], or confinement, narrowing, and characterized commonly by the temperature- and pressure-dependent velocity-changing collision rate, γ_{Dicke}. As pressure increases, this effect tends to increase, but becomes hidden by the much larger broadening γ_L. γ_{Dicke} is typically a fitted parameter in models which include a narrowing effect but it may also be estimated from the mass diffusion constant D_m [62, 63]:

$$\gamma_{Dicke} = P\frac{k_B T}{2\pi c m_a D_m} \tag{3.5}$$

for pressure P, temperature T, and absorber mass m_a. Values for D_m can be calculated from reference [62] eqn. 8.2-20 using Appendices I-A and I-M to obtain relevant values.

More sophisticated line shape models, such as the hard-collision (Rautian-Sobel'man[45, 46, 64]), soft-collision (Galatry[47]), and hybrid hard/soft- (RGP) collision profile [48, 65] include γ_{Dicke}. Models which include a narrowing mechanism result in larger γ_L values because models such as the Voigt, with no narrowing, attempt to compensate with artificially smaller γ_L. The HARD model corresponds to the limiting case where the perturbing molecule is much heavier than the absorber, and a significant velocity change of the active molecule requires only one or a few individual collisions. By contrast, the SOFT model corresponds to the case where the perturbing molecule mass is much smaller than the absorber mass, and a significant change in the absorber molecule velocity requires many individual collisions. Large variations in γ_{Dicke}

may be observed when describing soft or hard collisions at low pressures or when correlations exist between velocity changing and dephasing collisions; because of this γ_{Dicke} is larger when using SOFT than the HARD model. Line shifts are also included in these models, but do not significantly depend on the model. Distinct differences were seen in the residual plots in highly precise data recorded at different temperatures with frequency stabilized tunable diode laser systems [66] as well as in present data as shown in Figure 3.1. Absorption profiles characterized by Voigt or HARD/SOFT models are always symmetric about the center, unless the absorption feature is a blend of more than one line.

Analysis of the higher pressure spectra recorded with the current spectrometer using the line shape models previously discussed have nearly identical residuals. However, as described below, it is found that the residuals at the lowest temperatures and pressures are the result of inadequacies in the line shape modeling, and not the result of instrument limitations or spectral signal-to-noise. In particular, residuals display a clear asymmetry and systematic features near line center. One model that addresses the asymmetry is the Speed-Dependent Voigt (SDV) model[49]. This line shape model, taken directly from Ward et al.[49], treats collisions at different speeds as interacting with different parts of a spherical intermolecular potential, *V*, approximated by an inverse power, *q*, of the intermolecular distance, *r*, and assuming straight line trajectories, $V \propto r^{-q}$. The temperature- and pressure- independent parameter, *q*, accounts for both speed-dependent narrowing and asymmetry in the line shape. For many physical models of the intermolecular potential, a value of *q* near 6 is expected and qualitatively this has been observed. Qualitatively the speed-dependent narrowing is the result of slower-moving molecules, which tend to be nearer to the center of the velocity distribution, having fewer de-phasing collisions (which cause the collisional broadening effect associated with γ_L) than those far away from the center. Similarly, the asymmetry represented here is due to the collision-induced shift being more pronounced in the regions of the line profile associated with higher velocity molecules, which have more collisions[67]. This particular asymmetry effect will always result in a profile with greater intensity toward the direction of the shift. Asymmetry has also been reported in measured line profiles of water[68] and acetylene[69]. Aside from the effect of speed dependence on the shift, correlations between velocity-changing and phase-changing collisions in the context of a Dicke narrowing model can also result in asymmetry[70]

and a separation of the effects of these possible mechanisms has been a focus of several recent studies[69, 71, 72]. The fitted parameters dictating the SDV line profile are γ_L, δ_L, and q.

Aside from the SDV, other models were initially considered to account for the observed asymmetry in the residuals. Another model which takes into account speed-dependent effects on collisions is the weighted sum of Lorentzians profile (WSL) [73, 74]. Dicke narrowing changes the distribution of molecular velocities, and so including it in a model would affect speed-dependent parameters. In cases where both narrowing effects, are considered, product models denoted by WSL*SOFT [71, 75] or WSL*HARD [75] are used. These are the result of convolution products of a WSL profile with a confinement narrowed profile described by the SOFT [47] or the HARD [45] model. Ciurylo et al. [65] developed a model to describe intermediate cases where a generalized speed-dependent line profile combines soft and hard partially correlated Dicke-narrowing collisions (csdRG). The parameter, ε, is introduced in the csdRG model to describe the hardness of the velocity changing collisions, ε=0 describes a pure soft collision and ε=1 describes a pure hard collision. Intermediate cases correspond to 0<ε<1. Hurtmans et al. [76] adopted the use of the so called "mean persistence velocity ratio", u_{12}, defined by Chapman and Cowling [77] to take into account the intermediate case perturbing mass ratio. Using Hurtmans et al.'s approach, $\varepsilon_{calc}=1-u_{12}$, with ε_{calc} fixed during the fitting process. The mean persistence velocity ratio is the ratio of the mean value of the velocity of the active molecule, mass m_1, after collision, to its velocity before collision. For hard spheres this ratio is equal to

$$\mu_{12} = \frac{1}{2}M_1 + \frac{1}{2}M_1^2 M_2^{-\frac{1}{2}} \ln[(M_2^{\frac{1}{2}}+1)M_1^{-\frac{1}{2}}] \tag{3.6}$$

with $M_1=m_1/(m_1+m_2)$ and $M_2=m_2/(m_1+m_2)$. In the hard collision limit $\mu_{12}=0$, and μ_{12} increases to $\mu_{12}=1$ in the soft collision limit as the ratio m_1/m_2 of the mass of the active molecule to the perturber mass increases from zero to infinity. When both masses are equal, as is the case in this paper, $\mu_{12}=0.594$. A model termed the Speed-Dependent Galatry[78-80] profile (SDG) was also considered in Data Set III. This model is capable of including speed-dependent effects along with Dicke narrowing. Unlike the SDV model mentioned above, the speed-dependent narrowing

γ_2 and shift δ_2 are dictated by separate parameters. This means the SDG has 5 parameters dictating the line profile: γ, δ, γ_{Dicke}, γ_2, and δ_2. In the case where Dicke narrowing is fixed to 0 this model reduces to an SDV profile, which is called the Q-SDV here (because of the quadratic form of the speed dependence-see Chapter 3.2). It is unique amongst the models mentioned here in the analysis because it is evaluated in the time domain.

3.2 Model Choices

A. Data Set I

For Data Set I, Voigt, HARD and SOFT models were chosen for analysis. This was the first data examined so no more complicated models were yet being considered.

B. Data Set II

Described in Chapter 3.5 is the data analysis program used for Data Sets I and II, which includes built-in functions for all the above-mentioned models except Q-SDV. In analyzing the data for Data Set II all of these models were considered but only reported results from the HARD, RGP, and SDV models. Experimentally, line shape asymmetries were apparent, especially at low pressure, but at all temperatures. Line shape models that include correlations between velocity changing and dephasing collisions such as in [81] did *not* describe the observed asymmetries, and their results were not reported to keep the analysis more relevant. Instead, models were pursued that include speed-dependent effects to describe the asymmetry, because they resulted in the minimal residual features.

Line shape models that include collisional narrowing, like SOFT, HARD, or RGP, are completely symmetric, and because of this, these models failed to reproduce the spectral asymmetry at intermediate pressures and temperatures. On the other hand, models including speed-dependence as well as collisional narrowing, like the WSL*SOFT or WSL*HARD, or the csdRG model, added asymmetry to the line shape, but over-emphasized the narrowing compared

to the experimental observations here, and didn't provide improvements despite their higher complexity.

C. Data Set III

The SDV model was used here since it produced the smallest residuals with Data Set II. Additionally the Q-SDV profile was used. Both models fit this extensive data set to close to the experimental noise, i.e. a fractional noise of $1x10^{-4}$.

3.3 Line Shape Parameters

Between the 3 data sets parameters are reported for Voigt, HARD, SOFT, RGP, SDV, and SDG. Table 3.1 lists the parameters along with which models they are found in. The pressure- and temperature- dependent parameters have units of cm^{-1} and include all but q. These parameters are all expected to follow a linear trend with pressure. Each gas in a mixture will contribute to the line shape and it is often useful to express them as a pressure- weighted sums of the individual gas parameters. Using broadening γ_L as an example:

$$\gamma_L = \sum_{i=gas} p_i[\gamma_i(T)] \tag{3.7}$$

is a sum of broadening contributions $\gamma_i(T)$ (cm^{-1} $atm.^{-1}$) from contributing collision partners, weighted by p_i, the partial pressure of component gas i.

Data sets II and III include measurements at several temperatures. The individual component broadening or shift parameter are expected to vary from one gas to the next, and the temperature dependence is expected to vary also. $\gamma_i(T)$ is assumed to have a temperature dependence consistent with that used in the HITRAN database[82] (and this is verified in the Data Set II analysis). Using :

$$\frac{\gamma_i(T)}{\gamma_i(T_0)} = \left(\frac{T_0}{T}\right)^{n_{\gamma i}} \tag{3.8}$$

where $\gamma_i(T)$is the broadening at a given temperature T (K) for gas i, in cm^{-1}/atm., T_0 is the reference temperature (296 K here), and $n_{\gamma i}$ is the temperature-dependence exponent to be fit. Several assumed descriptions for temperature dependence of $\delta(T)$ have been used in the past[83, 84]. There is a possibility that the shift parameter may pass through zero at certain temperatures for some systems and a linear (or polynomial) function in the temperature can be used to fit the observations[83]:

$$\delta_i(T) = \delta_i(T_0) + \delta'_i(T - T_0) \tag{3.9}$$

with δ'_i as the temperature dependence parameter to be fit. Either model (eqn. 3.8 or 3.9) is empirical. In Data Set II the more used eqn 3.9 was used but a variation of the power law of eqn. (3.8) was chosen for $\delta_i(T)$ to model the shift in Data Set III because it resulted in a slightly better fit than the linear model and is consistent with the broadening parameter. As part of the data analysis in Chapter 3.7 the temperature dependence of $\gamma_2(T)$ and $\delta_2(T)$ will be explored since prior experiments have not investigated the trends expected for these parameters.

Table 3.1 Summary of fitted parameters and the reported line shape models which use them.

Param.	Description	Units	Voigt	HARD	SOFT	RGP	SDV	Q-SDV
γ_L	Broadening	cm^{-1}	X	X	X	X	X	X
δ_L	Shift	cm^{-1}	X	X	X	X	X	X
γ_{Dicke}	Dicke Narrowing	cm^{-1}		X	X	X		X
q	Speed dependence						X	
γ_2	Speed-dependent width	cm^{-1}						X
δ_2	Speed-dependent shift	cm^{-1}						X

In the SDV profile the total broadening and shift parameters for any given absorber speed were calculated slightly differently as the sum of the pressure-weighted contributions of each present molecule, multiplied by a unitless function, $\beta(v_a,q)$:

$$\gamma_L = \sum_{i=gas} p_i[\gamma_i(T)\beta_i(\nu_a, q)] \tag{3.10a}$$

from Ward et al.[49], Eqn. 7.7:

$$\beta_i(\nu_a, q) = (1+\frac{m_p}{m_a})^{-\frac{q-3}{2q-2}} \sum_{n=0}^{N} \frac{\left(\prod_{j=0}^{n-1} -\frac{q-3}{2q-2}+j\right)\left(-\frac{m_p \nu_a}{m_a \nu_{a0}^2}^2\right)}{\left(\prod_{j=0}^{n-1} \frac{3}{2}+j\right) N!} \tag{3.10b}$$

where m_p is the perturber mass, m_a is the absorber mass, v_a is absorber speed, and v_{a0} is the most probable absorber speed $(2\ k_B\ T\ /m_a)^{1/2}$. Care must be taken to choose N to be large enough for $\beta(v_a,q)$ to converge. In the SDV model, a convolution over all absorber speeds gives the line shape.

The approximations giving rise to the q parameter in SDV are not physically realistic but real deficiencies in the line shape modeling results appear, as discussed below. For this reason the analysis of Data Set III includes a special case of the Speed-dependent Galatry model, the Q-SDV model, parameterized in the time domain, which includes separate empirical parameters for speed-dependent narrowing and asymmetry and described in detail previously (Forthomme et al.[85] c.f. equations [2-7]). The essential elements are described below. In common with other recent reports[78, 86], due to the strong correlation between parameters representing the two narrowing effects, it has not been possible to allow both to vary in the analysis. The Dicke narrowing parameter (γ_{Dicke}) has been set to zero here, hence the name Quadratic Speed-Dependent Voigt (Q-SDV), derived from the quadratic form assumed for the speed dependence of the relaxation rate when averaged over collider velocities. In the Q-SDV model, a phenomenological relaxation rate (in s^{-1}) depending on the pressure- and temperature- dependent parameters (Γ) is given by the form[87]:

$$\Gamma(\nu_a) = \Gamma_0 + \Gamma_2\left[\left(\frac{\nu_a}{\nu_{a0}}\right)^2 - \frac{3}{2}\right] \tag{3.11}$$

where Γ_0 is the speed-independent portion of the relaxation and Γ_2 is a parameter characterizing the speed-dependence of the complex relaxation rate. The real and imaginary parts of Γ_0 give the broadening and shifting, while real and imaginary parts of Γ_2 give the narrowing and asymmetry according to:

$$\Gamma_0 = 2\pi c\left[\gamma_L - i\delta_L\right] \tag{3.12}$$

$$\Gamma_2 = 2\pi c\left[\gamma_2 - i\delta_2\right] \tag{3.13}$$

This model, while not specifically identifying parameters with specific individual physical interactions, does remove restrictions that the SDV model creates because of its direct link between narrowing and asymmetry. Additionally, the four parameters are effective in qualitatively describing observed perturbations to the line shape and the derived parameter values can be assessed with respect to their physical origin after the fitting, hence removing possibly unphysical model details from the fitting process. Contributions due to individual gases, $\gamma_i(T)$ and $\delta_i(T)$, are assumed to follow eqn.(3.8) in their temperature dependence.

3.4 Absorption Line Modeling

The absorption line shape is described by:

$$A/A_0 = e^{-S(T)lP\Gamma(\omega)} \tag{3.14}$$

where l is the absorption path length (cm), P is the pressure (atm.), $\Gamma(\omega)$ is the choice of line shape model being explored (1/cm^{-1}), and A and A_0 are the measured photodiode detector signals collecting the light from the absorption and background beam paths, respectively. $S(T)$ is the temperature-dependent transition intensity (cm^{-2}*atm^{-1}). These values are calculated starting with the transition intensity values reported in the HITRAN 2012 database[82], $S_{HITRAN}(T_0=296K)$, in units of cm^{-1}/[cm^{-2}*molecule]. From this intensity a value at a given temperature can be calculated[51]:

$$S_{HITRAN}(T) = [1-e^{-\left(\frac{hc\omega_0}{k_bT}\right)}]*[1-e^{-\left(\frac{hc\omega_0}{k_bT_0}\right)}]^{-1}*\frac{q(T_0)}{q(T)}*S_{HITRAN}(T_0)*e^{\frac{hcE''}{k_b}\left(\frac{1}{T_0}-\frac{1}{T}\right)} \quad (3.15)$$

E'' is the lower state energy, obtained also from the HITRAN 2012 database. $q(T)$ is an expression for the total internal partition sum[88]:

$$q(T) = a + bT + cT^2 + dT^3 \quad (3.16a)$$

which has the following values for acetylene for the relevant temperature range: a=-8.3088; b=1.4484; c=-2.5946*10^{-3}; d=8.4612*10^{-6}. $S_{HITRAN}(T)$ can then be converted to $S(T)$:

$$S(T) = S_{HITRAN}(T)*\frac{10^{-6}N_A}{RT} \quad (3.16b)$$

N_A is Avogadro's constant, and R is the gas constant. Recently Li et al[89]independently measured acetylene line strengths and found values similar to the HITRAN reported values. Also some years ago, Varanasi and Bangaru[90] also reported intensity measurements for the P(11) transition in this band at 295 K. Their reported value at 295 K was 0.3284 cm^{-2}/atm, and the value used for this work was 0.2888 cm^{-2}/atm. The way the intensity is handled in the data analysis software is described in the next section.

In the data considered here, explicit non-linear line mixing effects[91] are not taken into account since P(11) is effectively isolated at the pressures in this study. The line separation is such that adjacent lines in this band cannot be efficiently coupled by collisional energy transfer at pressures less than ~5 atm. given the measured $\gamma_i(T)$. Briefly when analyzing Data Set II line mixing effects were considered in the models but were not found to provide a measurable improvement, and resulted in very similar results but with higher uncertainties. The additive effects of the wings of two hot band lines were however included. Linear effects due to overlapping hot band lines can affect the values and temperature dependence of fitted parameters for the line of interest if not taken into account. Hot bands tend to diminish quickly as temperature decreases which would cause larger perturbations at high temperatures but have no effect on lower temperature results. Table 3.2 shows the nearby overlapping hot band lines and their intensities relative to the line of interest. The R(9)e of $101(11)^0$+g← $000(11)^0$+u and the R(11)e of $101(20)^0$+u←$000(20)^0$+g lines were included in the modeling using Voigt parameters fixed at the HITRAN[82] values due to their size and proximity to the line center. Since they are three orders of magnitude weaker than the fundamental transition of interest this was considered sufficient to remove them as a possible contribution to systematic errors or uncertainty. In Chapter 4 the validity of this assumption is discussed and the contribution of hot bands to the line shape will be further explored.

Data analysis involves fitting experimental line shapes using calculated spectra that are the result of taking the convolution product of an instrument line shape (or apparatus function) and a theoretical model describing the line shape that is selected to best fit the experimental data. The absorption line shape and the apparatus function may both be adjusted (or fixed to a predetermined value) in a least squares fit procedure to minimize the residuals in the observed minus calculated (O-C) synthetic spectrum to determine the appropriate spectroscopic parameters.

Table 3.2: List of assigned acetylene transitions in the region being measured. Bolded transitions are those included in the analysis of Data Sets I,II, and III.

Position[a] (cm^{-1})	upper[b]		lower		Relative intensity
6528.897	$200(10)^1$g	←	$000(01)^1$u	P15f	0.001777
6528.9311	$200(10)^1$g	←	$000(01)^1$u	P15e	0.000635
6528.9311	$110(21)^1$ 2u	←	$000(10)^1$g	P25e	0.000213
6529.0846	$101(02)^2$u	←	$000(02)^2$g	R6e	0.000214
6529.0846	$101(02)^2$u	←	$000(02)^2$g	R6f	0.000641
6529.1363	**$101(11)^0$+g**	←	**$000(11)^0$+u**	**R9e**	**0.00046**
6529.171909	**$101(00)^0$+u**	←	**$000(00)^0$+g**	**P11e**	**1**
6529.1962	**$101(20)^0$+u**	←	**$000(20)^0$+g**	**R11e**	**0.001931**
6529.2344	$110(12)^1$ 2g	←	$000(01)^1$u	P28f	7.78E-06
6529.2514	$101(11)^2$g	←	$000(11)^2$u	R10f	0.000502
6529.2717	$101(11)^2$g	←	$000(11)^2$u	R10e	0.001506

[a]Positions reported in HITRAN 2012 [82] database.
[b]Transition naming conventions from Jacquemart et al. [92].

3.5 Line Shape Fitting Programs

A. Data Sets I and II

The analysis program used, written by Hurtmans[48], calculates a synthetic spectrum by convolving the laser emission profile with an appropriate absorption line model. The resulting calculated spectrum is then compared to the experimental spectrum as an Observed - Calculated (O-C) plot. A flat O-C plot with random noise fluctuations represents a perfect fit to the data. The spectra acquired at different pressures were fitted simultaneously, but separate fits were performed for each temperature, as listed in Table 2.2. The temperature dependence of the broadening and shift parameters were subsequently determined by fitting the sets of independently determined values of $\gamma_i(T)$ and $\delta_i(T)$ to eqn. 3.8 or 3.9, respectively. Voigt, SOFT, HARD, RGP, and SDV models were used for comparison. The hard and soft collision model

fitting results are very comparable, while the Voigt fits lead to relatively large systematic residuals.

For a satisfactory fit, it is crucial that the line amplitude be correct, yet there are many relatively poorly characterized contributions to it. for example, the line strength values have estimated uncertainties of 2%[93] in the HITRAN 2012 database[82]. The partial pressure of the absorbing gas is subject to the pressure gauge uncertainties, which can be relatively large at low partial pressures. Non-ideal gas behavior[94] could contribute as much as 3% to the measured amplitudes and baseline uncertainties can also be correlated with the amplitude. The line intensity is also subject to any minor path length reductions due to copper contraction as the temperature is reduced. The path length is expected to decrease by about 0.3% from room temperature down to 125 K. These uncertainties combine to create a line amplitude that is difficult to model but that will prevent fit convergence if quantities are fixed to incorrect values. Therefore the overall line amplitude for individual line measurements was allowed to vary in this analysis by incorporating a variable correction factor that is approximately equal to unity. Most sources of uncertainty will be accommodated by this, but small errors in pressure will not contribute to the line shape model portion of eqn. 3.14 as they would if the pressure was being fit instead of the amplitude. Two samples of a concatenated array of files are shown in Figure 3.1. Figure 3.2 shows a series of varying temperature lines at nearly the same pressure. The line intensities derived for the pure acetylene lines in this analysis are the HITRAN values ± 1.5% typically.

Occasionally in Data Set I one also encounters a weak fringe in the residuals. These fringes may arise from optical feedback between optical elements, including optical surfaces, spatial filters, etc. and the fringe spacing can change over time due to changes in the room temperature of the laboratory. If there is only one fringe frequency present, it can easily be eliminated from the residuals by including a fringe in the fitting algorithm. Using such fringe reduction techniques, when necessary, a fit is achieved that has residuals (observed data points minus calculated points from fitting a line shape function, O-C) smaller than 0.01% of the signal channel. For Data Set II and III more careful alignment was able to reduce the fringes to the

point where they did not need to ever be modeled in the fit, and the experimental design improvements made in Chapter 4 virtually eliminate them.

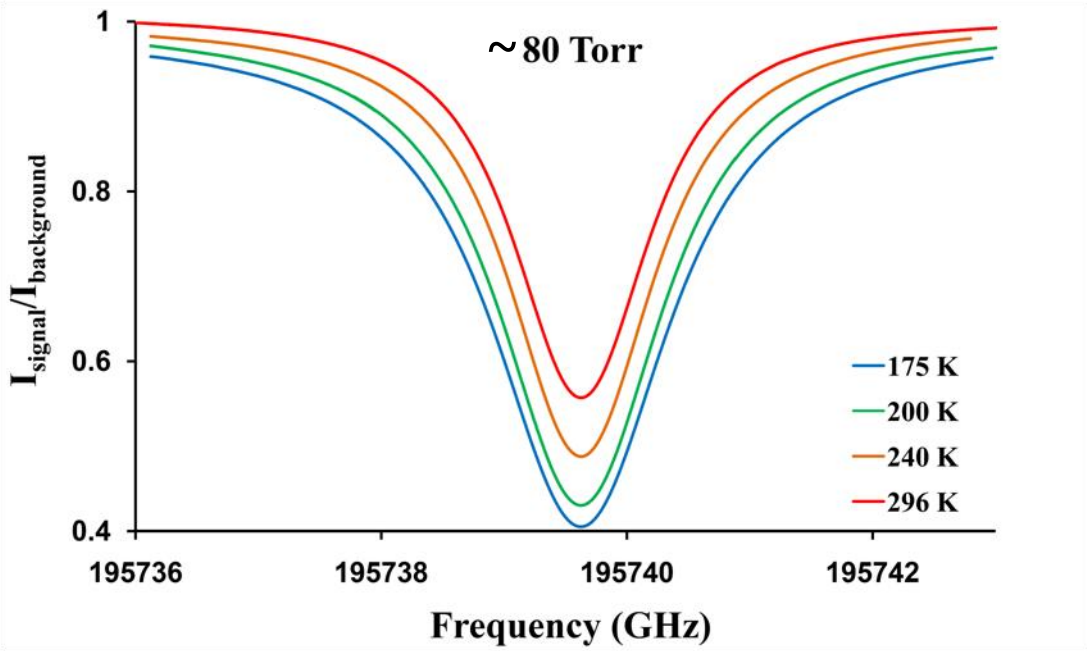

Figure 3.2: A plot of pure C_2H_2 lines from Data Set II with a nearly constant pressure of 80 Torr but varying temperatures, demonstrating the effect of temperature on a line shape.

B. Data Set III

A new data analysis program was written for the analysis of Data Set III, with the model coding done by Damien Forthomme. In Data Set II, self-collision data for each temperature were previously analyzed separately, resulting in a value for $\gamma_i(T)$, $\delta_i(T)$, and q at each measured temperature. Under these conditions, q varied but showed no well-defined trend with temperature, conceptually it should be represented by a single value. In the new multispectrum fitting code, either the SDV or Q-SDV model can be used. It allows for fitting of all the self- (or N_2-) broadened spectra simultaneously across all temperatures and pressures. With this code, only two parameters describing the broadening, $\gamma_i(T_0)$ and $n_{\gamma,i}$, were determined and the power law of eqn. 3.8 was used as a constraint on the temperature dependence, in place of having separate, uncorrelated broadening parameters for each temperature. For the SDV model, a single

q value in accord with the entire dataset was determined. In preliminary fits, the remaining parameters were allowed to float independently at each temperature– this includes $\delta_i(T)$ for SDV and $\delta_i(T)$, $\gamma_{2,i}(T)$, and $\delta_{2,i}(T)$ for Q-SDV. As clear trends were noted additional temperature-dependent constraints were added as described in Chapter 3.7.

As in the previous Data Sets, if a single pressure and temperature line profile measurement included several segments then a single value for the line strength was fit for the full line. In all cases the pure C_2H_2 data were evaluated first with the results being imported into the C_2H_2-N_2 data fitting as fixed values.

3.6 Results: Fit Quality

A. Data Set I

Figure 3.1 contains two spectra from Data Set I. The Voigt's characteristic W-shaped residuals are apparent in both the pure-acetylene and nitrogen-perturbed spectra, but are reduced in the higher pressure example. The HARD and SOFT model result in improved fits, but asymmetric residuals are apparent. Since the other two Data Sets are much more expansive refer to the discussion in the next two sections for more detailed analysis of the differences between line shape models, perturber gases, and the temperature dependence not present in this Data Set.

B. Data Set II

At intermediate pressures, between 4 Torr and 50 Torr, a weak asymmetry is observed at all sample temperatures. Figure 3.3 shows a spectrum recorded with a gas temperature of 150 K and at a pressure of 4 Torr. The spectrum in Figure 3.3 is recorded using the 1.085 cm absorption path length cell. The entire spectral line was collected in one continuous scan at this pressure. The lower panels show the residuals plotted for several line shape models fitted to the

data. Each of the lower panels is plotted with the same vertical scale to facilitate analysis by inspection. The sharp artifacts shown in each panel result from the laser locking to the comb off the side of the beat note at high absorption and can be removed from the fit weighting.

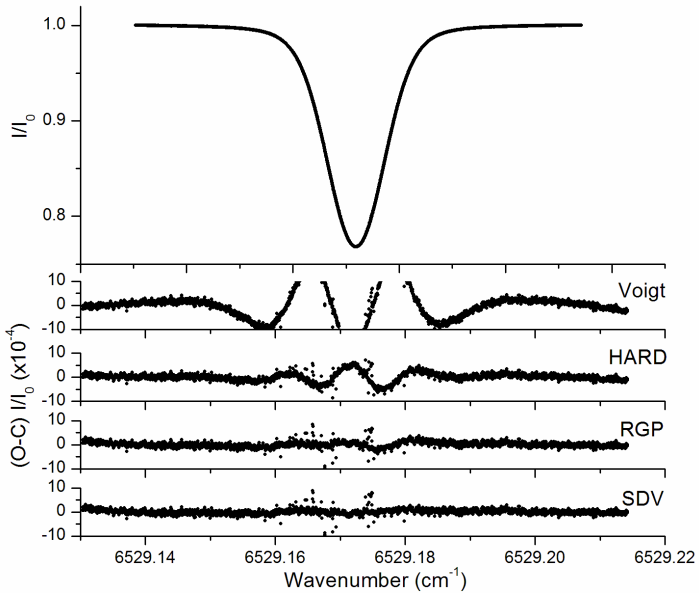

Figure 3.3: Transmission spectrum of the acetylene P(11) line at 4 Torr and 150 K and in a 1.085 cm absorption path length. (Bottom panels) Residuals (O-C) under these conditions resulting from least squares multispectrum fitting of experimental data to the corresponding line shape models.

The upper panel in Figure 3.3 shows results for a Voigt line shape model. These show the characteristic inverted W shape residuals near the line center commonly associated with this model. In this case the model is an inappropriate choice due to its oversimplified nature.

The SOFT and HARD models provide residuals that are nearly identical in quality, so only the HARD (O-C) residual results are discussed. Clearly the HARD residuals shown in Figure 3.3 are reduced significantly when compared to the Voigt fit. However, the residuals as plotted are still significantly larger than the residual spectral noise level near the line center. It appears that, near line center, collisional narrowing in the HARD model may be too large, as seen in the residuals. However, the fit in the line far wings is quite good.

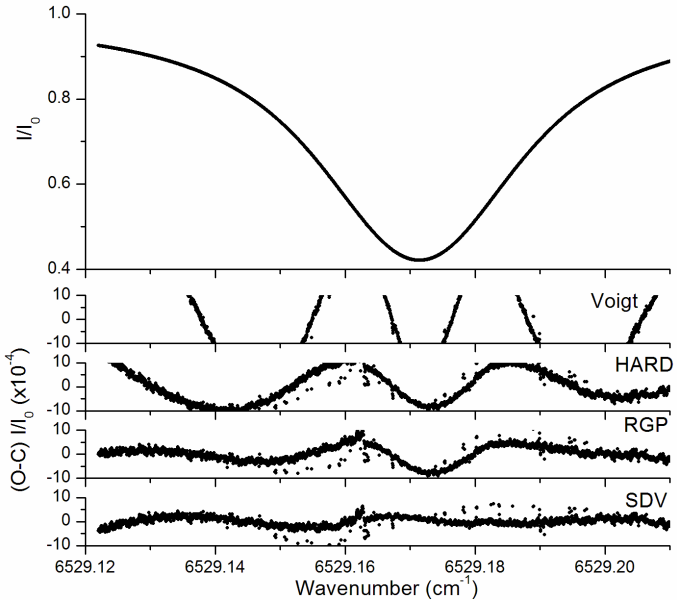

Figure 3.4: Transmission spectrum of the acetylene P(11) line at 45 Torr and 160K and a 1.085 cm cell length. (Bottom panels) Residuals (O-C) under these conditions resulting from least squares multispectrum fittings of experimental data to the corresponding line shape models.

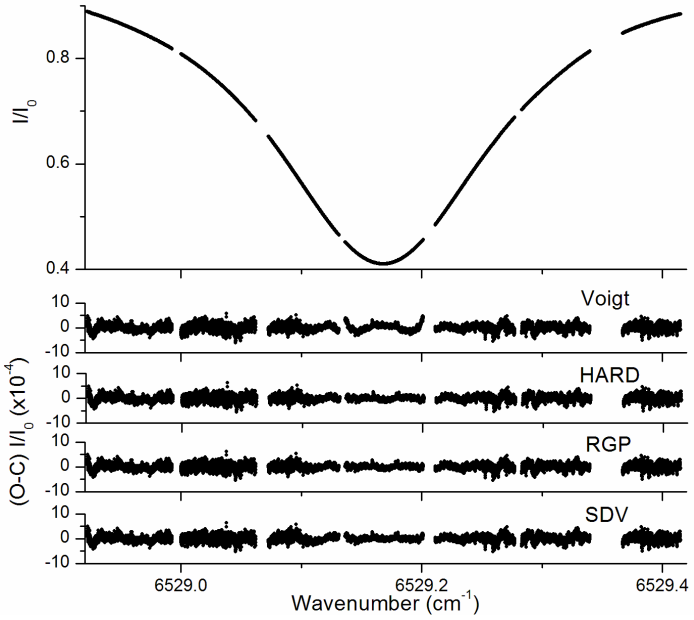

Figure 3.5: Transmission spectrum of the acetylene line studied here at 352 Torr and 200 K and a 1.085 cm cell length. (Bottom panels) Residuals (O-C) under these conditions resulting from least squares multispectrum fittings of experimental data to the corresponding line shape models.

For this study it was determined RGP and csdRG models provided similar residuals when applied to the lowest pressure and lowest temperature spectra. So only the results from the simpler model, RGP, are discussed. The RGP residuals in Figure 3.3 are significantly closer to the spectral noise level than are the HARD results. In fact the residuals almost lie at the system spectral noise level, but small asymmetries still exist near line center, and the residuals are approximately two times the size of the spectral noise. The RGP model does not properly model asymmetry, and a small narrowing residual remains.

The fit of the SDV results in the lower panel of Figure 3.3 is good to nearly the spectral noise level. Clearly, the SDV model fits the 150 K low pressure spectra best and this was found to be the case for all spectra recorded at 150 K.

Spectra recorded at higher pressures, where pressure broadening begins to strongly affect the spectral line profile, are generally not as sensitive to the different line profile functions used to reproduce the experimental spectra. Figure 3.4 shows a spectrum recorded at 160 K and 45 Torr, which is approximately 10 times higher pressure than is plotted in Figure 3.3. The entire spectral line was collected in one continuous scan at this pressure.

As before, the residuals associated with each of the four line shape models (convolved with the instrument function) are plotted in the lower panels of Figure 3.3. The Voigt profile fit is poor. The HARD residuals are a significant improvement over the Voigt case but remain unsatisfactory. Close inspection shows an asymmetry in the residual, evidence that speed-dependent effects remain. The RGP model residuals are shown below, and are an improvement over the HARD model, but still small asymmetric structure remains. Finally, in the bottom panel, the SDV residuals are within the spectral signal-to-noise ratio, representing the best fit at these experimental conditions.

A third spectrum is displayed in Figure 3.5. This is a concatenated spectrum in which seven individual experimental files are combined to create one continuous scan over the pressure

broadened line. For this spectrum the sample cell and gas were maintained at 200 K at a sample pressure of 352 Torr. The gaps in the concatenated scan result from non-overlap of successive scans in this case. In figures 3.4 and 3.5, the far wings of these strongly pressure-broadened lines are not shown because they are entirely dominated by the Lorentzian part of the lineshape function.

Analysis of this spectrum results in the panels plotted in the lower part of Figure 3.5. The Voigt line shape model fits to the experimental noise level in the wings, but in the region of the line center the residuals take on the characteristic shapes experienced in Figure 3.3 and 3.4 for this model. The Voigt line shape model is inadequate to fit the experimental spectrum to the signal-to-noise level.

All three of the more sophisticated line shape models are adequate to model the spectrum recorded under these conditions, however. The residuals in the same order as for Figure 3.4 are shown in the lower panels and fit the data to the experimental signal-to-noise levels. However, the SDV profile is the only profile that fits the data close to the noise at all temperatures and at all pressures measured, thus the SDV profile is selected as the appropriate profile to describe pure acetylene spectra recorded in this study at temperatures between 296 and 150 K, and at pressures between 3 and nearly 360 Torr pressure.

These results also emphasize another important fact that cannot be stressed enough: when trying to fit absorption line profiles, one must include low pressure spectra where artifacts may be observed in model fit residuals as well as fits to spectra at a variety of low temperatures. It is inappropriate to claim success with any line shape model unless experimental spectra have been fitted down to pressures of several Torr, in addition to including intermediate (several tens of Torr) and high pressure spectra (several hundreds of Torr). Extrapolation to lower pressures won’t work unless one is using the right model, which is impossible to determine without low pressure measurements.

C. Data Set III

As a measure of fit quality, a root mean square error (RMSE), derived from the squared differences between experimental transmission data points and calculated values, was calculated for each line measurement. The average RMSE for pure C_2H_2 line measurements was 0.011% of the maximum transmission for both SDV and Q-SDV models. RMSEs are very similar across the entire data set, with a slight trend of higher RMSEs as pressure and temperature decreases.

The baseline in each data file (representing either a full line or segment) was represented by an adjustable offset, slope, and curvature and is dominated by random independent drift of the signal in the two detection channels. Attempts were initially made to fit with only an offset and slope, which are necessary due to a drift in the ratio of the signal and reference channels and a wavelength-dependent drift caused by the changing laser diode current in the frequency stabilization locking loop, respectively. With only two baseline parameters the residuals contain small, but clearly observable features attributed to the drift in the signal ratio. Adding the third, quadratic, term to the baseline removes these features from the residuals and results in a factor of 2 improvement in RMSE. Unfortunately, each individual file measurement has a unique baseline that requires individual treatment. This implies that in the broader line shapes requiring multiple segmented scans there is little useful information in partial segments in which a line center is not present as the baseline can accommodate a large variety of different parameter values. This is something that was not realized in the analysis of Data Sets I and II and were only able to explore because of the new custom analysis code. In the SDV model fits, parameters were unchanged within their expected uncertainty when adding the quadrature parameter to the baseline (or even from a fit with only a single offset parameter) indicating that the multispectrum fit is not being biased by the additional parameters. However, the additional flexibility in the Q-SDV model caused the inclusion or exclusion of baseline curvature to change the values for the parameters of interest. Based on the improved RMSE and residual quality, it is believed that including the curvature removes most baseline inconsistencies which may negatively influence parameters that could accommodate the features such as the line

asymmetry. Improvements to the spectrometer, discussed in Chapter 4, were designed to reduce the baseline variation and remove the need to concatenate scans across a line, giving more useful data.

The data illustrated in Figure 3.6 are from a range of pressures at a constant 1.3% concentration and 175 K temperature from the C_2H_2-N_2 measurements. The observed–calculated residuals shown are representative of the line shape fits. For the two line profile models compared here, the average RMSE of all the measurements was 0.0095% of the maximum transmission for the SDV and 0.0089% for the Q-SDV. The RMSE was below 0.19% of the peak absorption in any line measurement for either model. While the N_2-broadened line shape fits have, on average, slightly smaller RMSE values than the self-broadened fits, the distribution showed some systematic trends. Lower pressure line shapes tended to have slightly poorer RMSE values, representing a less than perfect fit. Often the baseline variation of a line segment was fit imperfectly, resulting in visible features within the residuals above the spectrometer noise. Data recorded using the new spectrometer software controls described above had smaller than the average RMSE.

The lowest pressure data in Figure 3.6 show small, but systematic, deviations between the measured and calculated line profiles at line center, characteristic of inaccurate modeling of the narrowing and shifting contribution to the line shape at the nominal recorded pressure. Many of the measurements taken at pressures lower than 100 Torr showed similar discrepancies. Potential causes of these errors other than model deficiencies were explored. For example adjusting only the pressure by a few tenths of a Torr can fit an independent line with much reduced residuals. As a model of this, the error in the 33.9 Torr line profile at 175K in Figure 3.6 is consistent with a pressure error of less than 1%. This could be attributed to very small zero offsets in a pressure gauge reading or even a miscalibrated pressure gauge. In order to investigate potential issues with the pressure gauge, two additional NIST calibrated gauge with certified accuracy of 0.05% were obtained and compared to the first. The three gauges did not agree to within their calibrated uncertainties, but were within roughly 0.5% of each other. Other data (not shown) had residuals representative of similar pressure differences, but with the opposite sign, while still others were flat. An additional potential contribution to the residuals would be underlying hot band lines; this is discussed further in Chapter 4.

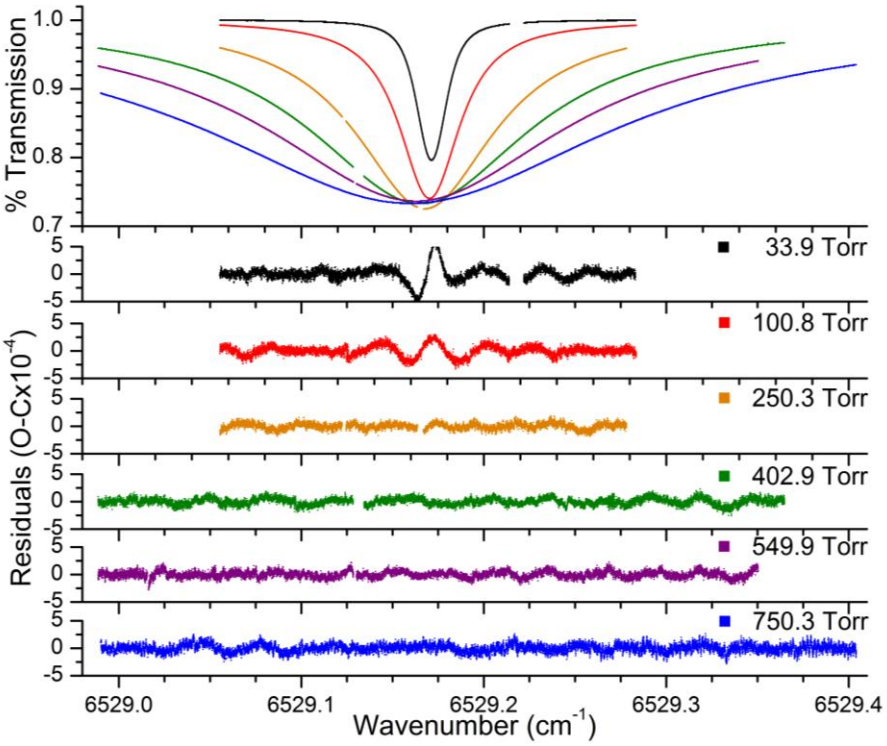

Figure 3.6: Example spectra taken at a concentration of 1.3% C_2H_2 in N_2 at 175 K. Overlaid in the top plot are the raw experimental data. The lower panels contain expanded residuals of the observed-minus-calculated data points at 6 different pressures, obtained with the SDV model. Due to instrumental constraints broader line shapes needed to be taken in several segments and were later concatenated, leaving small gaps where no data exists.

Figure 3.7 shows sample N_2-broadened data residuals resulting from both lineshape models, covering a variety of temperatures and pressures. At higher pressures the models give nearly identical fits. As pressure decreases, both models often show inexact modeling of the narrowing, as discussed above, leading to the "w" or "m"-shaped residuals at line center, primarily due to small pressure errors, combined with the constraints of the multispectral fit. Q-SDV fits exhibit slightly smaller and more symmetric residuals at all pressures, presumably a result of the model's additional flexibility.

The effects of systematic errors in pressure are not normally accounted for in line shape analyses, because errors in the frequency measurements are comparable or larger. For the present work, the frequency uncertainty in the data is negligible. Least squares fits to the data that do not include an account of the pressure (or other variable, such as temperature) uncertainty

result in derived parameters with artificially small statistical uncertainties[95]. A robust way of including uncertainties in secondary measured quantities uses a Monte Carlo technique described, for example, in Bevington and Robinson[96]. A variation of this procedure was implemented in order to derive realistic parameter uncertainties. It is assumed that the maximum pressure error in each measurement is at the level of 0.5%. For each line measurement, 500 new pressures were computed. They were chosen with a Gaussian probability function distribution about the measured pressure, with a standard deviation of 0.5% of the measurement. The overall fit was then repeated 500 times using the vector of new pressures for each line measurement, generating a distribution of the fitted parameter values. A standard deviation σ_{SDV} (or $\sigma_{Q\text{-SDV}}$) was obtained for each of the parameters by combining the results of all the dataset fits (indexed by *j*):

$$\sigma_{SDV} = \sqrt{\frac{\sum_{j=1}^{N}(X_j - \bar{X})^2}{N-1}} \tag{3.17}$$

where X_j is a parameter with average over all fits of $\bar{X}$, and N is the number of datasets, 500 here. 500 samples resulted in well-converged standard deviations. These standard deviations are reported in Tables 3.9 through 3.12 as the pressure, or "P-smeared" uncertainties. Naturally, these numbers are larger than the statistical estimates derived from the standard fitting procedure, but account for the pressure uncertainties such that the "true" parameters certainly lie within these limits.

Fitted line amplitudes for the pure C_2H_2 SDV data are higher than HITRAN's reported values[82] and a pressure-dependent trend is noted. At pressures less than 100 Torr, calculated intensities tend to be approximately 2% higher than HITRAN's values. At higher pressures intensities are no longer consistent; there is as much as an 8% difference from HITRAN, and some measurements were lower than expected. This is because the high pressure data is recorded in segments and particularly subject to baseline uncertainties. For the N_2 broadened data, the partial pressure of C_2H_2 is very small and the correction factor accommodates this pressure error. The line shape parameters are determined by the much larger N_2 pressure. These

intensity discrepancies may also be attributed to the incorrect modeling of underlying hot bands discussed in Chapter 4.

Some data were recorded at approximately 25% and 50% acetylene concentrations (160 Torr and 80 Torr total pressure, respectively) at 175 K, 200 K and 240 K. Unlike the pure C_2H_2 or low concentration data, in the high concentration data, the line shapes contain significant contributions due to collisions involving both gases, implying pressure uncertainties will have a greater effect. It was found that the multispectrum fit depended more heavily on the concentrations chosen for these line measurements than for the rest and were ultimately unable to reconcile them with the low concentration data. No literature reports could be found with speed-dependent line shapes being used to model mixtures of gases where one gas is not in low concentration and for the SDV model, the effective potential exponent, *q*, is not necessarily expected to follow a simple additive mole faction scaling with concentration. Because of the small number of measurements at high concentration it was difficult to determine if the problems encountered are a result of the line shape model used, increased pressure uncertainties, underlying lines, or the treatment of the concentration-dependent effective broadening parameters. In Chapter 4, a concentration-varying data set will be presented in order to investigate the cause of the difficulties encountered here.

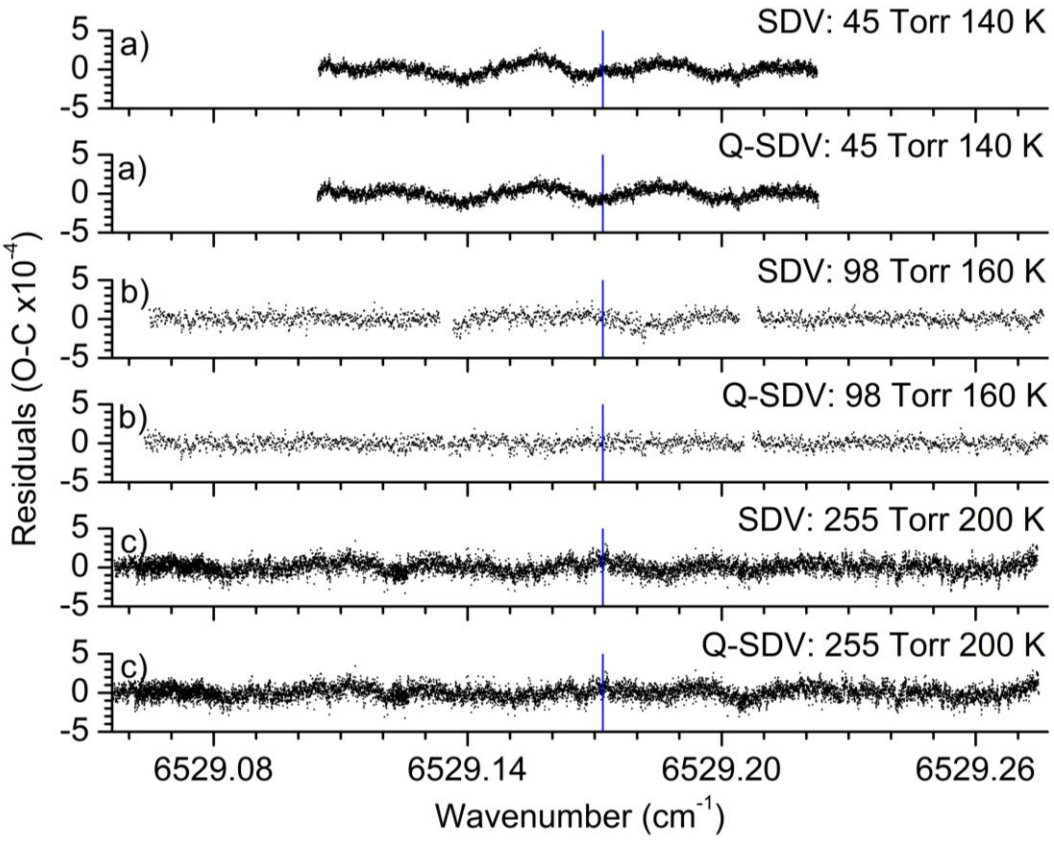

Figure 3.7. An example comparison of N_2-broadened data residuals (observed – calculated) calculated using SDV and Q-SDV models. A vertical blue line is drawn at line center for reference. a): 45 Torr and 140 K. b): 98 Torr and 160 K. c) 255 Torr and 200 K.

3.7 Results: Line Shape Parameters

A. Data Set I

The simultaneous analysis of pure acetylene spectra led to the values for the self-broadening, collisional narrowing and self-shift parameters reported in Table 3.3. There is some published data for this transition, and those results are included in Table 3.4. Table 3.3 shows the results from the present work to be at least two orders of magnitude more precise than any previous determinations of the self-broadening parameter. It should be noted that these values are from the statistical fits and were not obtained with the more rigorous uncertainty determination used for Data Set III. The shift parameter, as one would expect from the optical precision of this work, is also improved by two orders of magnitude over previous laser measurements. The self-collisional narrowing parameter is determined for the first time; no previous work on this band was able to measure this quantity. Valipour and Zimmerman[97] determined lineshape parameters for various lines in the $\nu_1 + 3\nu_3$ band and found β_{self} = 0.0426(18) for P(11) of this band; a value close to what is found for $\nu_1 + \nu_3$ here. A self-narrowing parameter of 0.02 cm^{-1}/atm was previously measured for the $\nu_1 + \nu_5$ band[98] from Q-branch measurements near 4100 cm^{-1}, but no error estimate was given.

The experimental results obtained for nitrogen and acetylene mixtures for this band are summarized in Table 3.4 where they are listed together with previously published room temperature results. The present results for the broadening parameter are more precise by two orders of magnitude according to the statistical determinations and they are larger than the previously published results due to the fact that Voigt profiles were assumed previously. The shift parameter is larger and far more precise than the recent laser results by Arteaga, et al.[11]. The nitrogen collisional narrowing result is more precise than the acetylene self-collisional narrowing result reported here, probably because the nitrogen results were obtained with nitrogen pressures of up to one atmosphere, while the pure gas results were derived from spectra with a maximum of 340 Torr of acetylene. Recent measurements by Dhyne et al[99, 100] of the

$\nu_4 + \nu_5$ band found a nitrogen narrowing parameter (β_{N2} = 0.0338(22) in cm^{-1} atm^{-1} units for R(9)) for the Rautian (hard) collision model while Valipour and Zimmerman quote a friction coefficient of 0.0252(18) for $\nu_1 + 3\nu_3$, also in close agreement with the hard collision parameter determined for $\nu_1 + \nu_3$ here.

Table 3.3: Collisional parameters for acetylene $\nu_1 + \nu_3$, P(11) at 296K (cm^{-1}/atm).

	Broadening (γ_{C2H2})	Narrowing ($\gamma_{Dicke,self}$)	Shift (δ_{self})
Hard Collision[a]	0.146317(27)	0.047271(104)	-0.0070819(22)
Soft Collision[a]	0.148310(28)	0.063905(126)	-0.0070851(21)
Voigt[a]	0.131466(37)		-0.0070363(64)
VB[90]	0.12(2)[b]		
Minutolo et al.[101]	0.124(1)[c]		-0.007(1)[c]
SG[102]	0.145(4)[d]		-0.0068(3)[d]
Li et al[59]	0.1512(23)[e]		

[a.] This work, for P(11) assuming the different lineshape models. For the various models, the resultant standard deviation of the fit (10^4 χ^2) = 1.31for the hard collision model, 1.30 for the soft collision model and 3.95 for the Voigt.
[b.] Measured from published figure.
[c.] For the P(22) line.
[d.] For the P(13) line, converted from MHz/torr, and converted to HWHM.
[e.] For P(11) and a hard collision model. These authors find γ_{self} = 0.1488(25) assuming a Voigt lineshape.

B. Data Set I Conclusions

This Data Set represents one of the first studies done with a frequency comb and is still a unique application of this technology. Frequency comb-referenced measurements of pressure parameters for molecular absorption lines result in at least two orders of magnitude improvement over the results obtained using free-running or cavity-stabilized laser systems. The statistical uncertainty determination is an underestimate and the Data Set III analysis addresses this. These measurements represent a significant improvement in the accuracy and precision of line shape spectroscopy. The ability to test models describing collisional processes is also significantly improved due to the orders of magnitude of improved precision in the retrieved pressure shift

and pressure broadening parameters. These measurements are a good start and the later frequency comb-referenced measurements build off what was learned here by expanding to more complex models and more robust modeling software.

Table 3.4: Collisional parameters for acetylene $\nu_1 + \nu_3$, P(11) perturbed by nitrogen at 296K (cm^{-1}/atm).

	Broadening (γ_{N2})	Narrowing ($\gamma_{Dicke,N2}$)	Shift (δ_{N2})
Hard Collision[a]	0.081129(35)	0.022939(74)	-0.0088913(25)
Soft Collision[a]	0.083217(37)	0.034611(99)	-0.0088973(25)
Voigt[a]	0.068979(33)		-0.0088663(48)
Arteaga et al.[11]	0.0805(8)		-0.0085(1)
Minutolo et al.[101]	0.065(1)[b]		-0.0082(2)[b]

[a.] This work, assuming different lineshape models. For the various models, the resultant standard deviation of the fit ($10^4 \chi^2$) = 1.22 for the hard collision model, 1.22 for the soft collision model and 2.31 for the Voigt.
[b.] For the P(22) line.

C. Data Set II

Considering long term temperature and pressure stability of the sample, accuracy of the wavenumber scale and experimental signal to noise ratio, the line shape data taken with this spectrometer are the most accurate that have been recorded to date for acetylene (and probably any molecule) at near-infrared wavelengths. For this reason results are reported for the analysis using the four line shape models considered above, Voigt, HARD, RGP, and SDV, even though the SDV model is clearly the only model that fits all the data to near the spectral noise level.

Table 3.5 summarizes the pressure parameters derived from fitting the experimental data to the Voigt line shape model. The Voigt model includes two pressure dependent parameters, the self- broadening parameter, $\gamma_{C2H2}(T)$, and the pressure shift parameter $\delta_{C2H2}(T)$ Uncertainties in the fit parameters are expressed in parentheses in units of the last significant figure reported for the parameter, and they are one sigma standard deviation of the least squares fits to the experimental data. Compared to the other models, the errors tend to be larger for the Voigt model. The Voigt doesn't fit to the noise level at any pressure, but at lower pressures it does especially poorly. At the severely vapor pressure-limited temperatures of approximately 165 K

and below there is no data taken at high or intermediate pressures and this is a major contribution to the trend of larger uncertainties as temperature decreases. The quoted statistical uncertainties are certainly severe underestimates of the true parameter uncertainties. With reference to Table 3.5, the pressure broadening parameter shows an increase with lowering temperature until about 165 K. The same may be said of the shift parameter. However the estimates of both parameters are influenced by the line shape asymmetry resulting from speed-dependent effects, apparent at temperatures below approximately 180 K, and asymmetry is not included in the Voigt model. Figures 3.3-3.5 all show the Voigt profile to be inadequate to represent the experimental data, with characteristic inverted W-shaped residuals at all pressures and temperatures.

Table 3.5: Line shape parameters derived from fitting the experimental data to the Voigt line shape model.

Average T (K)[a]	Broadening $\gamma_{C2H2}(T)$[a], (cm^{-1}/atm)	Shift $\delta_{C2H2}(T)$[a], (cm^{-1}/atm)
295.715(19)	0.141755(23)	-0.0076196(132)
240.135(25)	0.144846(71)	-0.0071958(101)
200.298(49)	0.181793(42)	-0.0079120(95)
175.319(16)	0.205407(23)	-0.0077875(281)
165.373(12)	0.214860(46)	-0.0080531(170)
160.343(5)	0.218815(55)	-0.0079847(308)
155.373(3)	0.210408(111)	-0.0074111(349)
150.383(20)	0.207093(144)	-0.0066676(1152)

[a] Errors in parenthesis are one standard deviation in reference to the last digit shown.

Table 3.6 summarizes the pressure parameters obtained from the analysis of the experimental data using the HARD model. The HARD model adds a confinement narrowing, β to the broadening and shift parameters for a total of three adjustable parameters. The HARD model does not include speed-dependent effects, and as a result, still predicts a symmetric line profile. Referring again to Figures 3.3 and 3.4 one can see that the residuals resulting from fitting the experimental data at lower pressures to the HARD model have significant systematic residuals near line center, and the residuals are slightly asymmetric. The highest pressure data, such as that shown in Figure 3.5 shows no sign of asymmetry, and is adequately represented by

the model. However, since the line shape model must fit all the data at all pressures and at all temperatures, the HARD (and SOFT) model are rejected since its fit is inadequate at lower temperatures and at the lowest pressures.

Table 3.6: Line shape parameters derived from fitting the experimental data to the HARD model.

Average T (K)[a]	Broadening $\gamma_{C2H2}(T)$[a] (cm^{-1}/atm)	Narrowing $\gamma_{Dicke,C2H2}(T)$[a] (cm^{-1}/atm)	Shift $\delta_{C2H2}(T)$[a] (cm^{-1}/atm)
295.715(19)	0.148057(9)	0.049393(66)	-0.0070613(29)
240.135(25)	0.169874(15)	0.053979(59)	-0.0074234(17)
200.298(49)	0.193347(6)	0.059095(61)	-0.0077966(23)
175.319(16)	0.211161(6)	0.060210(65)	-0.0076641(20)
165.373(12)	0.215287(28)	0.054967(85)	-0.0078360(22)
160.343(5)	0.229150(16)	0.079075(145)	-0.0080484(84)
155.373(3)	0.230106(53)	0.066152(170)	-0.0075890(90)
150.383(20)	0.233411(49)	0.061778(107)	-0.0077810(86)

[a] Errors in parenthesis are one standard deviation in reference to the last digit shown.

Table 3.7 includes the results from the RGP model. This model reproduces the experimental data rather well, except at the lowest temperatures and intermediate pressures. Even under the conditions of lowest temperature and pressure, the deviation from noise level is very small, perhaps a factor of two larger than the spectral noise with a clear asymmetry present. At higher pressure and temperature the fits cannot be distinguished from each of the other line shape models, excluding the Voigt.

Table 3.8 summarizes the results obtained by incorporating the SDV profile to describe the experimental spectra. The SDV model incorporates a pressure broadening, γ_L, pressure shift, δ_L, and the exponent of the leading term of the power series expansion of the intermolecular potential, q. The SDV model yielded a value for q ranging between 6.2 and 7.5 depending upon the temperature of the colliding gas molecules.

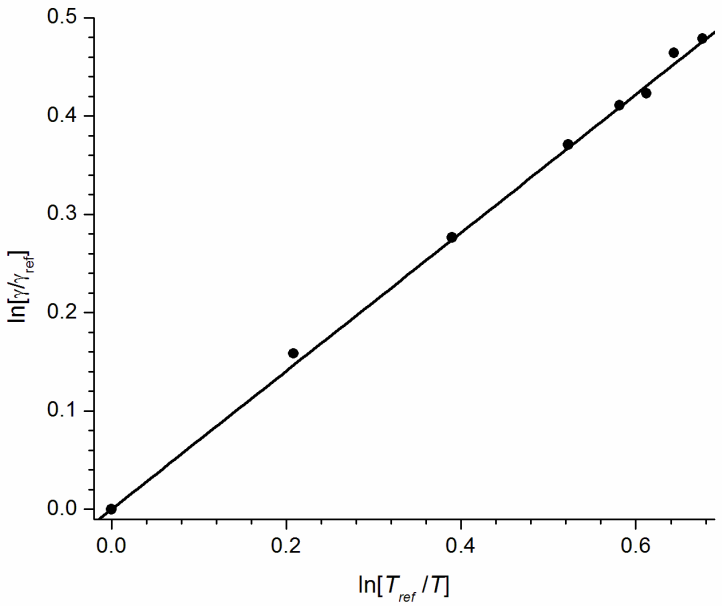

Figure 3.8: A plot of the experimentally determined temperature broadening parameters γ(T) from table 3.8 (SDV model) versus the sample temperature. The slope of this plot determines the temperature dependence exponent *n* from eqn. 3.18. Experimental error bars for both axes are smaller than the plotted points.

Since the SDV model is the only model that describes the experimental data close to the noise level, a further discussion of the temperature dependence of the pressure broadening or the pressure shift parameters derived from the other models considered above is not considered.

As mentioned in Chapter 3.3, the power law from eqn. 3.8 is used to fit $\gamma_{C2H2}(T)$. Rearranging, straight line plots can be generated with $n_{\gamma,C2H2}$ as the slope:

$$\ln\left(\frac{\gamma_i(T)}{\gamma_i(T_0)}\right) = n_{\gamma,i}\ln\left(\frac{T_0}{T}\right) \tag{3.18}$$

Figure 3.8 is a plot of the natural logarithms of these two ratios for the SDV model results. Statistical errors for both temperature and pressure in this plot are smaller than the points on the graph. The value for $n_{\gamma,C2H2}$, with its error, derived from this plot:

$$n_{\gamma,C2H2} = 0.7035(61) \tag{3.19}$$

The error obtained from one standard deviation in the plot in Figure 3.8 was 0.0050% (3.5×10^{-3}). However, this does not take into account the temperature uncertainty so the total error is approximated by also finding the standard deviation in the related plot for eqn. 3.18 with a slope of $1/ n_{\gamma,C2H2}$ (0.0071%) and taking the square root of the sum of the squares of these two standard deviations to get the error shown in eqn. 3.19. The error is expressed in units of the last digit shown for $n_{\gamma,C2H2}$. The power law dependence shown here is the result of fitting all of the data between 150 and 296 K (shown in Table 3.8). There is some scatter in the data below 200 K due primarily to the fact that the vapor pressure of acetylene limits the maximum value of the pressure employed experimentally.

Table 3.7: Line shape parameters derived from fitting the experimental data to the RGP model.

Average T (K)[a]	$\gamma_{C2H2}(T)$[a] (cm^{-1}/atm.)	$\gamma_{Dicke,C2H2}(T)$[a] (cm^{-1}/atm.)	$\delta_{C2H2}(T)$[a] (cm^{-1}/atm.)
295.715(19)	0.148220(8)	0.060433(62)	-0.0070609(24)
240.135(25)	0.168476(23)	0.059829(63)	-0.0074118(18)
200.298(49)	0.193044(11)	0.071415(64)	-0.0078071(21)
175.319(16)	0.208240(27)	0.071018(61)	-0.0074891(27)
165.373(12)	0.217076(30)	0.068137(108)	-0.0078455(24)
160.343(5)	0.226086(8)	0.080251(85)	-0.0079439(46)
155.373(3)	0.233315(51)	0.086224(188)	-0.0076071(81)
150.383(20)	0.238243(38)	0.087404(99)	-0.0077763(60)

[a] Errors in parenthesis are one standard deviation in reference to the last digit shown.

The temperature dependence of the pressure shift parameter is described here by the relation given in eqn. 3.9. Figure 3.9 shows the result of plotting a slightly modified form of eqn. 3.9, where the temperature dependence parameter δ' is the slope of a linear relation:

$$\left[\delta_i(T) - \delta_i(T_0)\right] = \delta' \times (T - T_0) \tag{3.20}$$

The experimental data are shown along with their one sigma error bars, and the linear least squares fit to the data is plotted as a straight line. The slope of this plot provides a value for the temperature dependence of the pressure shift parameter. As noted in Data Set III's analysis, this temperature dependence parameter is small compared to that found for the N_2-broadened data, which causes the points to appear far off the line. The best least squares fit value for the pressure shift parameter is:

$$\delta' = 0.00000400(50)\ \text{cm}^{-1}/(\text{atm. K}) \qquad (3.21)$$

The error in eqn. 3.21 above is expressed in units of the last digit shown for δ' and is obtained using the same method as was used in 3.19.

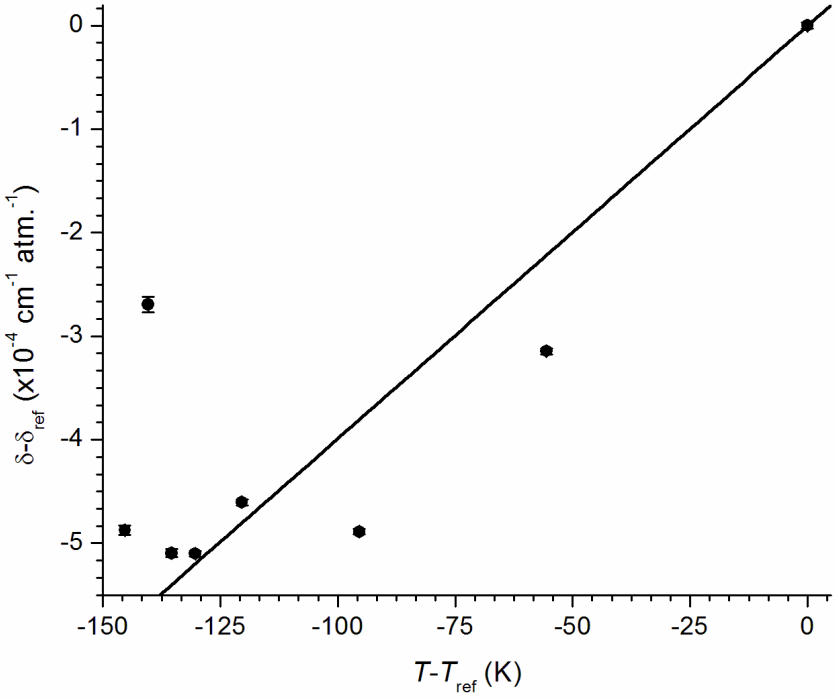

Figure 3.9: A plot of the difference between the experimental value of δ at temperature T and the $\delta_{C2H2}(T)$ at 295.7 K (T_{ref}) to determine the temperature dependence of the pressure shift parameter in the SDV model (Table 3.8). The temperature dependence is designated by the parameter δ' from (eqn. 3.20). Error bars for the vertical axis are one standard deviation as listed in table 3.8; the error bars are in some cases smaller than the plotted points.

D. Data Set II Conclusions

This is the first detailed study of acetylene in the 1.5 micron region in which line shape models were applied to spectra collected at temperatures ranging from 150 K to room temperature. The results show that the speed-dependent Voigt profile is the most suitable profile of those tested for describing the absorption line shape for this band of pure acetylene at temperatures between 296 and 150 K. The most commonly used line shape models (i.e. Voigt, Rautian, and Galatry) do not include speed-dependent terms and do very poorly modeling the observed line asymmetries at lower pressures and especially at low temperatures. Using the speed-dependent Voigt data that was also derived, for the first time, the power law temperature dependence for the pressure broadening parameter and the temperature dependence for the pressure shift parameter. The precision of these results is due to the extremely accurate frequency scale associated with the optical frequency comb laser employed in this research. There is still room for improvement in incorporating a true multispectrum fit across all temperatures simultaneously and this is addressed in Data Set III along with the better estimates for parameter uncertainties.

Table 3.8: Line shape parameters derived from fitting the experimental data to the SDV model.

Average T (K)[a]	Broadening $\gamma_i(T)$[a], (cm^{-1}/atm.)	Shift $\delta_i(T)$, (cm^{-1}/atm.)[a]	q[a]
295.715(19)	0.149912(8)	-0.0076763(21)	6.67(1)
240.135(25)	0.175658(40)	-0.0079908(20)	7.42(1)
200.298(49)	0.197660(16)	-0.0081652(15)	6.71(0.6)
175.319(16)	0.217219(14)	-0.0081368(24)	6.840(7)
165.373(12)	0.226071(8)	-0.0081864(14)	6.72(0.5)
160.343(5)	0.228853(10)	-0.0081859(31)	6.24(0.5)
155.373(3)	0.238473(61)	-0.0079458(73)	7.61(3)
150.383(20)	0.241989(28)	-0.0081638(40)	7.27(0.9)

[a] Errors in parenthesis are one standard deviation in reference to the last digit shown.

E. Data Set III

Table 3.9 contains the parameters determined from the fits to the self-collision data, with statistical errors of one standard deviation in parenthesis. The overall quality of the fit to the observations is similar to Data Set II and by extending the multispectrum fitting by using only two broadening parameters for all temperatures in the range, and including only a single q (effective potential) parameter, the results are more useful. Comparison with the results of Data Set II, also given in Table 3.9, shows that the parameters have changed by amounts that are many times greater than the respective statistical errors. This is due to the difference between the models but also large parameter correlations, particularly between quadratic baseline function coefficients and the line profile parameters. As discussed above, the multispectrum fit used here produces statistical errors that ignore pressure measurement errors and these statistical parameter errors are unrealistically small.

Table 3.9: Self-broadened line shape parameters for the P(11) line of $\nu_1+\nu_3$ derived from data in reference [1].

	----------SDV----------		----------Q-SDV----------		
Fitted Parameter	Value (uncertainty)	P-smeared uncertainty	Value (uncertainty)	P-smeared uncertainty	Data Set II
$\gamma_{C2H2}(T_0)$[a]	0.152531(8)	0.0006	0.154788(16)	0.0011	0.149912(8)
$n_{\gamma,C2H2}$	0.68763(8)	0.007	0.68541(19)	0.01	0.7035(61)
$\delta_{C2H2}(T_0)$[a]	-0.007885(1)	0.00002	-0.008166(4)	0.00005	-0.007676(2)
$n_{\delta,C2H2}$	0.07094(39)	0.005	0.05309(90)	0.01	0.086(10)
q_{C2H2}	7.353(3)	0.09	---	---	6.240(5)-7.61(3)[b]
$\gamma_{2,C2H2}(T_0)$[a]	---	---	0.02141(1)	0.0006	---
$n_{\gamma2,\ C2H2}$	---	---	0.657(1)	0.04	---
$\delta_{2,C2H2}(T)$[a]	---	---	See Table 3.11	See Table 3.11	---

[a]Units are cm^{-1}/atm. Reference temperature T_0 is 296 K. Values are reported with one standard deviation in parenthesis. Columns 3 and 5: Uncertainties obtained by assuming a 0.5% pressure uncertainty, and Monte Carlo sampling, see text for details.
[b]q parameters in [1] followed no trend but did change with temperature.

$\gamma_{C2H2}(T_0)$ and $n_{\gamma,C2H2}$ for self- collisions are compared to the previous SDV determinations in Figure 3.10(a). $\gamma_{C2H2}(T_0)$ falls outside the uncertainty of the previous value as a result of the constraints added to the fitting procedure, but the current analysis is more useful in terms of predicting profiles at different temperatures within the current range and results in a better representation of the measurements. The differences in the lower panel Figure 3.10(b) reflect the different models used in several of the earlier works. Figure 3.11(a) shows the individual $\delta_{C2H2}(T_0)$for each temperature and a comparison to the previous results. The temperature dependence is very weak for the self collision data, but based on the observed trend in the more strongly temperature-dependent N_2 $\delta_{N2}(T_0)$discussed below, the final results for C_2H_2 data have been constrained to follow eqn. 3.8. The final fit determinations, $n_{\delta,C2H2}$ and $\delta_{C2H2}(T_0)$, are reported in Table 3.9.

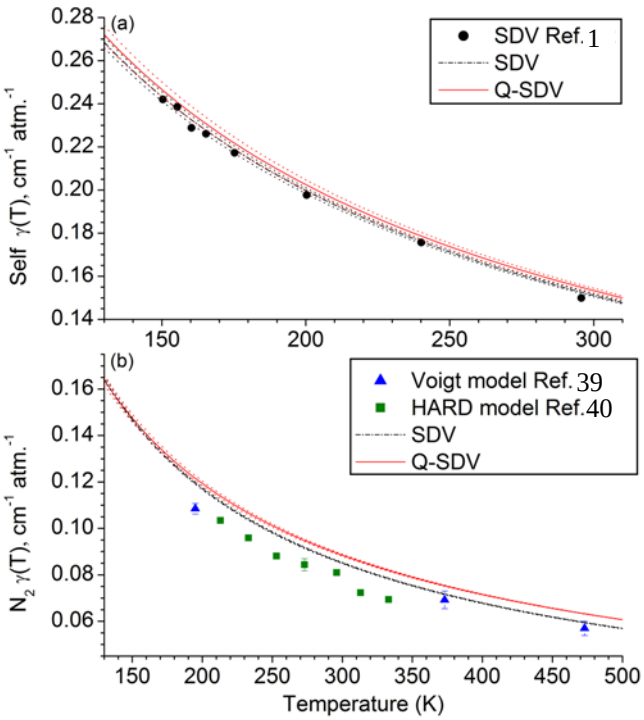

Figure 3.10: Temperature-dependent broadening $\gamma(T)$ for (a) self- and (b)N_2-broadened measurements with comparisons to previous studies. Line shape models used are as noted and plotted lines are calculated from Tables 3.9 and 3.10. Dotted lines show uncertainties as one standard deviation derived from the assumption of a 0.5% pressure measurement uncertainty, see text for details. Statistical error bars are shown as one standard deviation and are in many cases smaller than the points.

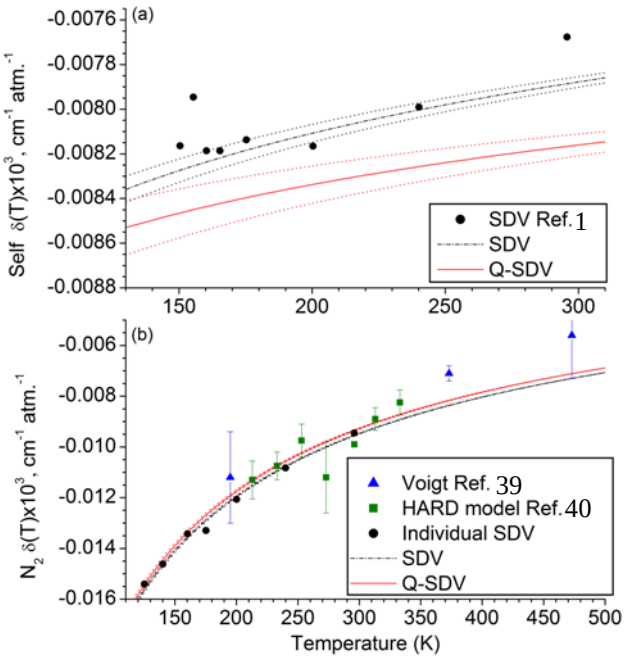

Figure 3.11: Temperature-dependent shift $\delta(T)$ for (a) self- and (b)N_2-broadened measurements with comparisons to previous studies. Line shape models used are as noted and plotted lines are calculated from Tables 3.9 and 3.10 with dotted lines indicating one standard deviation of the variation derived from the assumption of a 0.5% pressure uncertainty, see text for details. The points "Individual SDV" shown in (b) are from preliminary fits of the current data and were used to establish that $\delta(T)$ follows a power law for temperature dependence in the range of the present data. Statistical error bars are shown as one standard deviation and in many cases smaller than the points.

Table 3.10 summarizes the same results for the N_2-broadening and compares them to other analyses. In some cases, published values have been re-computed in a manner consistent with the present statistical determinations either because the authors did not report a value or adopted different analysis methods. Details are given in the table notes. The acetylene-N_2 parameters determined have similar accuracy to those found for self-collisions. Both n_γ and n_δ are larger than the respective self-collision parameters, indicating larger temperature effects on the broadening and shift for pressure broadening due to collisions with nitrogen. In the case of the shift, the strong temperature dependence seen in the points in Figure 3.11(b) allowed a clear trend to be observed that could be successfully modeled by eqn. 3.8. This allowed fits to temperature dependence in the multispectrum fit rather than determining a parameter at each temperature for the final determination.

Table 3.10: N_2-broadened line shape parameters for the P(11) line of $\nu_1+\nu_3$.

	----------SDV----------		----------Q-SDV----------			
Fitted Parameter	Value (uncertainty)	P-smeared uncertainty	Value (uncertainty)	P-smeared. uncertainty	Reference [39][b]	Reference [40][c]
$\gamma_{N2}(T_0)$[a]	0.086022(13)	0.0003	0.089351(19)	0.0005	---	0.08095(95)
$n_{\gamma,N2}$	0.78678(18)	0.005	0.73771(35)	0.009	0.75(3)	0.75(8)[d]
$\delta_{N2}(T_0)$[a]	-0.009548(2)	0.00002	-0.009346(4)	0.00003	-0.00837(12)[d]	-0.0099(1)
$n_{\delta,N2}$	0.57323(38)	0.004	0.58295(80)	0.006	0.717(57)[d]	0.57(20)[d]
q_{N2}	6.814(7)	0.03	---	---	---	---
$\gamma_{2,N2}(T_0)$[a]	---	---	0.01383(2)	0.0003	---	---
$n_{\gamma 2,N2}$	---	---	0.458(2)	0.04	---	---
$\delta_{2,N2}(T)$[a]	---	---	See Table 4	See Table 4	---	---

[a]Units are cm^{-1}/atm. Reference temperature T_0 is 296 K. Values are reported with one standard deviation in parenthesis. Columns 3 and 5: Uncertainties obtained by assuming a 0.5% pressure uncertainty, and Monte Carlo sampling, see text for details. $\delta_2(T)$ parameters can be found in Table 3.12 for the Q-SDV model.
[b]Voigt model results.
[c]Hard model results. P(11) estimate based on averaged results from P(10) and P(12) measurements.
[d]Calculated using eqn. 3.8 and weighted least squares fit to reported $\gamma_{N2}(T)$ and $\delta_{N2}(T)$ values, for comparison.

Data from other temperature dependent C_2H_2-N_2 studies in this band[39, 40] are included in Figures 3.10(b) and 3.11(b). Campbell et al.[39] reported one measurement within the present data's temperature range, at 195 K, and two higher temperature measurements at 373 K and 473 K. Rozario et al.[40] reported measurements at seven temperatures ranging from 213 K to 333 K. In reference [39], the data were fit to a Voigt profile and the pressure broadening parameters so derived are systematically lower than the plotted line representing $\gamma_{N2}(T_{ref})$ and $n_{\gamma,N2}$ from the current study. This is probably a result of the neglect of any narrowing in the Voigt profile, rather than any measurement inconsistency. Campbell et al. also determined a temperature exponent, $n_{\gamma,N2}$ which matches the present value to within quoted uncertainties. Of the data presented in Rozario et al. [40] the hard collision model data was chosen for comparison. The temperature-dependent parameter $n_{\gamma,N2}$ is once again in good agreement with the value from the present study, with individual $\gamma_{N2}(T)$ values again systematically lower than the present values. In reference[40] fixed narrowing parameters were used and these may have been estimated too high (in the case of C_2H_2-C_2H_2) or too low (C_2H_2-N_2), giving rise to the observed differences.

Figure 3.11(b) plots the data relating to the N_2 pressure shift. Data points from [39] and [40] show good agreement to the present results within their experimental uncertainty. The $\gamma_{N2}(T_{ref})$ points in[39] are lower than determined here, which can likely be explained by fitting line profiles that include some narrowing contribution with a Voigt profile. Based on the similarities between the data sets, it is believed eqn. 3.8 can be used successfully to extend both the present broadening and shift parameters to the higher temperatures where data was measured in reference [39].

Table 3.11: Narrowing and shift parameters derived from Q-SDV fits to the self broadened data.

Average T (K)	$\gamma_{2,C2H2}(T)$ Q-SDV	D_m Calculated	$\delta_{2,C2H2}(T)$ Q-SDV	$\delta_{2,C2H2}(T)$ P-smeared uncertainty
295.715(19)	0.02169(1)	0.040	-0.001689(6)	0.00006
240.135(25)	0.02495(1)	0.048	-0.001437(5)	0.00005
200.298(49)	0.02802(1)	0.057	-0.001344(5)	0.00006
175.319(16)	0.03055(1)	0.066	-0.001389(5)	0.00003
165.373(12)	0.03107(1)	0.070	-0.001479(5)	0.00005
160.343(5)	0.03195(1)	0.072	-0.001540(6)	0.00004
155.373(3)	0.03240(1)	0.074	-0.001563(7)	0.00004
150.383(20)	0.03333(1)	0.077	-0.001663(8)	0.00002

Column 2: speed-dependence of broadening obtained from a Q-SDV model fit where only $\gamma_i(T)$ is constrained to the power law in eqn. (1). Column 3: Calculated mass diffusion constant D_m values (see Page 25). Column 4: Self-broadened asymmetry due to the speed dependence of shift, $\delta_{2,C2H2}(T)$, obtained from the final Q-SDV model results in which the temperature dependence of $\gamma_i(T)$, $\delta_i(T)$, and $\gamma_{2,i}(T)$ are constrained to follow eqn. 3.8. Values have one standard deviation in parenthesis and units are cm^{-1}/atm. Column 5: Uncertainties obtained by assuming a 0.5% pressure uncertainty and Monte Carlo sampling, see text for details.

Tables 3.9-3.12 and Figures 3.10-3.13 contain results obtained with the Q-SDV model. Broadening and shift parameters are very similar to those determined using the SDV model, as one would expect. An advantage of using the Q-SDV is that one can determine how the narrowing and asymmetry change with temperature, while in the SDV model with a global q, the temperature dependence is part of the assumed physical model. Figure 3.12 shows narrowing parameter data points, labeled "Individual Q-SDV", obtained from self- and N_2- broadened fits where only the broadening $\gamma(T)$ temperature dependence was fixed to the power law, eqn. 3.8. In

both cases, but for self-collisions especially, the points display a power law dependence. The temperature dependence of the speed-dependent narrowing is more difficult to measure no reports of it could be found in the literature. For models based on Dicke-type narrowing a temperature dependence was recently reported for C_2H_2[42, 103] and Ar-perturbed H_2O[104]. In these 3 cases the authors also found a power law temperature dependence. If Dicke narrowing is related to the gas diffusion coefficient[62, 63] a $T^{-1/2}$ temperature dependence can be predicted, so the present results are not unexpected.

Table 3.12: Narrowing and shift parameters derived from Q-SDV fits to the N_2-broadened data.

Average T (K)	$\gamma_{2,N2}(T)$ Q-SDV	D_m Calculated	$\delta_{2,N2}(T)$ Q-SDV	$\delta_{2,N2}(T)$ P-smeared uncertainty
295.851(19)	0.01355(2)	0.031	-0.000600(7)	0.00005
240.080(20)	0.01482(1)	0.037	-0.000412(6)	0.00004
200.145(71)	0.01630(1)	0.044	-0.000626(6)	0.00005
175.281(96)	0.01709(1)	0.050	-0.000737(9)	0.00007
160.128(33)	0.01910(5)	0.054	-0.001382(24)	0.00007
140.117(44)	0.02069(2)	0.061	-0.001262(13)	0.00007
125.300(2)	0.02218(3)	0.069	-0.002307(17)	0.00007

Column 2: speed-dependence of broadening obtained from a Q-SDV model fit where only $\gamma_i(T)$ is constrained to the power law in eqn. 3.8. Column 3: Calculated mass diffusion constant D_m values (see Page 25). Column 4: N_2-broadened asymmetry due to the speed dependence of shift, $\delta_{2N2}(T)$, obtained from the final Q-SDV model results in which $\gamma_i(T)$, $\delta_i(T)$, and $\gamma_{2,i}(T)$ are constrained to eqn. 3.8 for temperature dependence. Values have one standard deviation in parenthesis and units are cm^{-1}/atm. Column 5: Uncertainties obtained by assuming a 0.5% pressure uncertainty and Monte Carlo sampling, see text for details.

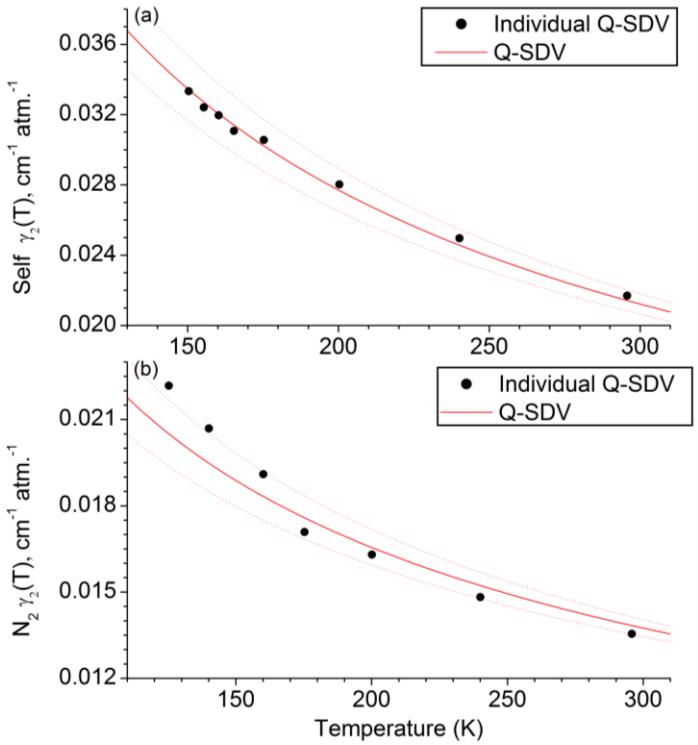

Figure 3.12: Temperature-dependent narrowing $\gamma_{2,i}(T)$ for (a) self- and (b)N_2-broadened measurements and the Q-SDV model. Points "Individual Q-SDV" are from Tables 3.11and 3.12 and were used to determine that $\gamma_{2,i}(T)$ follows a power law in temperature dependence. The plotted lines were produced from the final fitted values for $\gamma_{2,i}(T_0)$ and $n_{\gamma 2,i}$ from Tables 3.9 and 3.10, and dotted lines show errors obtained by assuming a 0.5% pressure uncertainty, see text for details. Statistical errors of one standard deviation are smaller than the points.

A Taylor Series approximation to the speed-dependent Galatry profile[87] suggests that the value of Dicke narrowing, γ_{Dicke}, would need to be approximately 3 times that of γ_2 to give an equivalent narrowing contribution and this has been confirmed in work on CN radical[85]. Assuming this relationship, three times the value of γ_{2self} (0.022 cm^{-1}.atm^{-1}) determined here, exactly corresponds to the γ_{Dicke} determined by Povey et al.[103] of 0.066(2) cm^{-1}.atm^{-1}at 293 K for another acetylene combination band in this region.

γ_{Dicke} may also be estimated from the mass diffusion constant D_m according to eqn. 3.5. Shown in Tables 3.11 and 3.12, calculated D_m values are between 1.8 and 2.3 times the size of $\gamma_{2,C2H2}(T)$ for self-broadened C_2H_2 and between 2.5 and 3.3 times the size of $\gamma_{2,N2}(T)$ for N_2-broadened C_2H_2, although the sign of the temperature dependent slope agrees in both cases. It is

noted, however, that the temperature dependence of the calculated diffusion coefficient does not match what is inferred from the observed line narrowing. Another consistency check is afforded by examination of the temperature dependence of the broadening [$\partial\gamma(T)/\partial T$] may be related to the speed-dependent narrowing as shown by Looney's[70] eqn. 5.46:

$$\gamma_2(T) = 2T\left(\frac{\mu}{m_a}\right)\left(\frac{\partial\gamma(T)}{\partial T}\right) \tag{3.22}$$

where μ is the reduced mass of the absorber and perturber. When the equations are evaluated, for pure C_2H_2 it is estimated γ_2= 0.012 from [$\partial\gamma(T)/\partial T$] while the fitted result (Table 3.9) is 0.022, both in cm^{-1} atm^{-1} units. The result is similar for the nitrogen broadened terms, with the value estimated from the T-dependence of $\gamma(T)$ approximately one half of the fitted narrowing value in Table 3.10.

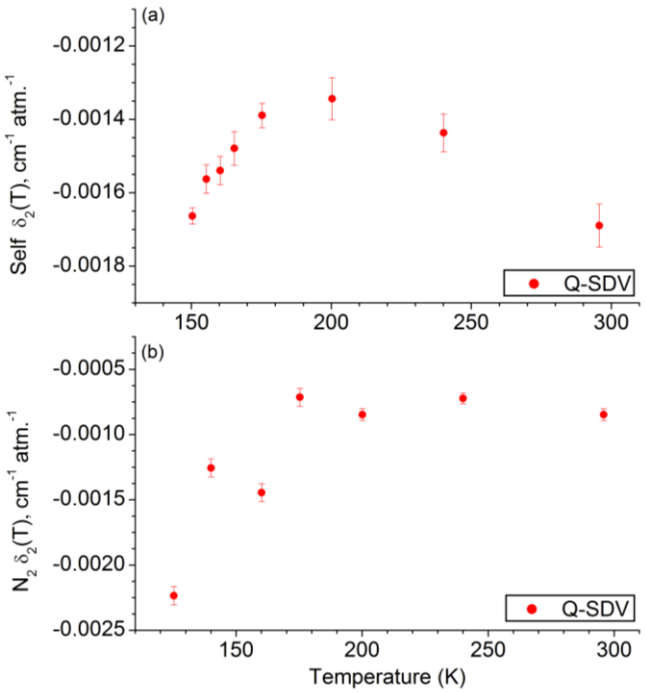

Figure 3.13: Temperature-dependent asymmetry $\delta_{2,i}(T)$ for (a) self- and (b)N_2-broadened measurements from the Q-SDV model. Plots were made with the final fit results from Tables 3.11 and 3.12. $\delta_{2,i}(T)$ as determined here has a clear non-power law temperature dependence which was not modeled. Error bars shown were obtained by assuming a 0.5% pressure uncertainty, see text for details.

It could be argued that modeled here are combined contributions to the line shape from Dicke and speed-dependent narrowing[69, 72] with a single effective (speed-dependent) parameter here. Physically, the Dicke narrowing should change the shape of the speed distribution in the gas, while speed-dependent narrowing is a result of slower moving molecules (near the line center) having fewer collisions. To investigate this, attempts were made to fix Dicke narrowing to the values derived from D_m, or scaled values that took into account the higher collision rates assumed in a soft collision model, but this did not improve the line shape fits; the parameters in the speed-dependent Galatry profile are completely correlated given the data. The analysis was not limited to strictly positive values for the narrowing mechanisms. It is possible that further measurements would permit the simultaneous determination of these closely related parameters. In the final determination the temperature dependence of the speed-dependent narrowing parameter was constrained to a power law and the $\gamma_2(T_0)$ and $n_{\gamma 2}$ were fit and are given in Tables 3.9 and 3.10. The results from the individual Q-SDV fits were included in Tables 3.11 and 3.12.

Values for the speed dependent shift parameter (δ_2) as a function of temperature plots are shown in Figure 3.13. These plots come from the final Q-SDV fit which uses the power law from eqn. 3.8 for the temperature dependence of the broadening, shifting, and narrowing. This is one of the first times that asymmetry parameters have been measured for acetylene line profiles and there are no precedents to compare to this. An apparent trend is noted, but it is not fit to a function here since the power law behavior seen in the other parameters is absent here. However, $\delta_{2,i}(T)$ points here can be used to get a very good estimate of $\delta_2(T)$ at other temperatures within the studied range using interpolation. The physical reason for the curve is unknown, but it is possible that not all the asymmetry comes from the speed-dependent shift. After looking at the concentration-dependent trends seen in Chapter 4 it is strongly believed that the cause of the curves seen here is underlying hot bands that are incorrectly accounted for in the Data Set III analysis. Other studies have modeled asymmetry using Dicke narrowing [63, 70] and an assumed correlation between velocity changing and dephasing processes. Typical data as referred to in Figure 3.7 shows the Q-SDV does effectively model the small observed line asymmetry in the current system. However, it is not clear why, in the case of self-broadening,

$\delta_{C2H2}(T)$ has a weak temperature dependence, while $\delta_{2,C2H2}(T)$ shows such a pronounced change with temperature.

F. Data Set III Conclusions

From data obtained using a frequency comb stabilized extended cavity diode laser, parameters for the self- and N2- broadened line shape for the P(11) transition in the ν1+ν3 band of acetylene have been determined to high accuracy. The results will be useful in the analysis of pressure-broadened spectra in various environments and determine accurate pressure-dependent broadening and shift parameters for comparison to theory. The analyses also reinforce the strengths and weaknesses of a multispectrum analysis that fits all temperatures and pressures simultaneously with a reduced set of parameters, but requires a more careful assessment of the error propagation. The SDV and Q-SDV model fits are very close to the noise level of the current experiment, but it is important to continue to test different types of models to assess their strengths and weaknesses as there are still small systematic differences between the observed and calculated line shapes. For the current work, however, observed asymmetry is small and either the SDV or Q-SDV models provide very good results. The multispectrum fit results in unrealistically small statistical uncertainties for line shape parameters when frequencies are highly accurate and pressure errors dominate the measurements. A more sensible estimate and upper limit was calculated using Monte Carlo methods to account for pressure uncertainties.

There is a preference for the Q-SDV model expressed, as it is here, in the time domain, as the resulting parameters are not dependent on approximations in a physically unrealistic model. The relaxation parameters in the Q-SDV, and the extended Q-SDV, model are model dependent only to the extent that the quadratic form has been assumed to describe the absorber speed dependence of the relaxation rate after collision with a partner with a Boltzmann distribution of speeds. These quantities can, in principle, be calculated from first principles using realistic intermolecular potentials and compared to the experimental results. Additionally the Q-SDV model allowed the identification of an unusual trend in the asymmetry parameter which would not have been noticeable in the SDV model.

Chapter 4: Future, Further Experimental Refinements

4.1. Spectrometer Improvements

Since the Data Set III experimental run, changes have been made to the experimental design in order to improve the signal-to-noise, locking stability, and the stability of the baseline. Figure 4.1 shows the improved design. An erbium-doped fiber amplifier takes the 1550 nm diode laser output of approx. 5 mW as an input and amplifies it to over 30 mW with the same polarization as before, and the same narrow frequency linewidth as before. For the line shape measurements, only approximately 5 mW of this amplified light is used, with the rest taken for the improved locking loop.

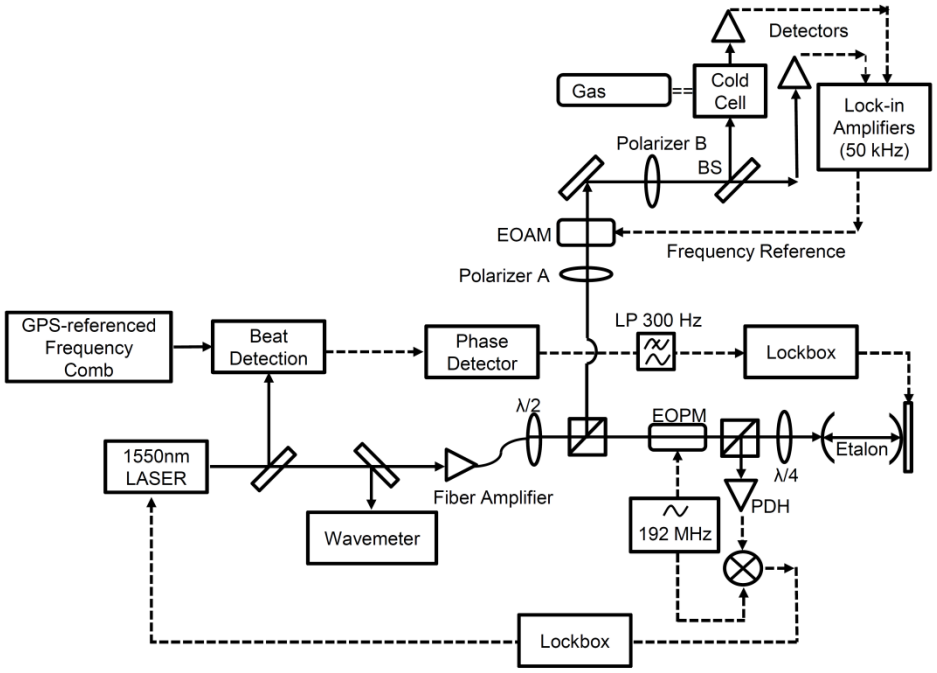

Figure 4.1: Experimental design for line shape measurements with all current improvements. BS= beamsplitter; EOAM= electro-optic amplitude modulator; EOPM= electro-optic phase modulator; PDH= detector for Pound-Drever-Hall method; Etalon= Toptica FPI 100.

The broadband plate beamsplitter labeled "BS" in Figure 4.1 is a nearly 50:50 split between reflection and transmission, with slight polarization dependence. The EOAM oscillates polarization between linear vertical and linear horizontal at the rate of the frequency reference,

50 kHz. Polarizer B is situated in a precision-rotated mount and is carefully set to an angle approximately halfway between vertical and horizontal polarization such that the light going on each path through the beamsplitter is equivalent, as measured on the two detectors. This alignment is far less prone to drift throughout a day of scanning in the ratio between the two channels than the previous design, which had a fixed polarizer and a $\lambda/2$ plate to set the channel ratio. The detectors are homemade with Hamamatsu G8605-11 InGaAs PIN photodiodes with large 1-mm active area and 18 MHz maximum frequency response. 5 cm focal length lenses combined with the large active area ensure that the entire beam hits the detectors. Two lock-in amplifiers are still used, but the first lock-in now records the difference between the two channels (Signal A-Baseline B) and the second lock-in records B. The ratio is then calculated as [(A-B)/B]+1, which still gives A/B as the signal ratio, but the first lock-in can be used with a lower voltage range, allowing for better dynamic range on detection.

The locking of the laser to the comb has also been improved. Seen for example in Figure 3.3 are noisy data points visible in the residuals that are the result of the laser-comb locking beat note locking off to the side instead of at the center. This results in data points taken at the wrong frequency, which is especially noticeable where the slope of the line profile is greatest; it is easy to see that this is the case in Figure 3.3. This issue happens after the software steps the comb. As a reminder the DDS controlling the frequency of the comb repetition rate (see discussion on page 9) changes in order to step the laser.

It was discovered that when the DDS changes frequency it does so very suddenly and this abrupt behavior occasionally causes the beat note to lock in the wrong position. This DDS was replaced with a different one, from Analog Devices, which waits for a close phase overlap between the old and new frequency, before changing. This means that the frequency stepping is much smoother.

Additionally software was developed and added to the scanning program. This software performs a Fourier transform on the error signal for the laser-comb beat note. By looking at the frequencies present when locked vs. unlocked, this program is calibrated to assume the laser is locked to the comb when the majority of frequencies are below a threshold frequency. This

routine was added between the stepping of the laser and the data acquisition portion of the scanning software, and would attempt to re-lock the laser, or, if unsuccessful, stop the scan.

If the lock is lost to the point of stopping the scan, in the previous Data Sets the scan would be lost. In order to further improve the lock, a temperature-stabilized Toptica FPI 100 Fabry-Perot Interferometer with free spectral range of 1 GHz was added as an intermediate between the CW laser and the frequency comb. Referencing again Figure 4.1, the majority of light from the fiber amplifier is sent into the resonant cavity, labeled "Etalon".

A technique known as the Pound-Drever-Hall method [105, 106] is used to lock the laser to the cavity. An electro-optic phase modulator (EOPM) is fed a 192 MHz frequency from a Marconi Signal Generator 2024 which is referenced to the same 10 MHz frequency reference as the rest of the experiment. This puts sidebands onto the laser which are separated from the carrier by the modulation frequency. One sideband is in-phase with the carrier and the other is of opposite phase. The laser passes through a beam splitter, then a $\lambda/4$ plate, then into the cavity. The reflected light will bounce back off the end mirror, through the $\lambda/4$ plate again and will reflect off the beamsplitter into the fast photodiode labeled "PDH". The beat notes between the carrier and each sideband are present at 192 MHz in this signal. The signal from this channel is demodulated at the 192 MHz, giving an error signal which is ideally zero when the two opposing phase beat notes cancel each other out, or a positive/negative signal when one beat note is greater than the other. Using this signal, the laser is then locked using a PID lockbox such that the carrier light is resonant with the cavity, and transmission through the cavity is at a maximum. The laser remains locked to the cavity because when one or the other begins to drift the error signal will drift positive or negative, allowing the lockbox to compensate in the correct direction. The lockbox sends a signal to the RF portion of a bias tee in the same way as described on page 9.

The cavity length is adjusted by a piezo, which responds slowly and is resistant to high frequency noise, especially when the piezo control has a lowpass filter (300 Hz) applied as is the case here. This gives the lock very good short term stability, reducing the chance that high frequency noise will break the lock to the laser. In order to maintain the long term stability, and

frequency accuracy, the lock to the frequency comb still needs to be maintained. The beat note between the laser and comb is still detected in the beat detection unit from Figure 2.4. However, instead of having the resulting error signal fed into the CW laser, it is fed into the piezo control for the cavity. Therefore the laser is still locked to the comb but with the added locking stability of the etalon, and the frequency ultimately dictated by the same equation 2.4 as before.

Previously the length of a scan was limited by the servo-lock voltage for the repetition rate frequency lock as mentioned on page 20. As the spectrometer is scanned this voltage slowly crawls from one maximum value to the other, previously limiting the length of the scan. With the improvements mentioned in this section (and some minor software additions) it became routine to simply pause a scan and "re-set" the repetition rate locking voltage, then continue a scan, without even losing lock. This means that a scan is now limited by either the available scanning voltage of the piezo in the resonant cavity, or the CW laser's piezo stepping range; the latter limits us to about 18 GHz scanning range in this case. Moving forward, this has eliminated the need to concatenate several files to get a full line profile, as shown in the following section.

Table 4.1: List of scans taken with C_2H_2-N_2 mixtures, by C_2H_2 concentration in Data Set IV. All temperatures are 296 K.

C_2H_2 Concentration	Total Pressure
1%	25
	50
	100
	200
	400
	750
5%	5
	10
	20
	50
	100
10%	5
	20
	50
	100

4.2. Data Set IV

On page 50 it is mentioned that C_2H_2-N_2 scans which had very high (25%/50%) C_2H_2 concentrations were not able to be fit along with the low (~1%) concentration data. For the purpose of investigating this concern a trend of varying concentration scans were made as outlined in Table 4.1. These scans were taken with all the improvements mentioned in Section 4.1. Figure 4.2 shows an example spectrum. It should be noted that the scan shown here is about 18 GHz long and was taken in a single scan rather than multiple smaller parts. Baseline drift is not detectable here. Seen in Figure 4.3 the noise grows near the line center. It is being investigated whether this noise is due to frequency jitter, lock-in rounding errors, or some other effect. Since the scans are larger, something that previously appeared to be a fringe or baseline curvature is shown to actually be the direct result of underlying hot band transitions. The magnified portion of the scan shows a feature resulting from at least 3 overlapping hot bands. A full list of hot bands over the range of this scan, as reported in HITRAN[82], is in Table 3.2.

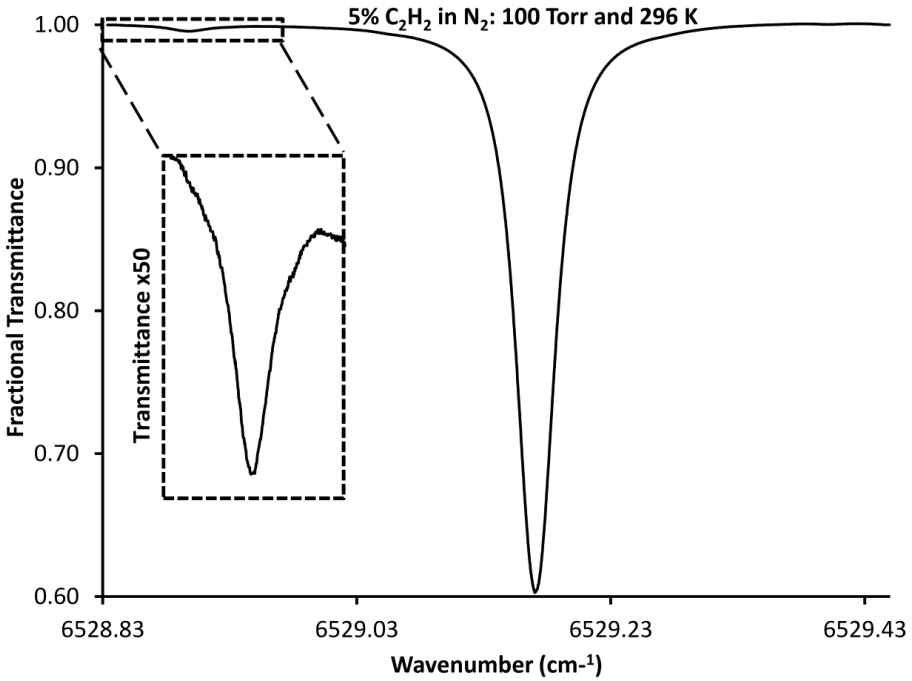

Figure 4.2: Example spectrum from Data Set IV. The subplot contains a magnified view of three hot band transitions that are visibly overlapping the main line.

An overlay of a preliminary, single-file SDV fit residual (O-C) to the data from Figure 4.2 is shown in Figure 4.3. Also shown in this figure are the reported HITRAN positions and relative line strengths for the transitions from Table 3.2. Only the bold-labeled transitions in Table 3.2 were included in the analysis of Data Sets I, II, and III. Figures 4.2 and 4.3 strongly suggest that all transitions listed in Table 3.2 should be taken into account . Although a full analysis has not yet confirmed the following, it is a strong possibility that many of the concerns raised in the analysis of the previous data sets can be explained by a more thorough account of the overlapping transitions.

The shape of the plots in Figure 3.13 suggests that hot bands are growing in at around 200 K. Since there are more hot bands on one side of the fundamental transition than on the other, the speed-dependent asymmetry $\delta_{2,i}(T)$ parameters are most strongly affected. Below 200 K the hot band intensities would be negligible and a very smooth trend is noted especially in the pure C_2H_2 plot here.

The varying spectra of different concentrations that would not fit together also make sense. Since hot band intensity, which was not being correctly accounted for, varies greatly with acetylene pressure, the multispectrum fitted parameters would have trouble fitting all files when concentrations varied. Using a single concentration allows the program to fit, but the resulting parameters will be the result of accommodating the lines that weren't included and not true values. It is also likely that such an effect would go unnoticed in the pure acetylene data since these entire sets of data are at a single concentration of 100%. Varying fitted intensity concerns mentioned on page 36 may also be the result of these hot band lines growing in more at higher pressures.

The solution to the concerns here is to appropriately include the hot band lines in the multispectrum fitting analysis. As suggested by Figure 4.3, the overlapping hot band lines are not found exactly in the positions reported in HITRAN. Even the two hot bands that were included in the analysis of Data Sets I-III are at the wrong positions. For example, Figure 4.3 suggests that the R(11)e line of the $101(20)^0$+u$\leftarrow$$000(20)^0$+g transition is about 220 MHz away from the value reported in HITRAN. This is a preliminary fit but even the 3-30 MHz or higher

uncertainty reported in the original measurement [92] would be more than enough to negatively affect the reported line shape parameters. Additionally, there are at least two transitions seen clearly in the fit residuals in Figure 4.3 which have no matching transitions in the database. The best solution is to take advantage of the high accuracy of the frequency comb to measure the positions of the underlying hot band lines.

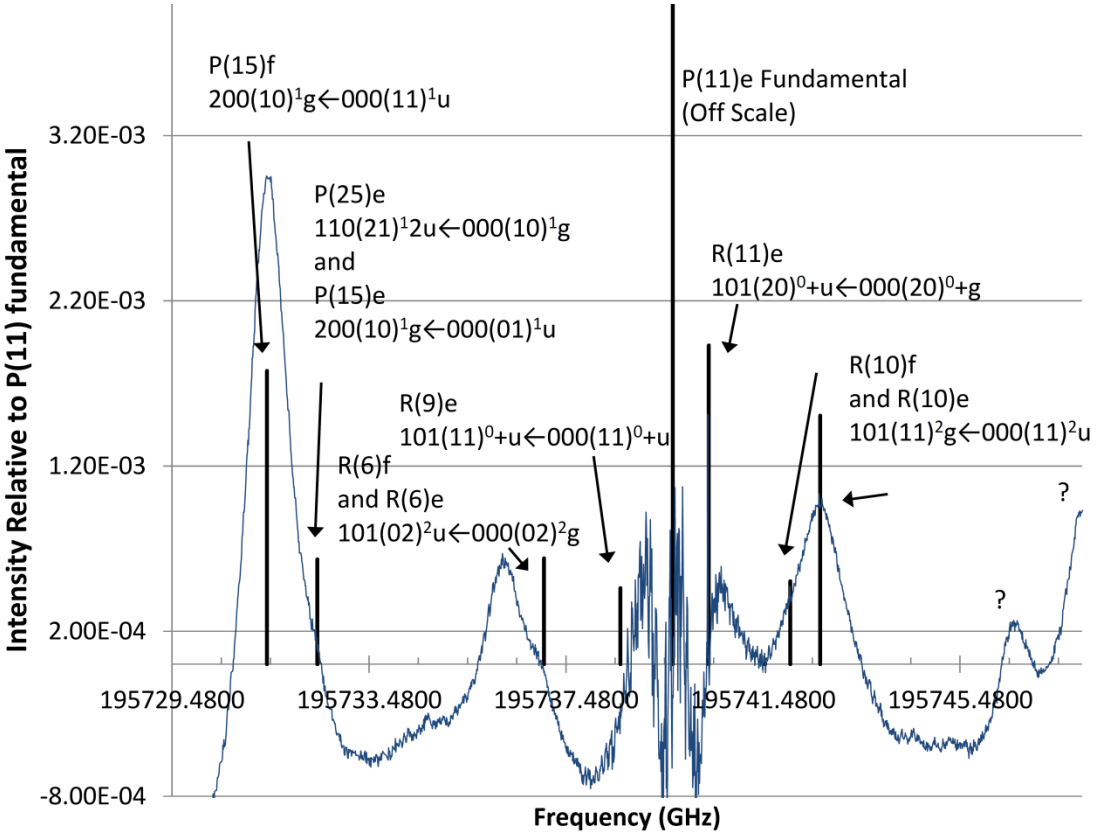

Figure 4.3: Stick representation of the hot bands in the region of interest plotted at intensities relative to the P(11) line of the $\nu_1 + \nu_3$ band. Overlaid is the residual plot obtained from a scan of 5% C_2H_2 in N_2 at 296 K fit with the SDV model fitting only P(11), with hot band transitions unaccounted for.

4.3. Line Position Measurements

a. Preliminary measurement of spectrometer's accuracy

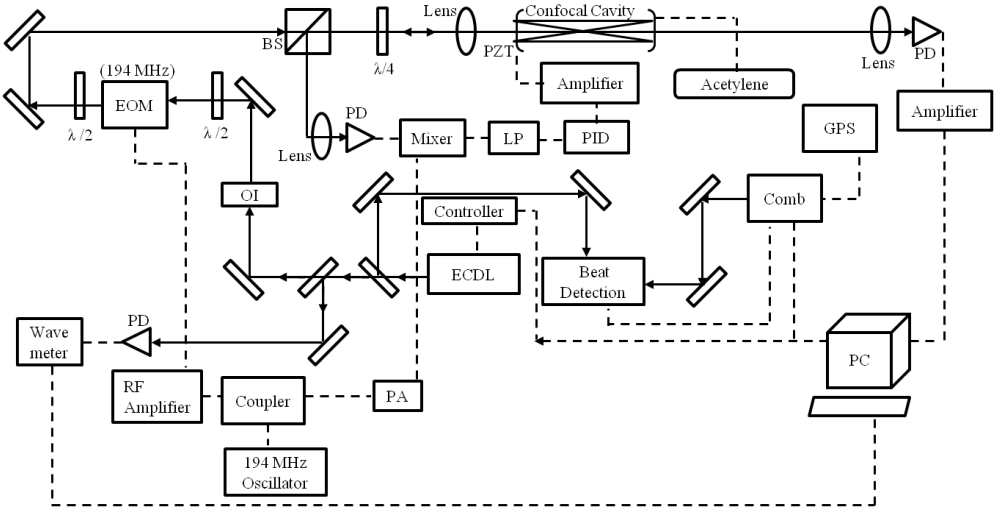

Figure 4.4: Block diagram of the spectrometer used for sub-Doppler saturation dip measurements of the P(11) line in the $\nu_1 + \nu_3$ band of $^{12}C_2H_2$. ECDL=extended cavity diode laser, EOM = electro-optic modulator, OI= optical isolator, PD=photodiode detector, LP=Lowpass filter, BS=beam splitter, PA=phase adjustment, PZT=piezo electric translator, PID=Pound-Drever-Hall locking.

The very first experiment done with the frequency comb was in order to characterize the absolute accuracy and precision attainable with this system[14]. A sub-Doppler saturation dip measurement was made of the P(11) line in the $\nu_1 + \nu_3$ band of acetylene. A resonant cavity-based absorption cell was designed and constructed using a confocal mirror arrangement since the optical pumping rate attainable using the ECDL with powers of 2-3 mW is generally lower than the collisional dephasing rate in samples at pressures of more than a few mTorr. The cavity was locked to the laser frequency which was itself locked to the frequency comb as the spectrometer frequency was scanned by small adjustments of the nominal 250 MHz comb repetition rate. This is in contrast to the locking described in section 4.1 where the laser was

locked to the cavity. There was also no temperature stabilization for the cavity. Cavity locking was achieved using the Pound-Drever-Hall scheme[105, 106]. Figure 4.4 shows a schematic of the spectrometer as configured for the sub-Doppler experiments.

With reference to Figure 4.4, part of the output from the 1550 nm (ECDL) laser (located toward the middle of the figure), is combined with the comb output in the beat detection unit. The main beam is directed to an optical isolator, an electro-optic phase modulator (New Focus model 4003 resonant modulator operating at 194 MHz), various optical components for polarization control, and finally through the confocal cavity/absorption cell to a New Focus model 2053 InGaAs-based receiver.

Figure 4.5 shows the measurement of the sub-Doppler saturation dip feature for P(11) recorded in the 1-meter long confocal cavity and a pressure of 5 mTorr of C_2H_2 at ambient temperature. The measured width (HWHM) of the resonance is 105(2) kHz. Saturation dip sub-Doppler spectra of lines in this band of C_2H_2 have previously been measured and used as secondary frequency standards[12]. The measured frequency of 195 739.649 513 5 (80) GHz is within the error limits of the published measurements[12] hence confirming the stability and accuracy of the system.

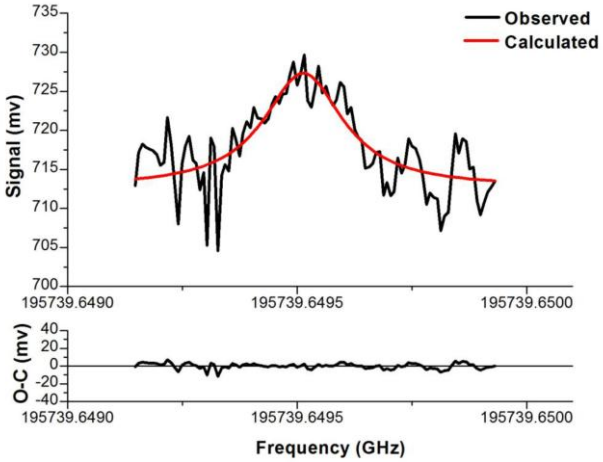

Figure 4.5: Sub-Doppler saturation dip signal for the P(11) line in the $\nu_1 + \nu_3$ band of $^{12}C_2H_2$. 5 mTorr of C_2H_2 was used in a 1 meter long confocal cavity with finesse measured to be 65. Incident laser power was 3 mW. O-C is the observed minus calculated residual. The fitted linewidth is 105(2) kHz. (HWHM).

b. Line Position measurements of hot bands

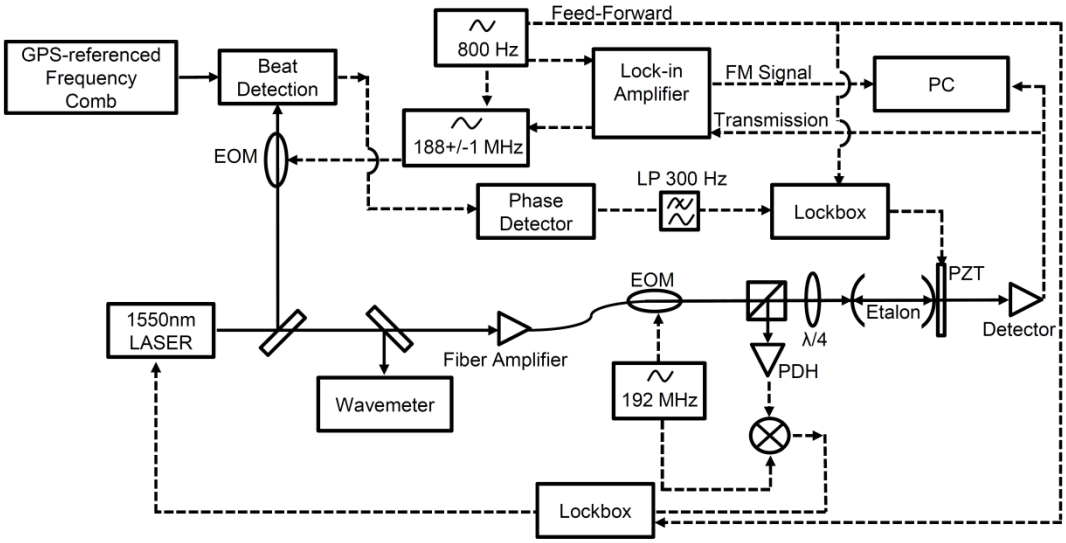

Figure 4.6: Experimental design for the sub-Doppler measurement of hot band positions. LP=lowpass filter; EOM= electro-optic phase modulator; PDH= detector for Pound-Drever-Hall technique.

This experiment was designed to measure the line positions of many weaker hot band lines to an accuracy comparable to the known frequency of the P(11) line of the $\nu_1 + \nu_3$ band. Figure 4.6 shows the experimental design. The locking scheme is similar to that described in Chapter 4.1. A new resonant cavity has a base free spectral range ($c/6l$) of 300 MHz, where l is the cavity length. In the beam path that leads to the beat detection unit, a second EOPM is present. This EOPM receives a frequency from a voltage-controlled oscillator (VCO) which is set to 188 MHz and is referenced to the 10 MHz frequency standard. One of the sidebands is then locked to the frequency comb in the beat detection unit, instead of locking the carrier.

An 800 Hz sine wave is fed from a signal generator into the VCO, at an amplitude that produces a change in VCO frequency of 2 MHz. This causes the output of the VCO to oscillate between 187 and 189 MHz, at a rate of 800 Hz. This in turn causes an oscillation in the spacing between the carrier and sidebands. Since a sideband is locked to the comb at a fixed frequency,

the carrier itself actually oscillates +/- 1 MHz about its center frequency. The 800 Hz is then fed forward to the lockboxes controlling the laser-cavity lock and the cavity-frequency comb lock.

The detector is a New Focus 10 MHz photoreceiver. The output is fed into a lock-in amplifier where lock-in detection gives the amplitude of the signal at 800 Hz. The spectrometer is scanned over a saturation dip, pausing at each data point to collect an averaged signal. This gives the slope of the saturation dip at each point, resulting in a spectrum that looks like the first derivative of the feature fit in Figure 4.5.

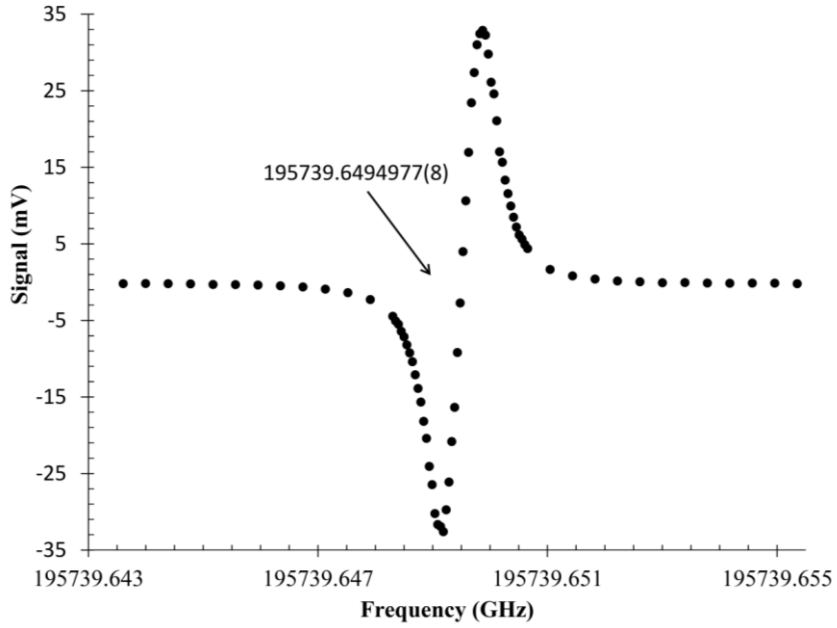

Figure 4.7: Spectrum of the C_2H_2 P(11) line of $\nu_1 + \nu_3$ transition, at 5 mTorr taken with the spectrometer from Figure 4.6.

Figure 4.7 shows the P(11) line center measured at 5 mTorr. These spectra are fit using 2 Lorentzians of opposing signs separated by the modulation frequency. This determination is about 25 kHz away from the published value[12] and determination of the absolute accuracy of this technique are ongoing. Figure 4.8 shows a measurement made of the $R(12)_f$ of the $101(10)^1u \leftarrow 000(10)^1g$ transition. This transition has an intensity that is .046 relative to the $P(11)_e$, for reference. It is found to be offset from HITRAN's reported value by 11 MHz, reinforcing the need to measure the hot band lines in the region of interest. Figure 4.9, the $P(2)_e$ of the $101(10)^1u \leftarrow 000(10)^1g$ transition, is currently the weakest line position measured with a

relative intensity of about 0.004, making it of similar intensity to some of the hot bands in the region of interest. The frequency comb-referenced determination of this line is offset 5 MHz from HITRAN's reported value.

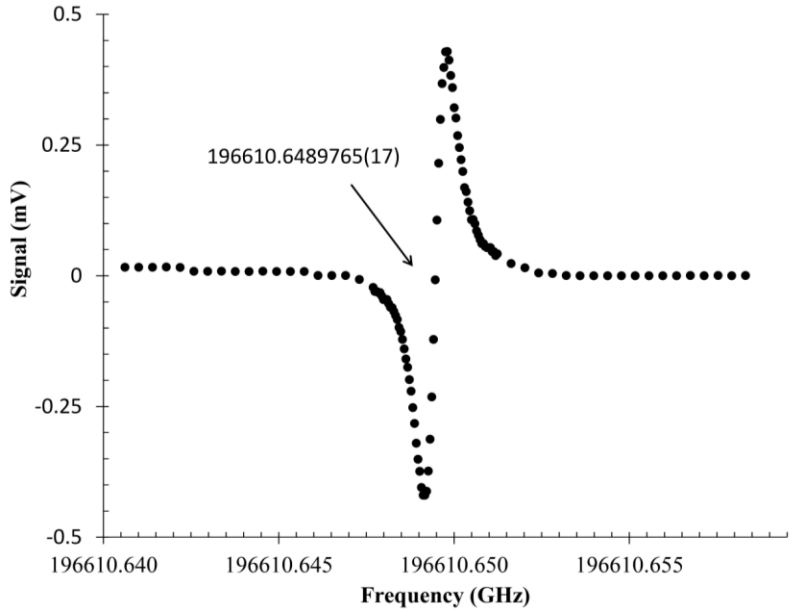

Figure 4.8: Spectrum of the C_2H_2 $R(12)_f$ line of $101(10)^1u \leftarrow 000(10)^1g$ transition, at 18 mTorr taken with the spectrometer from Figure 4.6.

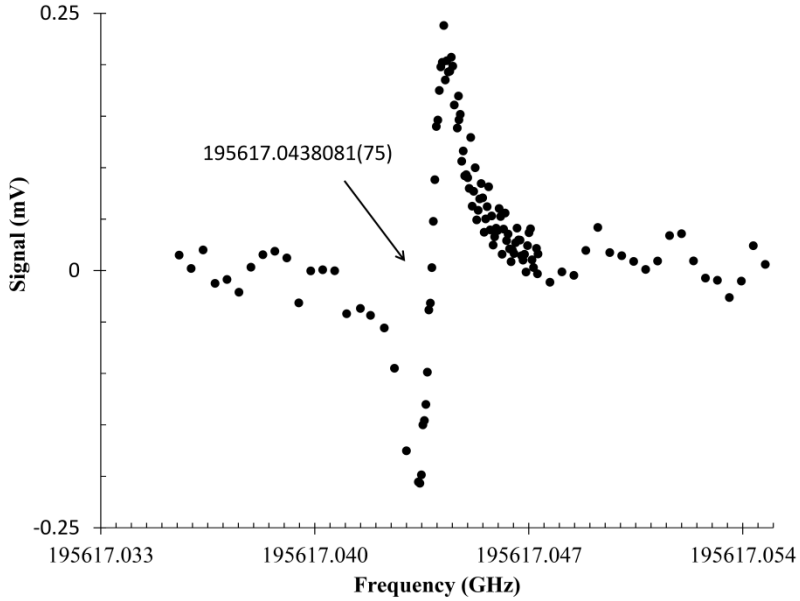

Figure 4.9 : Spectrum of the C_2H_2 $P(2)_e$ line of $101(10)^1u \leftarrow 000(10)^1g$ transition, at 26 mTorr taken with the spectrometer from Figure 4.6.

High accuracy measurements of the hot band lines in Table 3.2 are expected to make the analysis of scans like Figure 4.2 possible, with residuals near the experimental noise level. More importantly, the multispectrum fits in Data Set III in particular can be repeated with improved accounting of hot band effects in order to achieve more precise values for the line shape model parameters. It will be interesting to see if the unusual trends in the speed dependent asymmetry parameter will more closely match those found in the other fit parameters when using the Q-SDV profile.

Measurements are currently underway to determine updated spectroscopic constants for the relatively strong hot bands of the $101(10)^1u \leftarrow 000(10)^1g$ and $101(01)^1g \leftarrow 000(01)^1u$ transitions. As shown in Figures 4.10 and 4.11, the measurements of these hot bands are essential for the accurate modeling of other rotational lines in the $\nu_1 + \nu_3$ band, with line strengths approaching the same height as the P(1) line at 296 K.

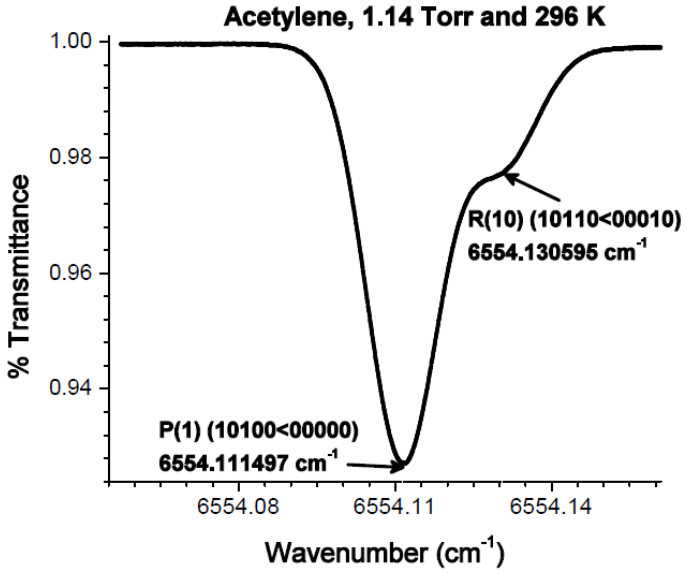

Figure 4.10: C_2H_2 P(1) line of $\nu_1 + \nu_3$ transition at 1.14 Torr and 296 K. The transition frequencies listed were measured using the spectrometer in Figure 4.6.

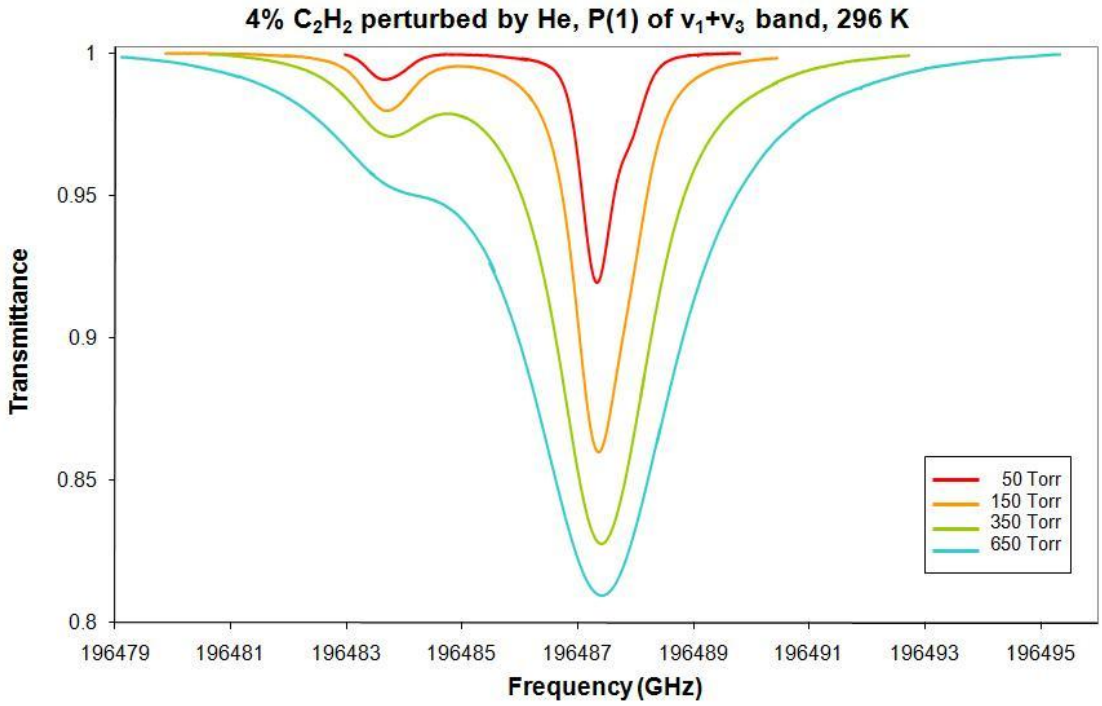

Figure 4.11: C_2H_2 P(1) line of $\nu_1 + \nu_3$ transition, 4% concentration in He at 296 K with varying total pressures. Also present are numerous, large overlapping hot band transitions.

References

[1] M. Cich, C. McRaven, G. Lopez, T. Sears, D. Hurtmans, A. Mantz, *Applied Physics B: Lasers and Optics* 109 (2012) 373-384.

[2] T. Udem, R. Holzwarth, T.W. Hansch, *Nature* 416 (2002) 233-237.

[3] D.J. Jones, S.A. Diddams, J.K. Ranka, A. Stenz, R.S. Windeler, J.L. Hall, S.T. Cundiff, *Science* 288 (2000) 635-639.

[4] S.A. Diddams, D.J. Jones, J. Ye, S.T. Cundiff, J.L. Hall, J.K. Ranka, R.S. Windeler, R. Holzwarth, T. Udem, T.W. Hansch, *Phys. Rev. Letts.* 84 (2000) 5102-5105.

[5] B.R. Washburn, S.A. Diddams, N.R. Newbury, J. Nicholson, M.F. Yan, C.G. Jurgensen, *Opt. Letts.* 29 (2004) 250-252.

[6] S.A. Diddams, T. Udem, J.C. Bergquist, E.A. Curtis, R.E. Drullinger, L. Hollberg, W.M. Itano, W.D. Lee, C.W. Oates, K.R. Vogel, D.J. Wineland, *Science* 293 (2001) 825-828.

[7] S.A. Diddams, L. Hollberg, V. Mbele, *Nature* 445 (2007) 627-630.

[8] I. Coddington, W.C. Swann, N.R. Newbury, *Phys. Rev. Letts.* 100 (2008) 013902(4).

[9] B. Bernhardt, A. Ozawa, P. Jacquet, M. Jacquey, Y. Kobayashi, T. Udem, R. Holzwarth, G. Guelachvili, T.W. Hansch, N. Picque, *Nature Phot.* 4 (2010) 55-57.

[10] C. Gohle, B. Stein, A. Schliesser, T. Udem, T.W. Hansch, *Phys. Rev. Lett.* 99 (2007) 263902.

[11] S.W. Arteaga, C.M. Bejger, J.L. Gerecke, J.L. Hardwick, Z.T. Martin, J. Mayo, E.A. McIlhattan, J.-M.F. Moreau, M.J. Pilkenton, M.J. Polston, B.T. Robertson, E.N. Wolf, *J. Molec. Spectrosc.* 243 (2007) 253-266.

[12] A.A. Madej, A.J. Alcock, A. Czajkowski, J.E. Bernard, S. Chepurov, *J. Opt. Soc. Amer. B* 23 (2006) 2200-2208.

[13] A. Amy-Klein, H. Vigué, C. Chardonnet, *Journal of Molecular Spectroscopy* 228 (2004) 206-212.

[14] C.P. McRaven, M.J. Cich, G.V. Lopez, T.J. Sears, D. Hurtmans, A.W. Mantz, *J. Molec. Spectrosc.* 266 (2011) 43-51.

[15] A. Valentin, *Spectrochim. Acta. A* 52 (1996) 823-833.

[16] A. Valentin, C. Nicholas, L. Henry, A.W. Mantz, *Appl. Opt.* 26 (1987) 41-46.

[17] H.S. Margolis, *Chemical Society Reviews* (2012).

[18] A. Gambetta, D. Gatti, A. Castrillo, N. Coluccelli, G. Galzerano, P. Laporta, L. Gianfrani, M. Marangoni, *Applied Physics B: Lasers and Optics* (2012) 1-6.

[19] D.A. Long, G.-W. Truong, R.V. Zee, D.F. Plusquellic, J.T. Hodges, 68th Ohio State University International Symposium on Molecular Spectroscopy, Columbus, OH, 2013.

[20] P. Varanasi, R.P. Bangaru, *J. Quant. Spectrosc. Radiat. Transf.* 15 (1975) 267-273.

[21] P. Minutolo, C. Corsi, F. D'Amato, M. DeRosa, *Eur. Phys. J. D* 17 (2001) 175-179.

[22] S.L. Gilbert, W.C. Swann, *NIST special publication* 260 (2001) 133.

[23] M. De Labachelerie, K. Nakagawa, M. Ohtsu, *Optics letters* 19 (1994) 840-842.

[24] K. Nakagawa, M. De Labachelerie, Y. Awaji, M. Kourogi, *JOSA B* 13 (1996) 2708-2714.

[25] C.S. Edwards, H.S. Margolis, G.P. Barwood, S.N. Lea, P. Gill, G. Huang, W.R.C. Rowley, *Optics letters* 29 (2004) 566-568.

[26] C.S. Edwards, G.P. Barwood, H.S. Margolis, P. Gill, W.R.C. Rowley, *Journal of Molecular Spectroscopy* 234 (2005) 143-148.

[27] C.S. Edwards, H.S. Margolis, G.P. Barwood, S.N. Lea, P. Gill, W.R.C. Rowley, *Appl. Phys. B* 80 (2005) 977-983.

[28] J. Rudolph, D.H. Ehhalt, A. Khedim, *Journal of Atmospheric Chemistry* 2 (1984) 117-124.

[29] R. Zander, C.P. Rinsland, D.H. Ehhalt, J. Rudolph, P. Demoulin, *Journal of Atmospheric Chemistry* 13 (1991) 359-372.

[30] A. Goldman, F. Murcray, R. Blatherwick, J. Gillis, F. Bonomo, F. Murcray, D. Murcray, R. Cicerone, *Journal of Geophysical Research* 86 (1981) 12143-12,146.

[31] M. Kanakidou, B. Bonsang, J. Le Roulley, G. Lambert, D. Martin, G. Sennequier, *Nature* 333 (1988) 51-52.

[32] R.S. Oremland, M.A. Voytek, *Astrobiology* 8 (2008) 45-58.

[33] V. Kunde, F. Flasar, D. Jennings, B. Bézard, D. Strobel, B. Conrath, C. Nixon, G. Bjoraker, P. Romani, R. Achterberg, *Science* 305 (2004) 1582-1586.

[34] A. Coustenis, *Space Science Reviews* 116 (2005) 171-184.

[35] C.P. McKay, J.B. Pollack, R. Courtin, *Science* 253 (1991) 1118-1121.

[36] P. Drossart, B. Bezard, S. Atreya, J. Lacy, E. Serabyn, A. Tokunaga, T. Encrenaz, *Icarus* 66 (1986) 610-618.

[37] H.B. Niemann, S.K. Atreya, S.J. Bauer, G.R. Carignan, J.E. Demick, R.L. Frost, D. Gautier, J.A. Haberman, D.N. Harpold, D.M. Hunten, G. Israel, J.I. Lunine, W.T. Kasprzak, T.C. Owen, M. Paulkovich, F. Raulin, E. Raaen, S.H. Way, *Nature* 438 (2005) 779-784.

[38] K. Didriche, M. Herman, *Chemical Physics Letters* 496 (2010) 1-7.

[39] N.T. Campbell, J.D. Cook, B.A. Coombs, E.P. Fuller, J.L. Hardwick, S.M. Hurley, L.K. Ho, P.A. Kovac, E.J. Robertson, E.N. Senning, J.K. Utterback, R.S. Wiser, *Molecular Physics* 109 (2011) 2199-2208.

[40] H. Rozario, J. Garber, C. Povey, D. Hurtmans, J. Buldyreva, A. Predoi-Cross, *Molecular Physics* 110 (2012) 2645-2663.

[41] K.S. Bond, N.D. Collett, J.L. Hardwick, E.E. Hinds, T.W. Keiber, I.S.G. Kelly-Morgan, C.M. Matthys, M.J. Pilkenton, K.W. Sinclair, A.A. Taylor, *Appl. Phys. B* 90 (2008) 255-262.

[42] C. Povey, M. Guillorel-Obregon, A. Predoi-Cross, S.V. Ivanov, O.G. Buzykin, F. Thibault, *Canadian Journal of Physics* (2013) DOI: 10.1139/cjp-2013-0031.

[43] M.J. Cich, D. Forthomme, C.P. McRaven, G.V. Lopez, G.E. Hall, T.J. Sears, A.W. Mantz, *The Journal of Physical Chemistry A* (2013).

[44] J.M. Hartmann, C. Boulet, D. Robert, Collisional Effects on Molecular Spectra. First ed.; Elsevier, Amsterdam, 2008.

[45] S.G. Rautian, I.I. Sobel'man, *Sov. Phys. Uspekhi* 9 (1967) 701-716.

[46] B. Lance, G. Blanquet, J. Walrand, J.P. Bouanich, *Journal of Molecular Spectroscopy* 185 (1997) 262-271.

[47] L. Galatry, *Phys. Rev. Lett.* 122 (1961) 1218-1223.

[48] D. Hurtmans, G. Dufour, W. Bell, A. Henry, A. Valentin, C. Camy-Peyret, *J. Molec. Spectrosc.* 215 (2002) 128-133.

[49] J. Ward, J. Cooper, E.W. Smith, *Journal of Quantitative Spectroscopy & Radiative Transfer* 14 (1974) 555-590.

[50] D.C. Benner, C.P. Rinsland, V.M. Devi, M.A.H. Smith, D. Atkins, *Journal of Quantitative Spectroscopy and Radiative Transfer* 53 (1995) 705-721.

[51] L.S. Rothman, I.E. Gordon, A. Barbe, D.C. Benner, P.E. Bernath, M. Birk, V. Boudon, L.R. Brown, A. Campargue, J.P. Champion, K. Chance, L.H. Coudert, V. Dana, V.M. Devi, S. Fally, J.M. Flaud, R.R. Gamache, A. Goldman, D. Jacquemart, I. Kleiner, N. Lacome, W.J. Lafferty, J.Y. Mandin, S.T. Massie, S.N. Mikhailenko, C.E. Miller, N. Moazzen-Ahmadi, O.V. Naumenko, A.V. Nikitin, J. Orphal, V.I. Perevalov, A. Perrin, A. Predoi-Cross, C.P. Rinsland, M. Rotger, M. Simeckova, M.A.H. Smith, K. Sung, S.A. Tashkun, J. Tennyson, R.A. Toth, A.C. Vandaele, J. Vander Auwera, *Journal of Quantitative Spectroscopy & Radiative Transfer* 110 (2009) 533-572.

[52] R. Stolen, C. Lin, *Physical Review A* 17 (1978) 1448.

[53] W. Chen, J. Cousin, E. Poullet, J. Burie, D. Boucher, X. Gao, M.W. Sigrist, F.K. Tittel, *Comptes Rendus Physique* 8 (2007) 1129-1150.

[54] A.W. Mantz, V. Malathy-Devi, D.C. Benner, M.A.H. Smith, A. Peredoi-Cross, M. Dulick, *J. Molec. Structure*. 742 (2005) 99-100.

[55] A. Tickner, F. Lossing, *The Journal of Physical Chemistry* 55 (1951) 733-740.

[56] A. Valentin, A. Henry, C. Claveau, D. Hurtmans, A.W. Mantz, *Molec. Phys.* 102 (2004) 1793-1802.

[57] K. Sung, A.W. Mantz, M.A.H. Smith, L.R. Brown, T.J. Crawford, V. Malathy-Devi, D.C. Benner, *J. Molec. Spectrosc.* 262 (2010) 122-134.

[58] R.J. Wells, *J. Quant. Spectrosc. Radiat. Transf.* 62 (1999) 29-48.

[59] J.S. Li, G. Durry, J. Cousin, L. Joly, B. Parvitte, V. Zeninari, *J. Quant. Spectrosc. Radiat. Transf.* 111 (2010) 2332-2340.

[60] R.H. Dicke, *Physical Review* 89 (1953) 472-473.

[61] J.P. Wittke, R.H. Dicke, *Physical Review* 103 (1956) 620-631.

[62] J.O. Hirschfelder, C.F. Curtiss, R.B. Bird, Molecular theory of gases and liquids. Wiley New York, 1954.

[63] A. Pine, *The Journal of chemical physics* 101 (1994) 3444.

[64] M. Nelkin, A. Ghatak, *Phys. Rev.* 135 (1964) A4-A9.

[65] R. Ciurylo, A.S. Pine, J. Szudy, *Journal of Quantitative Spectroscopy & Radiative Transfer* 68 (2001) 257-271.

[66] A.W. Mantz, A. Henry, A. Valentin, *J. Molec. Spectrosc.* 207 (2001) 113-119.

[67] R.L. Farrow, L.A. Rahn, G.O. Sitz, G.J. Rosasco, *Phys. Rev. Lett.* 63 (1989) 746-749.

[68] D. Lisak, G. Rusciano, A. Sasso, *Journal of Molecular Spectroscopy* 227 (2004) 162-171.

[69] D. Lisak, G. Rusciano, A. Sasso, *Physical Review A* 72 (2005).

[70] J.P. Looney, Pennsylvania State University, 1987.

[71] P. Duggan, P.M. Sinclair, A.D. May, J.R. Drummond, *Physical Review A* 51 (1995) 218-224.

[72] P. Duggan, P. Sinclair, R. Berman, A. May, J.R. Drummond, *Journal of molecular spectroscopy* 186 (1997) 90-98.

[73] P.R. Berman, *Journal of Quantitative Spectroscopy & Radiative Transfer* 12 (1972) 1331-1342.

[74] H.M. Pickett, *Journal of Chemical Physics* 73 (1980) 6090-6094.

[75] A. Henry, D. Hurtmans, M. MargottinMaclou, A. Valentin, *Journal of Quantitative Spectroscopy & Radiative Transfer* 56 (1996) 647-671.

[76] D. Hurtmans, A. Henry, A. Valentin, C. Boulet, *Journal of Molecular Spectroscopy* 254 (2009) 126-136.

[77] S. Chapman, T.G. Cowling, The Mathematical Theory of Non-uniform Gases. Camb. Univ. Press, New York, 1958.

[78] J.F. D'Eu, B. Lemoine, F. Rohart, *Journal of molecular spectroscopy* 212 (2002) 96-110.

[79] C.D. Boone, K.A. Walker, P.F. Bernath, *Journal of Quantitative Spectroscopy and Radiative Transfer* 112 (2011) 980-989.

[80] R. Ciuryło, J. Szudy, *Journal of Quantitative Spectroscopy and Radiative Transfer* 57 (1997) 411-423.

[81] A.S. Pine, *Journal of Quantitative Spectroscopy & Radiative Transfer* 62 (1999) 397-423.

[82] L.S. Rothman, I.E. Gordon, Y. Babikov, A. Barbe, D. Chris Benner, P.F. Bernath, M. Birk, L. Bizzocchi, V. Boudon, L.R. Brown, A. Campargue, K. Chance, E.A. Cohen, L.H. Coudert, V.M. Devi, B.J. Drouin, A. Fayt, J.M. Flaud, R.R. Gamache, J.J. Harrison, J.M. Hartmann, C. Hill, J.T. Hodges, D. Jacquemart, A. Jolly, J. Lamouroux, R.J. Le Roy, G. Li, D.A. Long, O.M. Lyulin, C.J. Mackie, S.T. Massie, S. Mikhailenko, H.S.P. Müller, O.V. Naumenko, A.V. Nikitin, J. Orphal, V. Perevalov, A. Perrin, E.R. Polovtseva, C. Richard, M.A.H. Smith, E. Starikova, K. Sung, S. Tashkun, J. Tennyson, G.C. Toon, V.G. Tyuterev, G. Wagner, *Journal of Quantitative Spectroscopy and Radiative Transfer* 130 (2013) 4-50.

[83] C. Povey, A. Predoi-Cross, D.R. Hurtmans, *Journal of Molecular Spectroscopy* 268 (2011) 177-188.

[84] J.P. Bouanich, A. Predoi-Cross, *Molecular Physics* 109 (2011) 2071-2081.

[85] D. Forthomme, C.P. McRaven, T.J. Sears, G.E. Hall, *The Journal of Physical Chemistry A* (2013) DOI: 10.1021/jp4030359.

[86] M.A. Koshelev, M.Y. Tretyakov, F. Rohart, J.-P. Bouanich, *The Journal of Chemical Physics* 136 (2012) 124316.

[87] D. Priem, F. Rohart, J.-M. Colmont, G. Wlodarczak, J.-P. Bouanich, *Journal of Molecular Structure* 517 (2000) 435-454.

[88] R. Gamache, S. Kennedy, R. Hawkins, L. Rothman, *Journal of Molecular Structure* 517 (2000) 407-425.

[89] J.S. Li, L. Joly, J. Cousin, B. Parvitte, B. Bonno, V. Zeninari, G. Durry, *Spectrochim. Acta. A* 74 (2009) 1204-1208.

[90] P. Varanasi, R.P. Bangaru, *J. Quant. Spectrosc. Radiat. Transf.* 15 (1975) 267-273.

[91] P.W. Rosenkranz, *Ieee Transactions on Antennas and Propagation* AP23 (1975) 498-506.

[92] D. Jacquemart, N. Lacome, J.-Y. Mandin, V. Dana, H. Tran, F.K. Gueye, O.M. Lyulin, V.I. Perevalov, L. Régalia-Jarlot, *Journal of Quantitative Spectroscopy and Radiative Transfer* 110 (2009) 717-732.

[93] R. El Hachtouki, J. Vander Auwera, *Journal of Molecular Spectroscopy* 216 (2002) 355-362.

[94] G. Bottomley, C. Reeves, G. Seiflow, *Journal of Applied Chemistry* 9 (1959) 517-518.

[95] R.R. Gamache, E. Arié, C. Boursier, J.-M. Hartmann, *Spectrochimica Acta Part A: Molecular and Biomolecular Spectroscopy* 54 (1998) 35-63.

[96] P.R. Bevington, D.K. Robinson, Data Reduction and Error Analysis for the Physical Sciences. 3rd ed.; McGraw-Hill, New York, NY, 2003.

[97] H. Valipour, D. Zimmermann, *J. Chem. Phys.* 114 (2001) 3535-3545.

[98] A.S. Pine, J.P. Looney, *J. Chem. Phys.* 93 (1990) 6942-6953.

[99] M. Dhyne, L. Fissiaux, J.C. Populaire, M. Lepere, *J. Quant. Spectrosc. Radiat. Transf.* 110 (2009) 358-366.

[100] M. Dhyne, P. Joubert, J.C. Populaire, M. Lepere, *J. Quant. Spectrosc. Radiat. Transf.* 111 (2010) 973-989.

[101] P. Minutolo, C. Corsi, F. D'Amato, M. DeRosa, *Eur. Phys. J. D* 17 (2001) 175-179.

[102] W.C. Swann, S.L. Gilbert, *J. Opt. Soc. Amer. B* 17 (2000) 1263-1270.

[103] C. Povey, A. Predoi-Cross, D.R. Hurtmans, *Molecular Physics* 110 (2012) 2633-2644.

[104] H. Li, A. Farooq, J.B. Jeffries, R.K. Hanson, *Journal of Quantitative Spectroscopy and Radiative Transfer* 109 (2008) 132-143.

[105] R.W.P. Drever, J.L. Hall, F.V. Kowalski, J. Hough, G.M. Ford, *Appl. Phys. B* 31 (1983) 97-105.

[106] E.D. Black, *Am. J. Phys.* 69 (2001) 79-87.